Carbon Nanotubes as Cooper Pair Beam Splitters

Lorentz Herrmann

Carbon Nanotubes as Cooper Pair Beam Splitters

Dissertation
to obtain the Doctoral Degree of Science
(Dr. rer. nat.)
(Docteur de l'université Paris VI)
from the Faculty of Physics
of the University of Regensburg
and
of the University Paris VI

presented by

Lorenz Herrmann
from Regensburg

2010

This thesis was supervised by Dr. Takis Kontos and Prof. Dr. Ch. Strunk and emerged from a double supervised Ph.d. project (co-tutelle de thèse) between Laboratoire Pierre Aigrain at Ecole Normale Supérieure Paris and the University of Regensburg.

Das Promotionsgesuch wurde am 01.06.2010 eingereicht. Das Kolloquium fand am 09.07.2010 statt.

Prüfungsausschuss:

Vorsitzender:	Prof. Dr. Milena Grifoni
1. Gutachter:	Prof. Dr. Christoph Strunk
2. Gutachter:	Dr. habil. Takis Kontos
weiterer Prüfer:	Prof. Dr. Elke Scheer
weiterer Prüfer:	Prof. Dr. Jascha Repp
weiterer Prüfer:	Dr. habil. Bernard Plaçais

Thèse de Doctorat de l'Université Paris VI
Spécialité: Physique des Solides
présentée par Lorenz Herrmann
pour obtenir le titre de Docteur de l'université Paris VI

Soutenue le 09. juillet 2010 devant le jury composé de:

président:	Milena Grifoni
rapporteur:	Prof. Dr. Christoph Strunk
directeur de thèse:	Dr. Takis Kontos
rapporteur:	Prof. Dr. Elke Scheer
examinateur:	Prof. Dr. Jascha Repp
examinateur:	Dr. Bernard Plaçais

Laboratories

Laboratoire Pierre Aigrain, CNRS UMR 8551, Ecole Normale Supérieure, 24, rue Lhomond, 75231 Paris Cedex 05, France.

Institut for Experimental and Applied Physics, University of Regensburg, Universitätstraße 31, 93040 Regensburg, Germany.

Abstract

We report on conductance measurements in carbon nanotube based double quantum dots connected to two normal electrodes and a central superconducting finger. By operating our devices as Cooper pair beam splitters, we provide evidence for Crossed Andreev Reflection (CAR). We inject Cooper pairs in the superconducting electrode and measure the differential conductance at both left and right arm. The contacts split the device into two coupled quantum dots. Each of the quantum dots can be tuned by a lateral sidegate. If the two sidegates are tuned such that both quantum dots are at a transmission resonance, a considerable part of the injected Cooper pairs splits into different normal contacts. On the contrary, if only one of the two dots is at resonance, nearly all pairs tunnel to the same normal contact. By comparing different triple points in the double dot stability diagram, we demonstrate the contribution of split Cooper pairs to the total current. In this manner, we are able to extract a splitting efficiency of up to 50% in the resonant case. Carbon Nanotubes ensure ballistic transport and long spin-flip scattering lengths. Due to these properties they are promising candidates to investigate EPR-type correlations in solid state systems.

Zusammenfassung

Diese Doktorarbeit beschäftigt sich mit auf Kohlenstoffnanoröhren basierenden Doppelquantenpunkten, welche mit zwei normalleitenden und einem supraleitenden Kontakt verbunden sind. Indem wir unsere Proben als Cooper Paar Strahlteiler verwenden, können wir Nonlokale Andreev-Reflektion nachweisen. Wir injezieren dazu Cooper-Paare in den supraleitenden Kontakt und messen den differentiellen Leitwert an den beiden Normalkontakten. Die drei Kontakte unterteilen unsere Proben in einen Doppelquantenpunkt. Jeder Quantenpunkt wird von einer lateralen Gatterspannung gesteuert. Falls beide Quantenpunkte in Resonanz mit dem chemischen Potential der Kontakte sind, trennt sich ein beträchtlicher Teil der injizierten Cooper Paare in verschiedene Normalkontakte auf. Falls, im Gegensatz dazu, nur einer der beiden Quantenpunkte in Resoanz ist, tunneln nahezu alle Cooper-Paare über eben

diesen Quantenpunkt zum entsprechenden Normalkontakt. Indem wir verschiedene Triple-Punkte aus dem Stabilitätsdiagram des Doppelquantenpunkts vergleichen, demonstrieren wir, dass Nonlokale Andreev Reflektion zum Gesamtstrom beiträgt. Mit dieser Methode extrahieren wir außerdem eine Splitting-Effizienz, die bis zu 50% betragen kann. Der ballistische Transport und die großen Spin-Kohärenzlängen in Kohlenstoffnanoröhren predestinieren dieses Materialsystem für Korrelationsexperimente im Sinne von Einstein-Podolsky-Rosen im Festkörper.

Resumé

Cette thèse a pour objet des mésures de conductance dans des double boîtes quantiques basées sur des nanotubes de carbone monoparois qui sont connectés à deux contacts normaux et un contact supraconduteur dans une géométrie du type Einstein-Podolsky-Rosen. Nous injectons des pairs de Cooper dans le contact supraconducteur et nous mésurons simultanément la conductance différentielle aux deux contacts normaux. Avec ce type de mésure nous séparons les pairs de Cooper dans deux contacts différents. Ce processus est équivalent aux réflexions d'Andreev croisées. En déposant les trois contacts sur le nanotube de carbone, nous créons une double boîte quantique. Chacune des boîtes quantiques est contrôlée par une grille latérale. Si toutes les deux boîtes sont en résonance, une partie considérable des pairs de Cooper se sépare dans différents contacts normaux. En contraire, si seulement une des boîtes est en résonance, presque tous les pairs sont transmis au même contact normal. En comparisant des différents points triple dans le diagramme de stabilité de la double boîte quantique, nous démontrons la contribution des réflexions d'Andreev croisées au courant total. Par ce méthode nous pouvons extraire une efficacité du processus de séparation qui s'éleve jusqu'à 50% dans le cas résonant. Le transport électronique dans des nanotubes de carbone est ballistique. En plus des nanotubes de carbone possède une longue cohérence du spin. A cause de ces propriétés, des nanotubes de carbone sont un matériel favorable pour effectuer des expériences des correlations du type EPR dans la physique des solides.

Keywords

Mesoscopic physics, Single-Walled Carbon Nanotubes, Electronic transport, Superconductivity, Beamsplitter, Coulomb blockade, Double quantum dots, Hanbury-Brown-Twiss, Einstein-Podolsky-Rosen, Crossed Andreev Reflection

Schlüsselbegriffe

Mesoskopische Physik, Kohlenstoffnanoröhren, Elektronischer Transport, Supraleitung, Beamsplitter, Coulomb Blockade, Doppelquantenpunkt, Hanbury-Brown-Twiss, Einstein-Podolsky-Rosen, Nonlokale Andreev Reflektion

Mots Clés

Physique mésoscopique, Nanotube de Carbone Monoparois (SWNT), Transport Electronique, Supraconductivité, Beamsplitter, Blockage de Coulomb, Double boîte quantique, Hanbury-Brown-Twiss, Einstein-Podolsky-Rosen, Réfléxions d'Andreev croisées

Contents

1 Introduction **9**
- 1.1 Artificial Atoms and Molecules . . . 9
- 1.2 EPR-experiments in solid state . . . 12

2 Basics **17**
- 2.1 Single-Walled Carbon Nanotubes . . . 17
  - 2.1.1 Band structure . . . 17
  - 2.1.2 Electron transport in Single-Walled Nanotubes . . . 19
- 2.2 Quantum dots and Coulomb blockade . . . 21
  - 2.2.1 Coulomb blockade at zero bias . . . 21
  - 2.2.2 Coulomb blockade at finite bias . . . 24
- 2.3 Double Quantum dots . . . 25
  - 2.3.1 Capacitive coupling: The electrostatic model . . . 26
  - 2.3.2 High interdot tunnel coupling: The molecular state . . . 29
- 2.4 BCS-theory and the spin singlet state . . . 34
  - 2.4.1 The BCS ground state . . . 34
  - 2.4.2 Quasiparticles and the density of states . . . 36
  - 2.4.3 Tunneling processes involving superconductors . . . 36
- 2.5 Injecting superconducting correlations in a normal conductor: Andreev Reflection . . . 38
  - 2.5.1 Andreev Reflection at an NS interface . . . 38
  - 2.5.2 Crossed Andreev Reflection . . . 40
- 2.6 Putting the puzzle together: Theoretical description of the beamsplitter 41
  - 2.6.1 Qualitative Theory and Splitting argument . . . 45
  - 2.6.2 Methods to obtain the Γ's . . . 48

3 Sample preparation and Measurement environment **53**
- 3.1 CVD growth . . . 54
- 3.2 Lithographical patterning . . . 54
- 3.3 Evaporation . . . 55

3.3.1 Shadow Evaporation . . . 56
3.3.2 Two-step Process . . . 57
3.4 Measurement setup . . . 57
3.4.1 Electronics . . . 59
3.4.2 Cryogenics . . . 59

4 Transport in a double quantum dot connected to a superconducting lead 61
4.1 Spectroscopy of the double dot . . . 61
4.1.1 Stability diagram of the sample . . . 62
4.1.2 Extraction of electrostatic parameters . . . 67
4.1.3 Testing the NS-junction . . . 73
4.2 Evidence for splitting Cooper pairs . . . 74
4.2.1 Measurements along the axis of detuning at zero and finite magnetic field . . . 74
4.2.2 Unbalanced Anticrossings . . . 78
4.2.3 Quantitative comparison of theory and experiment . . . 79
4.3 Nonlinear transport at triple points . . . 85

5 Discussion and Outlook 87

6 Conclusion 91

A CVD growth of Single-Walled Carbon Nanotubes 93
A.1 Catalyst recipe for Single-Walled Carbon Nanotubes . . . 93
A.2 Growth process - Paris . . . 93
A.3 Growth process - Regensburg . . . 94

B Printed-Circuit-Bord 95

C Finding the working point of the beamsplitter 97

D Determination of the current going to the superconductor in the side-injection setup 99

Literature 101

Acknowledgements 111

Chapter 1

Introduction

1.1 Artificial Atoms and Molecules

Artificial atoms are objects which have bound, discrete electronic states, just like naturally occuring atoms. The big difference is, however, that artificial atoms are tunable. That is to say that the energy level separation as well as the number of electrons on the atom can be tailored such that a wide parameter range becomes accessible, whereas in natural atoms these parameters are fixed by the fundamental laws of nature.

Artificial atoms are small particles which are only a few hundred nanometers in size [1]. They can be coupled to electrical leads through tunnel junctions, as depicted in figure (1.1(a)). Like natural atoms, artificial atoms display a discrete spectrum. In the literature, artificial atoms are often called quantum dots, pin-pointing their small dimensions and their quantum physical character.
Notably, metallic islands are not the only possibility to form artificial atoms: As shown in figure (1.1(b)), the artificial atom can also consist of a nanowire [2], [3], [4] or a Carbon Nanotube [5]. Furthermore artificial atoms have been fabricated out of single molecules [6], nanocrystals [7], [8] and two dimensional electron gases [9] (see also figure 1.1(c)). All these methods have in common that the electrons are confined in a small region. In the case of two-dimensional electron gases, this confinement is not ensured by material boundaries but by lateral confining electrodes: By applying a negative potential to the electrodes, they deplete the region lying underneath in the 2DEG and hence define an island in the middle. The electrons thus face the potential illustrated in figure (1.1(d)). The big well in the middle thereby illustrates the artificial atom. The two boundaries constitute the tunnel couplings to the leads. If the barriers are sufficiently high, electrons can tunnel one by one to the quantum

dot, by means of gate voltage sweeps. Therefore this device is often referred to as Single Electron Transistor (SET).

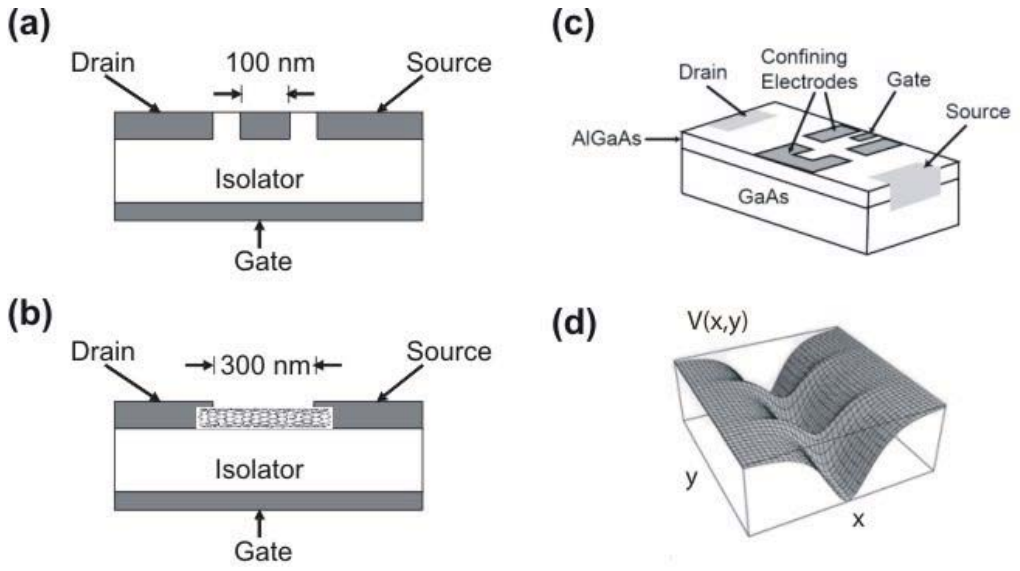

Figure 1.1: (a) An artificial atom in its simplest form: A small metallic island is connected to source and drain metallic leads by two tunnel barriers. (b) Alternatively, the metallic island can be replaced by a quantum wire, e.g. a nanowire or a Carbon Nanotube. (c) A further possibility is to define an artificial atom in a two-dimensional electron gas. A negative potential applied to the confinement electrodes depletes the region underneath and forms an isolated island which is weakly connected to source and drain contacts (taken from reference [10]). (d) Here, the potential created in this way is illustrated. The figure is taken from reference [10].

The biggest advantage of artificial atoms in comparison with natural atoms is their tunability. In natural atoms we normally perform photoelectron spectroscopy to determine the minimum energy to remove an electron (=ionization energy), and the maximal energy of emitted photons when an atom captures an electron (electron affinity). In artificial atoms we can also measure the energy which is needed to add or remove electrons, using a slightly different method. Normally we measure the differential conductance through the quantum dot and extract the energy which is needed to add/remove an electron. The energy which is needed to add an electron to the artificial atom is called the addition energy. The addition energy is composed of the quantum mechanical level separation and the charging energy, whereby the latter contribution is due to Coulomb interaction .
In artificial atoms we have possibilities to tune the addition energy and the number

of electrons on the dot. For instance we can modify the quantum mechanical level separation. To illustrate the mechanism we consider the 'particle in a box' problem in quantum mechanics. There, the energy level separation can be written as $\Delta E \sim \frac{\hbar^2}{ma^2}$, where a is the size of the box. Using standard lithography techniques, a can be varied over a large parameter range and hence the quantum mechanical energy level separation within an artificial atom can be tailored. Furthermore, by putting a gate electrode near to the artificial atom, one obtains a significant advantage compared to natural atoms: If the artificial atom is sufficiently small, the gate can be used to change the number of electrons on the artificial atom one by one. That means that we can use the gate electrode to align the quantized energy levels with the chemical potential of the leads and add/remove electrons in a controlled and reversible way. In the picture of natural atoms the gate is thus a possibility which 'moves' the atom through the periodic table. This is a further possibility which is not present in natural atoms. Finally we state that in suitable circuit and sample designs, a single charge more or less on the quantum dot can vary the capacitance of the artificial atom or the current between source and drain by many orders of magnitude. Hence a single charge can be detected with modern measurement techniques.
In the case of heterostructure artificial atoms, the tunnel coupling can be controlled by the value of the negative voltage which is applied to the confining electrodes. This is a further advantage of artificial atoms with respect to natural atoms.
Artificial atoms open a new parameter range to a variety of fundamental effects in physics. One example particularly important for this thesis is Coulomb-blockade (see section 2.2). Another example is the Kondo effect which is explained by the antiferromagnetic coupling between a magnetic impurity and the spin of the host's conduction electrons [11]. The possibility to design artificial atoms has opened avenues to study this many-body problem in a controlled way [12], [13], [14], [6]. The same applies to optics, where artificial atoms can be used as quantum emitters [15], [16], [17].

Nature puts natural atoms together to form a molecule. The same applies to artificial atoms. Putting artificial atoms together forms artificial molecules. The simplest case of an artificial molecule is two artificial atoms in series, or one artificial atom in a magnetic field. In both cases the electrons can be localized at different sites of the artificial molecules [18], [19], [20]. This thesis is set in the context of a device consisting of two artificial atoms in series which is called a double quantum dot. In our experiment we use Single-Walled Carbon nanotubes [21], [22]. Double quantum dots based on different materials, such as two-dimensional electron gases [23], [24] and nanowires [25], [26], are described in the literature.

1.2 EPR-experiments in solid state

Entangled states play an important role in quantum mechanics since the original work of Einstein, Podolsky and Rosen (EPR) [27] in 1935. Their reasoning is exemplified by the following *Gedankenexperiment* [28]:
Two spin-1/2 particles are prepared in a quantum mechanical state which can be written as

$$\Psi = \mid S, M\rangle = \mid 0, 0\rangle = \frac{1}{\sqrt{2}}[\mid\uparrow,\downarrow\rangle - \mid\downarrow,\uparrow\rangle] \tag{1.1}$$

In this example, the observable is not momentum or space but spin, i.e. only the spin part of the wave-function is considered. If two spins are prepared in a common state, quantum mechanical selection rules describe how this can be done [29]: The two particles have spin quantum numbers $s_1 = s_2 = \frac{1}{2}$ which act like angular momenta. The total spin of the two-particle state can either be $S = 0$ (singlet state) or $S = 1$ (triplet state). Whereas the triplet state is three-fold degenerate (M consisting of 2S+1 values, running from -S to S in integer numbers), the singlet state can only be expressed as given in equation (1.1). This state is a two-particle state which cannot be factorized. In quantum mechanics this characterizes a bipartite state.

Imagine that the two spins of the singlet state are spatially separated in an experimental arrangement as illustrated in figure (1.2). Due to entanglement, a detection of the spin state of one of the two spins would give a result which predicts the outcome of the detection of the spin state of the second spin with certainty and instantaneously. This is paradoxical because there is no classical explanation for this effect. Historically, it took quite a time before entanglement was accepted as an inherent property of quantum mechanics [30].

Entanglement and EPR-pairs play an important role in quantum computers. In a recent publication [32], the author asks where the research fields of quantum computing and quantum information, which became highly fashionable in the early nineties [33], [34], [35], [36], [37], [38], are standing after 20 years of research. The surprising answer is that quantum computers are already there. However, these systems are still working at a very rudimentary level and cannot be considered as computers in our everyday's sense of the word. They rather deal with issues like ultrasecure information processing [39], which is an application that is more at hand than ultrafast calculations. Here, we give a short overview of how this is possible.
In quantum computing, the classical bit is replaced by the quantum bit. The quantum bit is a two-level quantum system, e.g. $|\uparrow\rangle$, $|\downarrow\rangle$, replacing boolean 0,1. The big

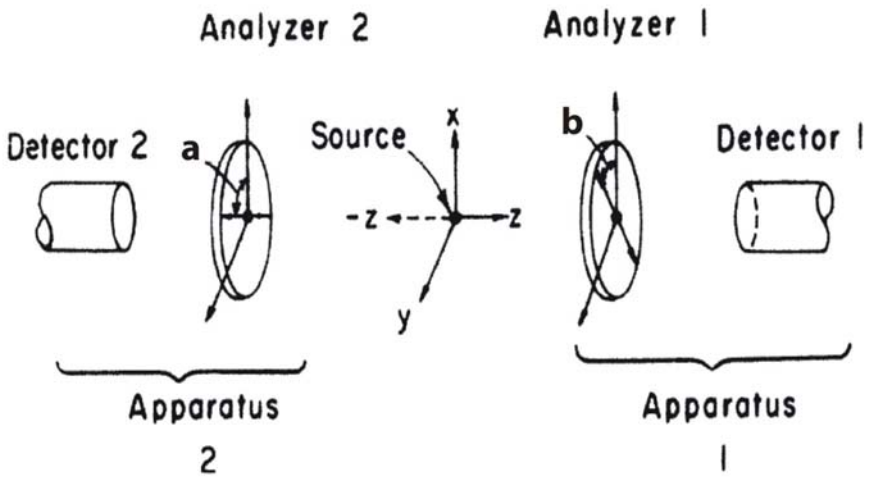

Figure 1.2: Setup to illustrate the Einstein-Podolsky-Rosen Gedankenexperiment, taken from Clauser and Horne [31].

difference in comparison with classical bits is that quantum bits cannot just be in configuration $|\uparrow\rangle$ or $|\downarrow\rangle$, but in any superposition of its two levels: $|\Psi\rangle = \alpha\,|\uparrow\rangle + \beta\,|\downarrow\rangle$. If one measures the state, however, only the two results $|\uparrow\rangle$ or $|\downarrow\rangle$ can occur.
The EPR pair is an example of a two qubit state. If we take again the state $\frac{|\uparrow\downarrow\rangle - |\downarrow\uparrow\rangle}{\sqrt{2}}$ and measure the first qubit, we find it with probability 1/2 in level $|\uparrow\rangle$ and with probabiltiy 1/2 in level $|\downarrow\rangle$. After the first measurement, however, the state of the two qubit system is either $|\uparrow\downarrow\rangle$ or $|\downarrow\uparrow\rangle$ and hence we can predict the outcome of the measurement of particle two with certainty. That means that the measurement outcomes are correlated.
Rather than classical gates, quantum computing uses quantum gates. These gates are used to manipulate the qubits. The only constraint in quantum gates is that the matrices describing the gates must be unitary. The quantum gates for single qubit manipulations are represented by 2x2 matrices whereas two-qubit manipulations are carried out by 4x4 matrices.
An example how qubits and gates can be used in a quantum computation process is illustrated in reference [40] by the so-called quantum teleportation.
In this process, a qubit $|\Psi\rangle$ is transferred from Alice to Bob with the help of an EPR-pair. That means that each person possesses one qubit of the EPR pair as a point of departure. Alice then interacts the qubit $|\Psi\rangle$ with her part of the EPR-pair and then performs a measurement. She obtains one of the following results: $\downarrow\downarrow$, $\downarrow\uparrow$, $\uparrow\downarrow$, $\uparrow\uparrow$. Alice then sends the result of her measurement in a classical way to Bob.

Surprisingly it shows out that Bob can find an appropriate quantum gate operation for each of the possible results of Alice's measurement to reconstruct the original qubit Ψ out of his half of the EPR pair.
The next question is how quantum-computer-like operations could be implemented. First results have been obtained using nuclear magnetic resonance [41], [42], [43], cold ion trap [44], [45] and optical methods [46], [47], as was nearest at hand considering the original EPR-experiment.
A different approach has been suggested in the late nineties [48], [49]. The authors point out that it is unclear whether atomic physics-implementations are suitable to be scaled up to large-scale quantum computation. Instead, the authors suggest to use the solid state for quantum computing. Unlike atoms, solid state devices can be tailored as described in section (1.1) and hence allow the adjustment of various parameters of solid state based quantum bits [50]. It is pointed out [51] that superconducting quantum bits are gaining more and more importance. The advantage is that Cooper-pairs are natural EPR-pairs.
Quantum computing with superconducting qubits involves quantum circuits and quantum gates. An important question to ask is how mesoscopic circuits, which are typically hundreds of nanometers wide and contain trillions of electrons, can show their quantum character and house quantum bits and even entangled quantum states. The answer proceeds along similar lines as given in section (1.1): The quantum nature of these circuits can be observed because they can be engineered such that they are isolated enough from their environment. Significant coupling to the environment, in turn, causes rapid decoherence, destroying the quantum state of the circuit and makes its behavior classical. The exclusion of decoherence is thus one of the basic challenges in quantum circuits. Decoherent elements can originate from radio and television transmitters. These can be eliminiated by using shielding and broadband filters. Furthermore it must be ensured that the complex impedances seen by the qubit are high over a broad bandwidth. The main intrinsic limitation on the coherence of superconducting qubits results from 1/f noise.

Despite these difficulties, various experiments in the past years provided evidence that mesoscopic (and even macroscopic) electrical circuits can behave as quantum systems [52], [53], [54], [55]. Recently, superconducting qubits have furthermore been prepared in Bell states [56] and a violation of Bell's inequality was demonstrated for the first time within a solid state device [57]. Till to date, three fundamental types of superconducting qubits are experimentally explored: flux [58], [59], charge [60] and phase [61]. Additionally, the spin of the electron was pointed out to be a candidate for a quantum bit [48], [62]. This idea was supported by experiments which showed that dephasing times approaching microseconds and phase-coherent transport up to 100 μm are possible. [63], [64], [65]. Metallic carbon nanotubes are predicted to

exhibit ballistic transport and long spin-flip scattering lengths, both relevant to the coherent transport of EPR pairs [66]. Hence Cooper pairs are supposed to have a long superconducting coherence length within these quasi-one dimensional conductors.
Efficient quantum gates are a further challenge. After theoretical suggestions based on virtual photons, real excitation of the resonator and geometric phase [67], first quantum-processor like implementations are visible in the literature [68]. Nevertheless it is pointed out that qubit coherence length is still one of the most demanding issues [56].
About 10 years ago it was suggested that Coulomb blockade in quantum dots could be used to implement quantum gates on electron-spin based qubits [48], [49]. As Single-Walled Carbon nanotubes can be used as quantum dots (compare section 1.1), a Single-Walled Carbon nanotube with a central superconducting electrode and two normal leads could act as a nanotube-superconductor entangler [69], [70], [71]. In this thesis we pick up the idea to create EPR-pairs in a Single-Walled Carbon nanotube beamsplitter. We show experimentally that within an EPR-type geometry, a Cooper-pair coming from a superconducting source contact can be split into two normal metal leads.

Chapter 2

Basics

2.1 Single-Walled Carbon Nanotubes

Discovered in 1991 by Iijima [72], Single-Walled Carbon nanotubes have been an extensive source of research. This is due to outstanding properties, both in mechanical and electrical respect. Carbon Nanotubes are very light, yet much stronger than stainless steel. This makes them interesting for applications, e.g. in glues. In this thesis, we focus on electronic properties of Carbon Nanotubes. A first remarkable fact is that Carbon Nanotubes can carry extremely high current densities, exceeding normal metals by far. Moreover, due to their tininess, they can be used in a large variety of experiments where quantum phenomena appear.

2.1.1 Band structure

The calculation of the band structure of Single-Walled Carbon nanotubes proceeds in two steps. First, the band structure of graphene is calculated in a tight-binding model [73]. As Single-Walled Carbon nanotubes can be understood as rolled-up graphene sheets, a process called zone-folding is used to take into account the chiral structure of the nanotube.
Graphene consists of a hexagonal lattice (see figure (2.1)). The lattice is defined by two primitive lattice vectors $\vec{a}_1$ and $\vec{a}_2$. The chirality vector $\vec{C}_h$ is defined by a linear combination of the primitive lattice vectors.

$$\vec{C}_h = n\vec{a}_1 + m\vec{a}_2 \tag{2.1}$$

The index numbers n and m are the chiral indices which contain all the information about diameter and the roll-up direction. A second vector is important: The translational vector $\vec{a}$ is perpendicular to the circumferential vector. Together with

$\vec{C}_h$ it defines the unit cell of the Carbon Nanotube. When going to reciprocal space, the lattice vectors $\vec{C}_h$ and $\vec{a}$ are replaced by $\vec{k}_\perp$ and $\vec{k}_z$. Thereby $\vec{k}_\perp$ is associated with the circumference of the nanotube whereas $\vec{k}_z$ refers to the axis along the tube. Compared to its diameter, the nanotube can be considered as infinitely long. Hence $k_z = 2\pi/a$ is continuous. Around the circumference, however, the situation is different. A wave travelling around the nanotube must have the same value at its point of departure. Therefore we find:

$$e^{i\vec{k}_\perp \vec{r}} = e^{i\vec{k}_\perp (\vec{C}_h + \vec{r})} \tag{2.2}$$

This leads to the boundary condition for $k_\perp$:

$$\vec{k}_\perp \vec{C}_h = 2\pi j \tag{2.3}$$

where j is an integer number. Zone folding thus imposes a boundary condition on the energy dispersion of Graphene.

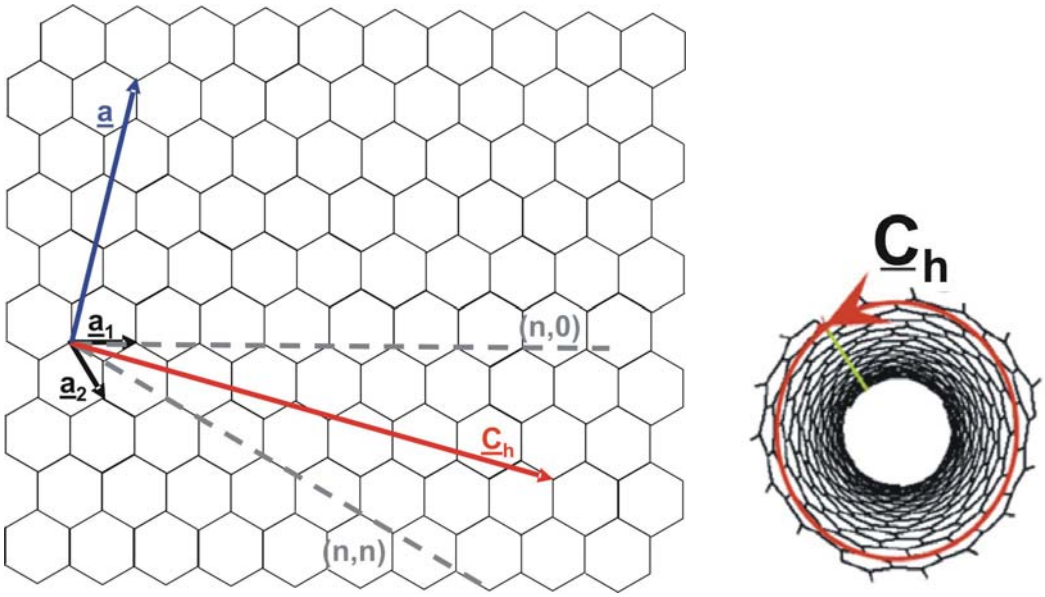

Figure 2.1: (Left) The lattice of graphene is spanned by two primitive lattice vectors $\vec{a}_1$ and $\vec{a}_2$. The index numbers n and m define the chirality of a tube which contains information on diameter and material properties. (Right) The chirality vector $\vec{C}_h$ describes the axis along which the graphene sheet is rolled up to form a nanotube.

The band structure of graphene is shown in the left part of figure (2.2). It can be seen that there are six points where conduction and valence band touch each other.

Within these six points, only two points are linearly independent, namely K and K'. As stated above, zone folding imposes a boundary condition on the dispersion relation of graphene which yields to cuts within the dispersion relation.
To simplify the picture we assume that $k_\perp$ is identical with k_y in figure (2.2 (Left)). Figure (2.2 (Right)) is a zoom on the red hexagon within figure (2.2 (Left)). Additionally, the line-cuts resulting from zone folding are shown. Only states where the Graphene hexagon and the quantized lines intersect are allowed states in Single-Walled Carbon nanotubes. Depending on the chirality vector $\vec{C}_h$, K and K' either intersect with the line-cuts or not. In the latter case there is no connection between conduction and valence band, a gap forms, and the nanotube is semiconducting. Otherwise the nanotube is metallic. Metallic nanotubes occur, if $(n-m)/3 \in \mathbb{Z}$.

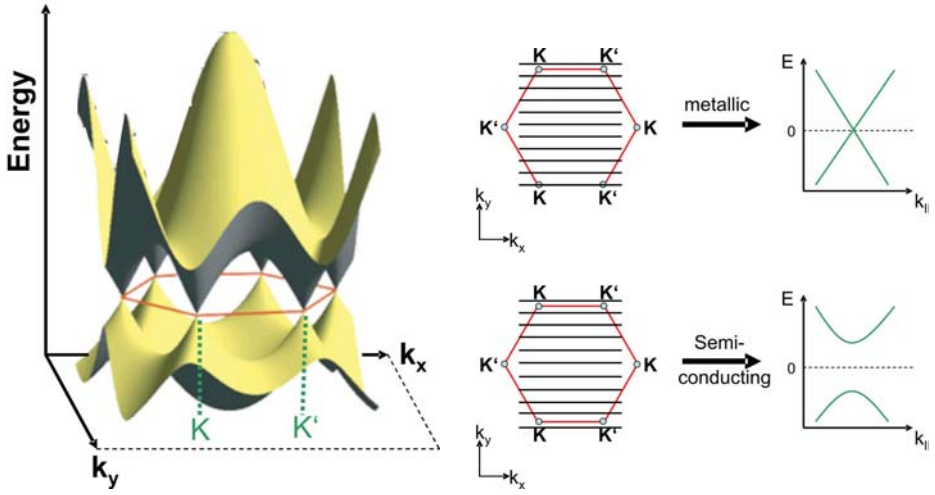

*Figure 2.2: (Left) The tight binding calculation of the bandstructure of graphene. (Taken from http : //www.als.lbl.gov/pics/*154*graphene*01*.png and modified). (Right) Zone folding leads to an additional quantization in $k_\perp$ direction. Only if the line-cuts intersect with K and K' the nanotube is metallic. Otherwise a gap develops and the tube is semiconducting.*

2.1.2 Electron transport in Single-Walled Nanotubes

At the macroscopic scale, electron transport within a conductor is diffusive and the conductance is given by the ohmic relation $G = \sigma W/L$. In this expression W and L are width and length, respectively, and σ is a material parameter. When dimensions

become much smaller than the mean free path of an electron, however, another phenomenon called ballistic transport occurs. In this regime, the conductance is given by the Landauer-Büttiker formalism [74], [75], [76]. The result for the current through a mesoscopic conductor connected to two electron reservoirs, i.e. the contacts, is given by

$$I = \frac{e}{h} \int d\epsilon (f_L(\epsilon) - f_R(\epsilon)) T(\epsilon) \tag{2.4}$$

where $T(\epsilon)$ is the transmission probability through the conductor and f is the Fermi-Dirac distribution:

$$f_{L,R}(E) = \frac{1}{1 + e^{(E-\mu_{L,R})/k_B T}} \tag{2.5}$$

The conductance is defined by the following equation

$$G(\epsilon') = \frac{e^2}{h} \int d\epsilon T(\epsilon) F_T(\epsilon - \epsilon') \tag{2.6}$$

where $F_T(\epsilon - \epsilon')$ is the thermal broadening function $F_T(\epsilon - \epsilon') = -\frac{d}{d\epsilon}(\frac{1}{exp((\epsilon-\epsilon')/k_B T)+1}))$ which can be approximated as a Dirac δ-function in the zero temperature limit. Calculating the integral we obtain:

$$G(\epsilon') = \frac{e^2}{h} T(\epsilon') \tag{2.7}$$

Now it is evident that even for maximal transmission $T = 1$ the conductance cannot exceed $\frac{e^2}{h}$.
This result was derived for one transport mode. In Single-Walled Carbon Nanotubes there are two spin-degenerate and thus four transport modes. Therefore the maximal conductance is:

$$G_{max} = 4\frac{e^2}{h} \tag{2.8}$$

Consequently, the minimal contact resistance can be calculated as:

$$R_{min} = \frac{1}{G_{max}} \simeq 6,4k\Omega \tag{2.9}$$

In real samples, the transmission probability T is reduced by impurity scattering. Impurities can be formed inherently in carbon nanotubes during the growth process. We use Chemical Vapor Deposition because this is a process that reliably produces regular shaped Single-Walled Carbon Nanotubes with a low number of defects (see chapter [3]). The most important scatterers develop at the interface between Single-Walled Nanotube and the two contacts. The so-called contact resistance is thus a

crucial point for the electronic behavior of Single-Walled Carbon Nanotubes.
If contact resistances are low and the transmission approaches unity, a Single-Walled Carbon Nanotube between two contacts behaves like a Fabry-Perot interferometer [77]. Its behavior is explicitly dependent on quantum interference between propagating electron waves. In these devices, the nanotubes act as coherent electron waveguides with the resonant cavity formed between the two nanotube electrode interfaces. The number of electrons on the resonator is not fixed.
The situation is different if the contact resistance is higher, i.e. $\geq 20k\Omega$. Then transport is governed by a phenomenon named Coulomb blockade, a phenomenon which is explained in the next section.

2.2 Quantum dots and Coulomb blockade

A quantum dot develops if an artificial atom is weakly connected to the electron reservoirs (see section 1.1). This weak connection is described by quantum mechanical tunneling matrix elements. If temperature and coupling between leads and quantum dot are sufficiently low, a phenomenon called Coulomb blockade [78], [79], [80], [81] becomes important. In order to understand Coulomb-blockade, electron-electron interaction must be taken into account, which was not considered yet in the derivation given in subsection 2.1.2.
In our experiment, we use Single-Walled Carbon Nanotubes to implement quantum dots. If two contacts are evaporated on a Single-Walled Carbon Nanotube, tunnel barriers form between the nanotube and the metallic leads. In the following we describe how electronic transport is possible through such a structure.

2.2.1 Coulomb blockade at zero bias

If a quantum dot is in the Coulomb blockade regime and if we assume that the quantum mechanical level separation is negligible, an energy E_C is needed to add a supplementary charge to the dot.

$$k_B T_{el} << E_C = e^2/C_\Sigma \tag{2.10}$$

The energy E_C is called charging energy and C_Σ is the sum of all capacitances of the dot to leads, gates and ground. It is important that the energy to add an electron to the dot is bigger than the thermal energy $k_B T_{el}$. Therefore many experiments are carried out at low cryogenic temperatures, though room temperature devices are described in the literature [5] .
In a simplified picture, the situation is as illustrated in figure (2.3 (a)). The chemical

potential of the leads is μ_L and μ_R for left and right lead, respectively. In between the leads, the quantum dot has quantized energy levels. In the general case, this quantization is a sum of the electrostatic part E_C and a contribution coming from single particle quantization. The classical part is due to the Coulomb repulsion between single electrons, the quantum mechanical part is due to the small length of the nanotube between the two leads which results in an energy quantization $\Delta E = \frac{hv_F}{2L}$. Here, h is Planck's constant and v_F is the Fermi velocity in the nanotube. Additionally, a gate electrode acts on the dot which shifts the energy levels as a function of gate voltage. That is to say that the gate voltage alters the total charge on the dot. As $E = Q^2/2C$, the energy levels shift as a function of the gate voltage. The gate voltage can thus be used as a switch which moves the dot either in the Coulomb blockade regime (see figure 2.3(a)) or drives the dot into resonance (see figure 2.3(b)) by aligning the dot energy level with the chemical potential of the leads. By sweeping the gate voltage, one can therefore drive the quantum dot through a sequence of resonance peaks and blockaded regions. This leads to so-called Coulomb-peaks if the conductance is plotted as a function of gate voltage (see figure 2.3(c)).
In the next step the gate voltage difference between two adjacent levels on the quantum dot will be calculated. We start with the expression for the electrostatic energy difference $\triangle E = E(N+1) - E(N)$, where N is the number of electrons on the dot.

$$E(N) \equiv E_{electrostatic}(N, V_g) = \frac{1}{2C_\Sigma}(eN + C_g V_g)^2 \tag{2.11}$$

Transport through the dot can occur only if the probabilty of finding N elctrons on the dot is equal to the probability of finding N+1 electrons on the dot. From figure (2.11(d)) it is obvious that these points occur only if neighboring energy curves for N and N+1 particles intersect. Transport is possible if and only if this condition is met (compare figures 2.11(c) and 2.11(d)). Coming back to the required potential difference, it is obvious from equation (2.11) that a gate voltage change of $\Delta V = e/C_g$ moves the system from energy level E(N) to E(N+1).
In reality, the gate voltage change must also account for the quantum mechanical level spacing $\Delta\epsilon/e$. Additionally, one has to take into account the finite coupling of the gate by means of the factor

$$1/\alpha_g = C_\Sigma/C_g \tag{2.12}$$

We thus find:

$$\Delta U_g(N) = \frac{C_\Sigma}{eC_g}(\epsilon(N+1) - \epsilon(N)) + \frac{e}{C_g} = \frac{\epsilon(N+1) - \epsilon(N)}{e\alpha_g} + \frac{e}{C_g} \tag{2.13}$$

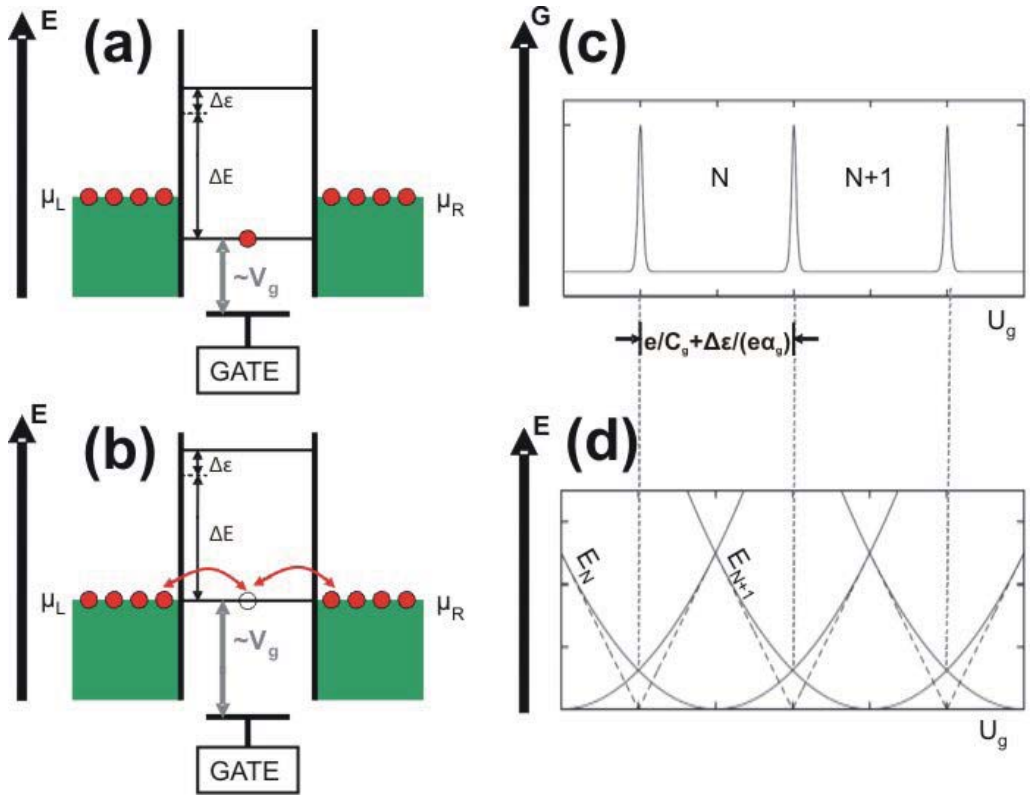

Figure 2.3: Coulomblockade in the zero bias regime: In figure (a) transport between the leads is not possible. The quantum dot is Coulomb blockaded because no energy level within the dot is aligned with the chemical potential of the leads. In figure (b) the gate voltage is modified such that an energy level of the dot is available for transport. (c) If the gate voltage is swept, energy levels are aligned with the chemical potential of the leads in regular gate voltage intervals. Hence a structure of regular conductance peaks develops. (d) In a slightly different picture, transport through the dot is possible if the energy for N particles on the dot equals the energy of N+1 particles. As the energy of the dot is a parabola as a function of gate voltage, transfer occurs at the points where the parabola for N charges intersects with the parabola for N+1 charges.

Within the Coulomb blockade regime, higher order tunneling processes can occur and contribute to the measured current [82], [83]. These processes can be elastic or inelastic.

Elastic cotunneling involves virtual states which are unoccupied and energetically above the chemical potential of the leads. The process is shown in figure (2.4(a)). The energy difference which is required to reach the virtual state defines the lifetime of the virtual state by means of the uncertainty relation: $\Delta t \sim \frac{\hbar}{\Delta E}$. In figure (2.4(b)), the "inverse" process is depicted which is described by the cotunneling of

a hole. This process is a two-electron process. That means that an electron trapped in the dot potential tunnels to the drain contact and simultaneously it is replaced by an electron coming from the source contact.
Figure (2.4(c)) shows an inelastic process: A ground state electron leaves the quantum dot by tunneling to the drain contact. At the same time, another electron tunnels into an excited state of the dot. This process becomes more frequent if the applied bias voltage eV_{sd} exceeds the energy difference $\Delta\epsilon$ between ground state and excited state. Inelastic cotunneling does not conserve energy.

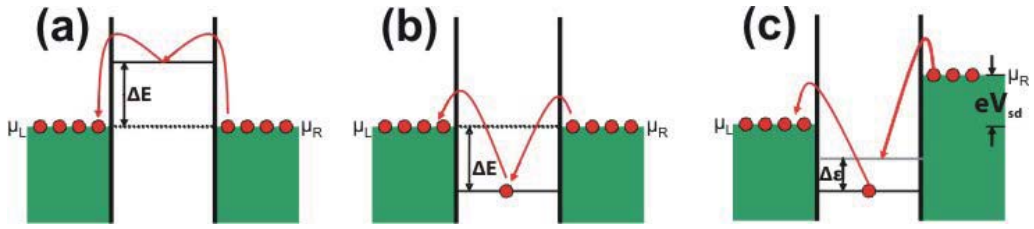

Figure 2.4: Elastic cotunneling of (a) electrons and (b) holes: Energy is conserved as the final state has the same energy as the initial state. In (c) an inelastic process is depicted: Whereas an electron leaves the quantum dot from its ground state, another electron tunnels into an excited state. Hence energy is not conserved.

2.2.2 Coulomb blockade at finite bias

At finite bias, the chemical potential of the leads is changed. Single electron tunneling occurs if either the chemical potential of the source contact or the chemical potential of the drain contact are aligned with the chemical potential of the dot. As the energy change needed for tunneling depends strongly on the position of the energy levels in the dot, single electron tunneling at finite bias is strongly dependent on the gate voltage. If one plots the differential conductance as a function of both gate voltage and source-drain voltage, the so-called Coulomb-diamonds become visible in a 2D-plot. A typical Coulomb-diamond can be seen in figure (2.5(Left)). For each of the four corner points a sketch illustrating how tunneling works, is provided. Generally it can be said that tunneling occurs only if the condition

$$\mu_{Drain} \leq \mu_{Dot} \leq \mu_{Source} \tag{2.14}$$

is fulfilled. Otherwise the dot is Coulomb-blockaded.
Carbon Nanotube quantum dots which are weakly coupled to the leads show Coulomb-

blockade behavior [84], [85]. In figure (2.5(Right)), a typical Coulomb diamonds measurement as observed in our devices is shown.

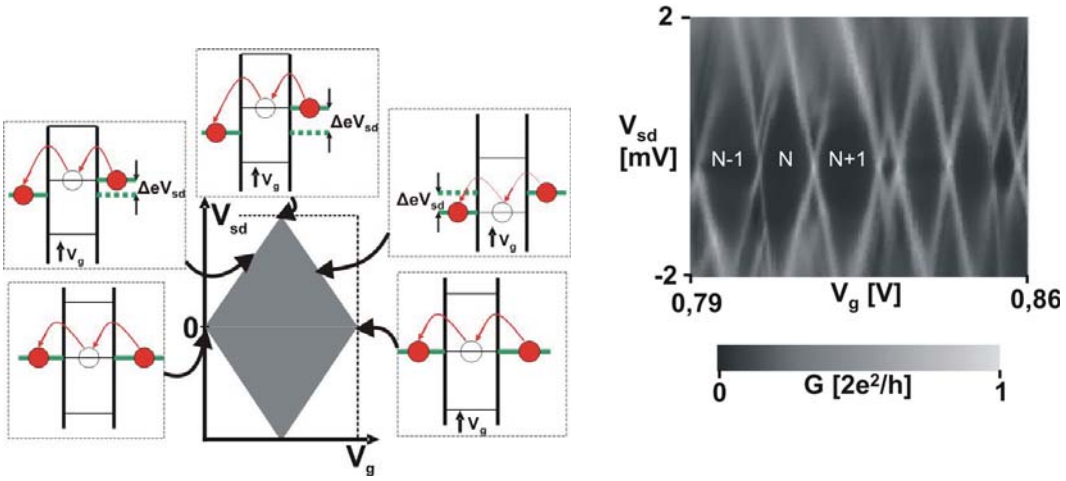

Figure 2.5: (Left) Schematical explanation of 2-dimensional diamond plots. Depending on the mutual positions of the chemical potential, the dot is either transparent or Coulomb-blockaded. The dark region within the Coulomb diamond signifies the area in which Coulomb-blockade dominates. Within white areas, a finite conductance between left and right reservoir is possible. (Right) Typical measurement of the differential conductance of our Single-Walled Carbon Nanotubes in the Coulomb-blockade regime (T=300mK). The regular spacing of the diamonds suggests that our nanotubes have a small number of defects.

2.3 Double Quantum dots

When two quantum dots are coupled in series, a double quantum dot develops [86], [23], [87]. The system is a network of capacitors and resistors as illustrated in figure (2.6). A gate voltage $V_{g1(2)}$ is coupled to each of the dots through a capacitor $C_{g1(2)}$. Furthermore the dots are coupled to source and drain, respectively, by tunnel resistors $R_{L(R)}$ and capacitors $C_{L(R)}$. Moreover $C_{\Sigma 1}, C_{\Sigma 2}$ are the total capacitances of 1st and 2nd dot to gates, leads and ground.

The most important element of the circuit diagram is the coupling between the two dots. The coupling is represented by C_M accounting for capacitive coupling between the dots and R_M standing for the tunnel coupling. Depending on these two parameters, one can distinguish between two regimes. First, we will discuss

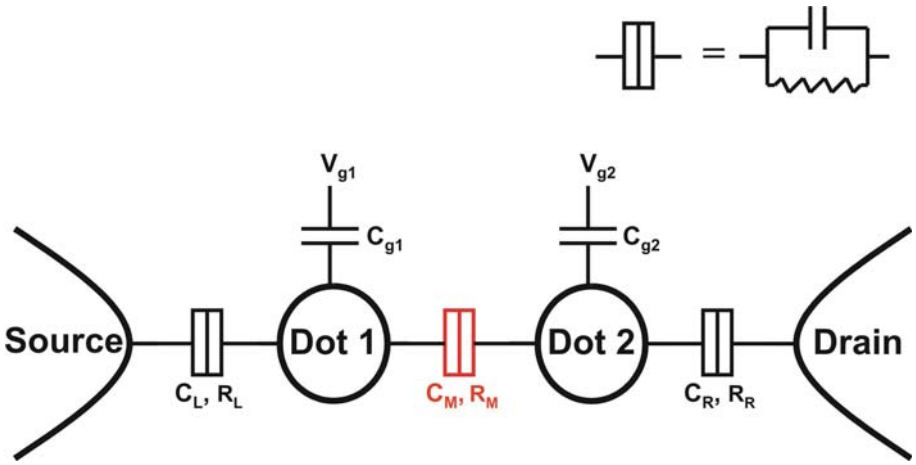

Figure 2.6: Electrical circuit representation of a double quantum dot: The coupling capacitance C_M and the coupling resistance R_M are the decisive elements for the electronic behavior of the dot.

the regime in which electrostatic coupling dominates and tunnel coupling is small. In this parameter range, electrostatic effects outweigh quantum mechanical effects by large. Therefore a classical description of the system is appropriate. Second, we will discuss the case of high interdot tunnel coupling. In this case, the electron wavefunction is delocalized over both dots and hence the electrons on the dot form a molecular state.

2.3.1 Capacitive coupling: The electrostatic model

Throughout this subsection, we assume that the intermediate tunnel coupling is very small and the intermediate capacitive coupling dominates. At the end of the subsection, we treat the two boundary cases for very low and very large intermediate capacitive coupling.

In a double dot system, transport is only possible at certain gate voltages. Measuring the conductance at zero bias through the whole system as a function of the two gate voltages V_{g1} and V_{g2}, one obtains the so-called honeycomb pattern (see figure 2.7(a)). Electron transport is only possible along the black lines. Within each hexagon, the number of charges on the double dot is fixed and transport is not possible, as illustrated in figure (2.7(b)). Concerning the lines of conductance within the stability diagram, one can discriminate 3 different situations, labeled (c) to (e). Each situation is explained by the mutual position of the energy levels of dots and leads,

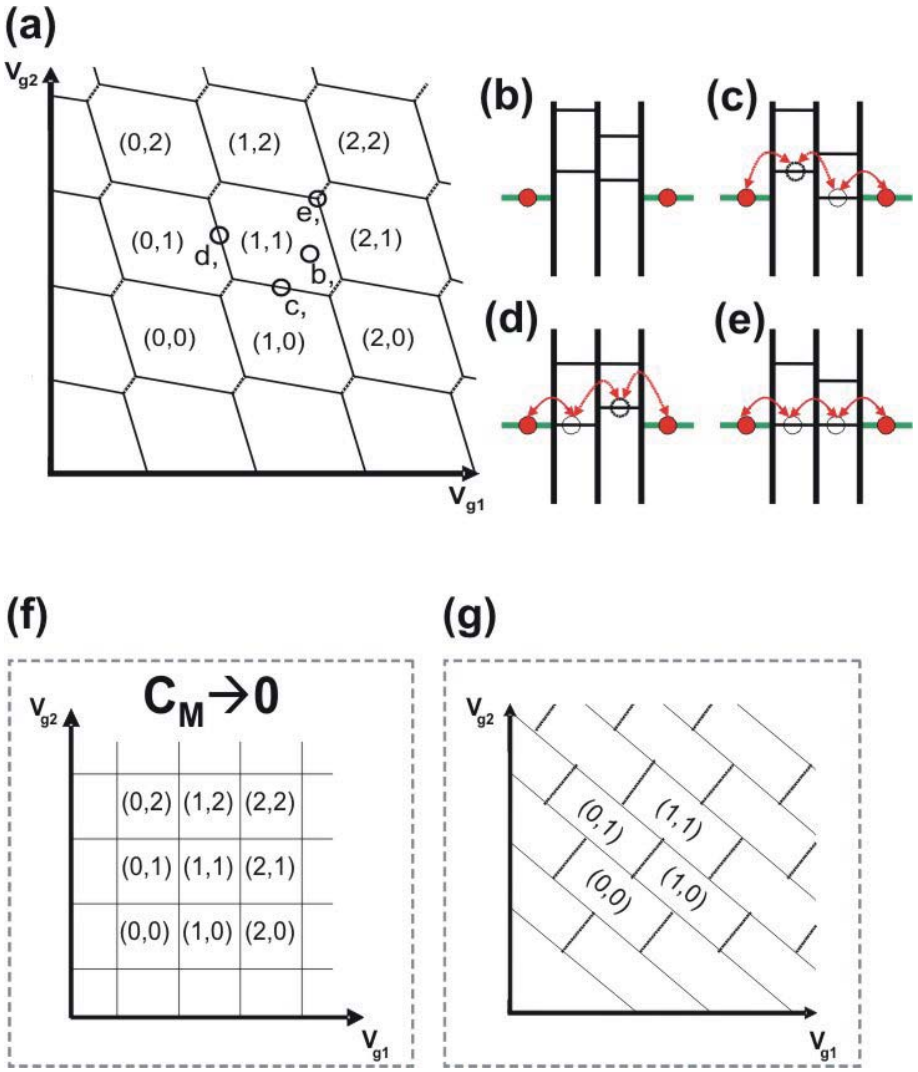

Figure 2.7: (a) A typical honeycomb stability diagram is shown here. Each honeycomb cell has a fixed number of electrons on left and right dot. (c)-(f) The corresponding energy level diagrams for the different transport configurations of the double dot. (g) Stability diagram of the double dot for $C_M \rightarrow 0$. (f) Stability diagram for very high capacitive interdot coupling.

as illustrated in the corresponding sketch at the up right side of figure (2.7). If cotunneling is negligible, transport in the double dot is only possible at the so-called triple points. An example of a triple point is labeled by (e). As can be seen in the sketch, all energy levels of dots and leads are aligned and hence transport is possible. In situations (c) and (d) only one dot level is aligned with the leads. At very small

but finite interdot tunnel coupling, electrons can nevertheless tunnel from source to drain by means of cotunneling [86], as is explained above for a single quantum dot. In figure (2.7(f)) it is shown how the stability diagram changes in the case $C_M \mapsto 0$. The degeneracy of the triple points, which is due to the capacitive coupling of the two dots, vanishes. In the other boundary case, if the capacitive coupling between the two dots becomes very high, the double dot effectively behaves like one big dot. Within the stability diagram this would mean that the hexagonal structure vanishes and only straight lines remain (see figure 2.7(g)).

Applying a finite bias to the double dot, the triple points enlarge to triangular regions. This is visible in figure (2.8(a)). In black solid lines, the original position of two adjacent honeycomb-cells including two triple points is depicted. Due to the applied bias voltage V_{sd} both vertical and horizontal lines shift by δV_{g1} and δV_{g2}. With the prefactors

$$\alpha_{g1} = \frac{C_{g1}}{C_{\Sigma 1}} \tag{2.15}$$

and

$$\alpha_{g2} = \frac{C_{g2}}{C_{\Sigma 2}} \tag{2.16}$$

which take into account the different coupling of each gate to its corresponding dot, we can write for the relation between $\delta V_{g1(g2)}$ and V_{sd}:

$$|e|\alpha_{g1}\delta V_{g1} = \frac{C_{g1}}{C_{\Sigma 1}}|e|\delta V_{g1} = |eV_{sd}| \tag{2.17}$$

$$|e|\alpha_{g2}\delta V_{g2} = \frac{C_{g2}}{C_{\Sigma 2}}|e|\delta V_{g2} = |eV_{sd}| \tag{2.18}$$

Figures (2.8(b)) ,(d) and (e) show how the applied bias voltage enlarges the triple points to triangular regions. In contrast to the zero bias case, where transport is only possible if all energy levels of dots and leads are aligned, a transport window is opened at finite bias. In figure (2.8(d)), a triple point of the zero bias stability diagram is treated. Imagine that the energy level of the source contact is lifted by a constant bias voltage. On the one hand, by modifying both gate voltages such that the dot energy levels are in-between the energy levels of source and drain, one can move from situation (2.8(d)) to (2.8(e)) within the stability diagram. For gate configurations in-between the two points, transport is possible. On the other hand one can also go from situation (2.8(d)) to siutation (2.8(b)) by sweeping only one gate. That means that transport is possible within the triangular region in the stability

diagram defined by the three points labeled (d),(e) and (b). At the corner points of the triangular regions, a further sweep of the gate voltages drives the double dot into the Coulomb blockade regime, as at least one of the two dot-levels exceeds the energy level of the source contact.
In (2.8(c)) a further phenomenon occurring within the triangular regions is explained figuratively: At sufficiently large bias, there is enough energy to populate excited states which can thus contribute to transport. This explains additional line structures within the triangular regions.

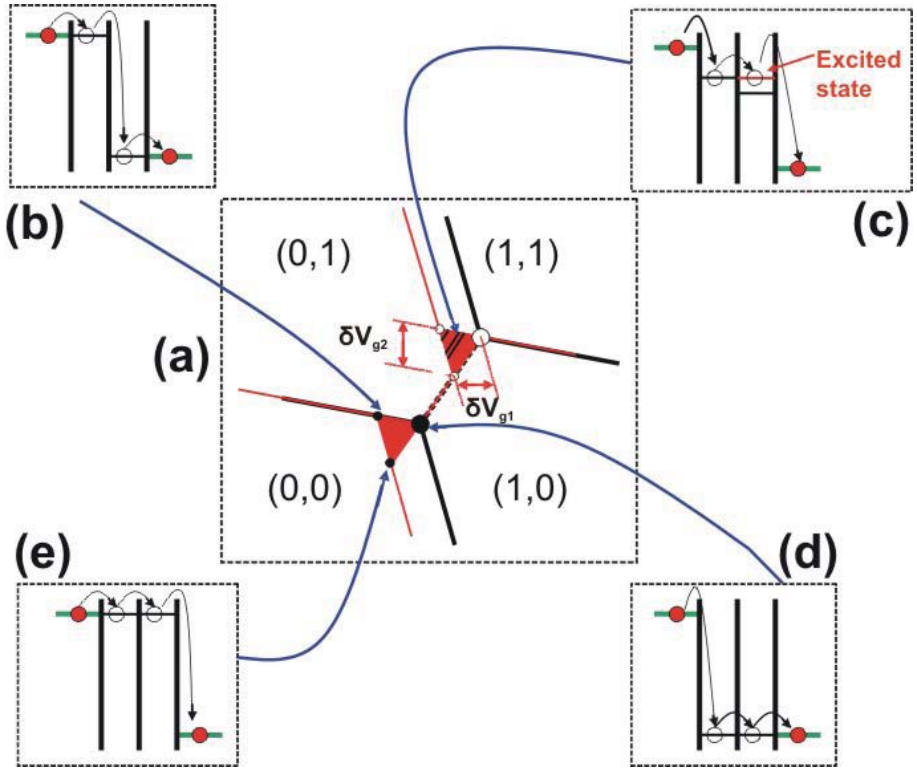

Figure 2.8: (a) At finite bias triple points split into triangular regions . (b),(d),(e) A detailed analysis of the mutual position of the energy levels explains how these enlarged resonances are possible. (c) If bias is sufficiently high, excited states contribute to transport.

2.3.2 High interdot tunnel coupling: The molecular state

If the interdot tunnel coupling is high, the purely electrostatic model is not sufficient to describe the double dot. In our case of two coupled quantum dots which are occu-

pied by one electron each, we hence deal a priori with a two-electron molecular state. The state forms because the finite tunnel coupling allows each electron to penetrate into the adjacent quantum dot. Hence the two electrons are not distinguishable and a two particle-state is formed. The result is illustrated in figure (2.9(Right)). The square of the wave-function gives the probability distribution of where the electrons are located across the whole double dot.

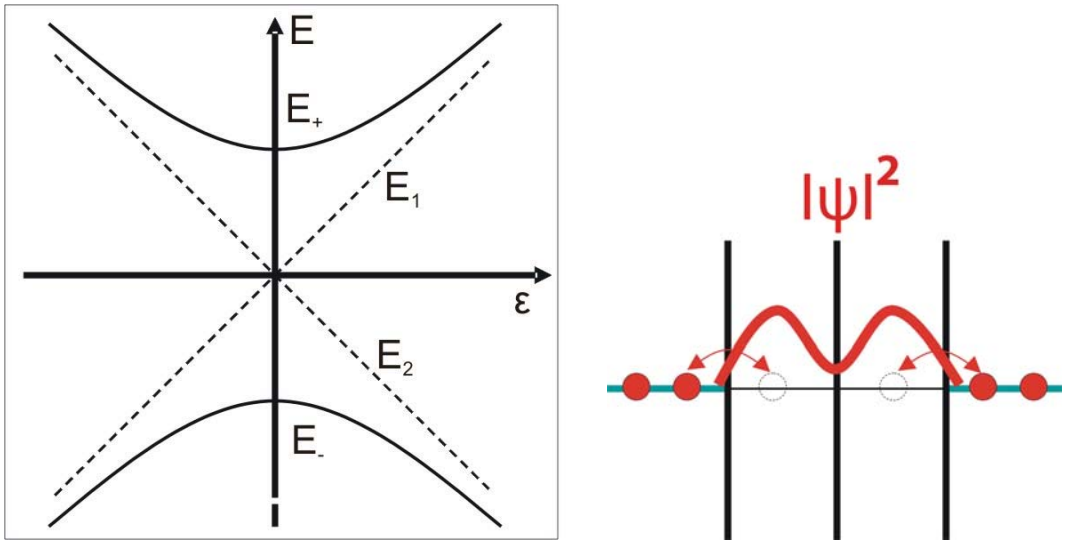

Figure 2.9: (Left) When tunnel coupling between the two dots of a double quantum dot is introduced, the single dot energies E_1, E_2 repel each other and form an anti-crossing with energies E_+, E_-. (Right) The new energy levels, referring to bonding and antibonding wave-function of a molecular state, are delocalized over the quantum dot. The square of the wave-functions describing the molecular state is the probability distribution where to find an electron.

The enhanced tunnel coupling also has an effect on the stability diagram. We assume that the electrostatic coupling is such that the stability diagram, when switching off the tunnel coupling, would look like figure (2.7(a)). In order to understand the effect of the tunnel coupling, we start the discussion with the textbook example of two tunnel-coupled energy levels. This is justified because in a simplified picture the discussion of the molecular state in a double quantum dot can be based on the elementary case of a quantum mechanical two-level system [86]. That means that we take into account only the topmost occupied level of each dot and neglect electrons in lower energy levels. Furthermore we do not consider excited states and assume that the electrostatic coupling of the quantum dots is zero. Only if transport occurs

in the two ground states of the dots, the picture is justified. The basic discussion of two tunnel-coupled energy-levels is presented e.g. in reference [88].
The uncoupled quantum dots have eigenstates $|\Phi_1\rangle$, $|\Phi_2\rangle$ and eigenvalues E_1, E_2. The two energies are illustrated on the energy axis E in figure (2.9(Left)) as a function of the energy difference

$$\epsilon = E_1 - E_2 \tag{2.19}$$

This energy difference between the levels of the two different dots is often called the axis of "detuning". The uncoupled system is described by a Hamiltonian $\hat{H}_0$:

$$\hat{H}_0 = \begin{pmatrix} E_1 & 0 \\ 0 & E_2 \end{pmatrix} \tag{2.20}$$

If we switch on tunnel-coupling between the two dots, we introduce a tunnel matrix $\hat{T}$. The total Hamiltonian of the system thus reads:

$$\hat{H} = \hat{H}_0 + \hat{T} = \begin{pmatrix} E_1 & 0 \\ 0 & E_2 \end{pmatrix} + \begin{pmatrix} 0 & t \\ t & 0 \end{pmatrix} = \begin{pmatrix} E_1 & t \\ t & E_2 \end{pmatrix} \tag{2.21}$$

The eigenstates of $\hat{H}$ are the delocalized molecular states $|\Psi_+\rangle$, $|\Psi_-\rangle$, corresponding to antibonding and bonding state, respectively. As can be seen in figure (2.9(Left)), the eigenenergies E_+, E_- of the total Hamiltonian seem to repel each other forming a so-called "anticrossing". The eigenvalues of $\hat{H}$ are:

$$E_\pm = \frac{E_1 + E_2}{2} \pm \sqrt{\frac{1}{4}(E_1 - E_2)^2 + t^2} \tag{2.22}$$

The energy difference E_Δ between bonding and anti-bonding state is a measurable quantity which can be used to determine the tunnel coupling between the two dots of a double quantum dot. Within this simplified picture, the energy difference is

$$E_\Delta = E_+ - E_- = \sqrt{(E_1 - E_2)^2 + 4t^2} = \sqrt{\epsilon^2 + 4t^2} \tag{2.23}$$

At $\epsilon = 0$, we obtain the minimal bonding-antibonding energy difference $E_\Delta = 2t$. Hence the tunnel coupling is responsible for a level repulsion of $2t$.

In a more realistic picture, the energy levels E_1 and E_2 are embedded in a double-well potential as given in figure (2.10).
As before, the interdot tunnel coupling is responsible for the formation of a molecular state, which is represented by bonding and antibonding state $E_\mp$. Moreover we identify the detuning ϵ as given in equation 2.19 as the energy difference between the single-dot energy levels E_1 and E_2. If we assume that the point $E = 0$ is equal

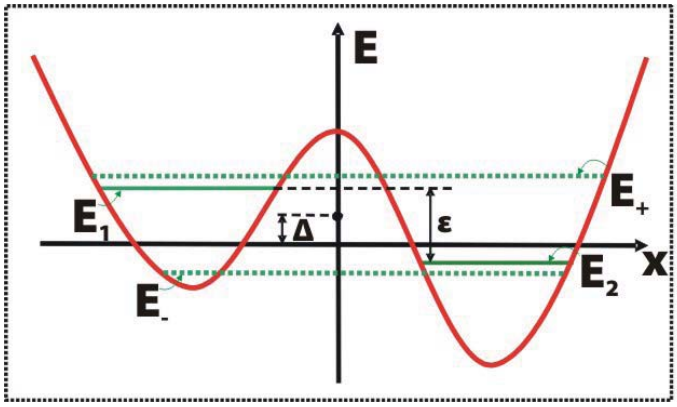

Figure 2.10: Double-well potential of a double quantum dot. At high interdot tunnel coupling, the two single-dot energy levels E_1 and E_2 form bonding and antibonding state $E_{\mp}$.

to the chemical potential of the leads at zero bias, the parameter Δ is defined as the energy shift of the whole double-well potential with respect to the chemical potential of the leads.

With these preliminaries we consider the stability diagram of a double quantum dot with strong tunnel-coupling depicted in figure (2.11(a)). We consider two adjacent triple points in the $V_{g1(2)}$ plane. In black solid lines, we illustrate the stability diagram without tunnel coupling. The separation of the two triple points is due to the electrostatic coupling U' of the two dots. Due to the tunnel coupling and the formation of a molecular state, the triple points split further and fall onto the two anticrossing lines illustrated in red colour. The anticrossing lines refer to bonding and anti-bonding state $E_{\mp}$ treated in figures (2.9) and (2.10). This time, however, E_+ and E_- are not only separated by the contribution $2t$ coming from the tunnel coupling but also by the contribution U' from the electrostatic coupling.

In figure (2.11(a)) the anticrossing is treated in the coordinate system (ϵ, Δ). The two parameters were defined in figure (2.10). The parameter ϵ is defined as the axis of detuning. If we walk along the axis labeled by this parameter in figure (2.11(a)), we decrease V_{g2} and increase V_{g1}. That means that we indeed move the energy levels of the two dots of the double quantum dot further apart and thus increase the detuning. If we increase V_{g2} and V_{g1} simultaneously, we increase the energy levels of both dots in the same way and thus move the whole double well potential with respect to the chemical potential of the leads. This refers again to the definition of Δ in figure (2.10) and thus it is justified to label the axis which runs perpendicular to the anticrossing lines in the stability diagram in figure (2.11(a)) with the very

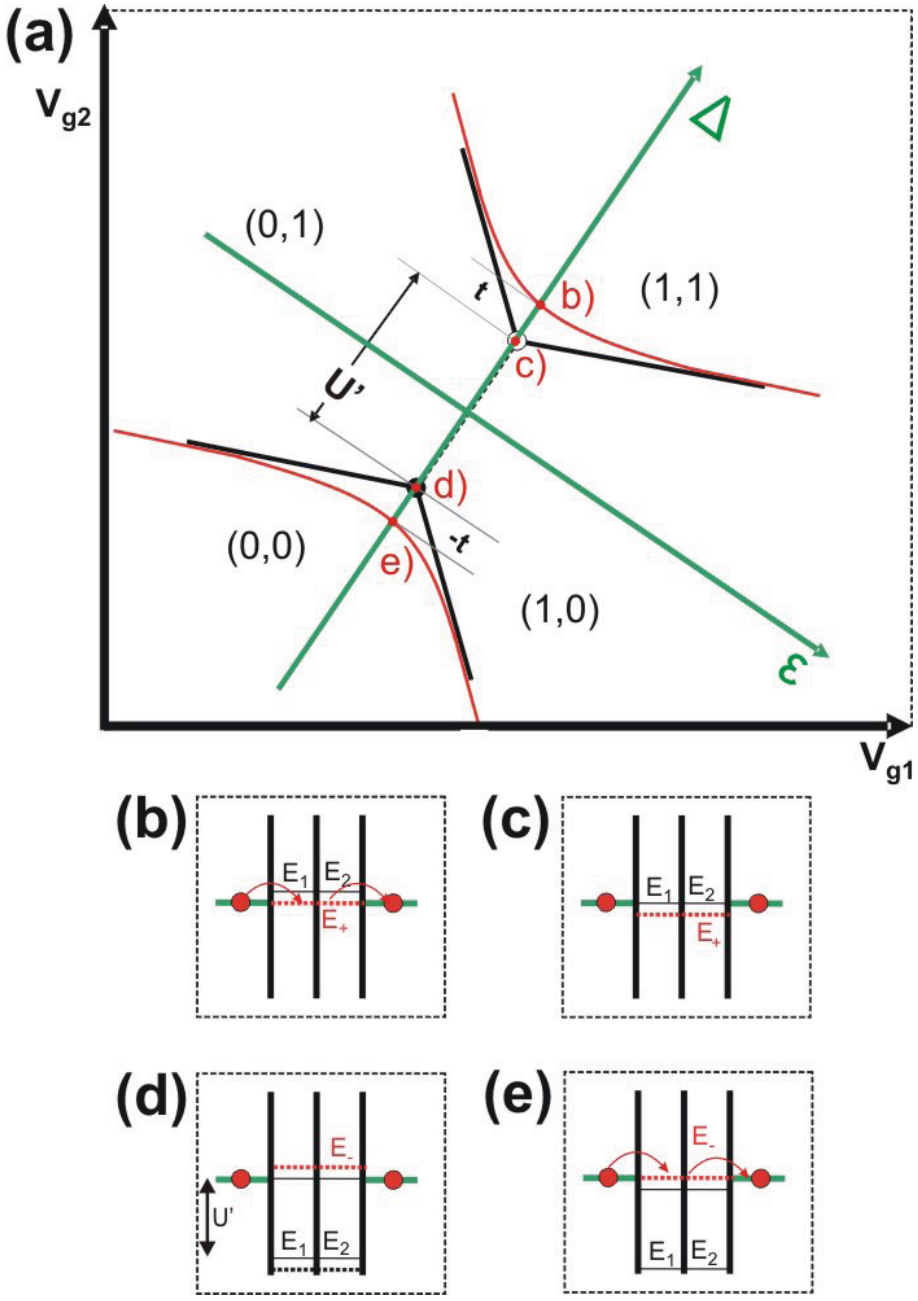

Figure 2.11: In real double quantum dots, the separation of the anticrossing lines has two reasons: Electrostatic coupling and tunnel coupling.

same symbol.

In order to understand in some more detail why the triple points move to the anti-

crossing lines, we consider the energy diagrams presented in figures (2.11(b)-(e)): In situation (b) the energy level corresponding to the antibonding state of the molecular state is aligned with the chemical potential of the leads. In situation (c) the single-dot energy levels would be aligned with the leads. As they do not exist any more in the case of high tunnel coupling, no transport is possible at this energy. If we continue along the axis Δ to point (d), we would have already paid the necessary energy to overcome U'. Though transport is not possible because once again, the single dot levels are not existent any more. The next accesible level is the bonding state E_- of the molecular state shown in figure (e). As a result we obtain the two anticrossing lines indicated by red colour in figure (2.11(a)).
The exact determination of the splitting and the identification of electrostatic and tunneling contribution is more complicated. In order to treat a real two-particle state, it is inevitable to take Coulomb repulsion and exchange interaction into account [49]. This leads to the exact expression of the separation E_Δ of the wings in the Δ-direction as a function of the detuning ϵ [22]:

$$E_\Delta = \sqrt{2}U' + \sqrt{4\epsilon^2 + 8t^2} \tag{2.24}$$

Again, U' is the electrostatic coupling and t is the tunnel coupling.

2.4 BCS-theory and the spin singlet state

2.4.1 The BCS ground state

In a very basic approach, a metal can be described as a free electron gas. In the ground state (meaning at T=0), all levels of the Fermi sphere $E_F = \frac{\hbar^2 k_F^2}{2m}$ are occupied. States above E_F are empty. In 1957, Bardeen, Cooper and Schrieffer [89] showed that in the presence of an attractive interaction, the free electron gas ground state becomes unstable. That means that the total energy of the system is lower than the ground state energy without interaction. As summarized e.g. in reference [90], the prove is straight forward.
Taking an electron pair outside the Fermi sea and furthermore assuming that its center of mass is at rest, the wave-function of the pair can be expanded in plane waves.

$$\Psi(\vec{r}_1 - \vec{r}_2) = \sum_k g(k) e^{i\vec{k}(\vec{r}_1 - \vec{r}_2)} \tag{2.25}$$

Thereby g(k) is the probability of finding electron 1 in state $\hbar\vec{k}$ and electron 2 in

state $-\hbar\vec{k}$. Next, the eigenvalues of Ψ are calculated using Schrödinger's equation for the problem:

$$-\frac{\hbar^2}{2m}(\nabla_1^2+\nabla_2^2)\Psi(\vec{r_1}\vec{r_2})+V(\vec{r_1}\vec{r_2})\Psi=(E+\frac{\hbar^2k_F^2}{2m})\Psi \tag{2.26}$$

The question is if there are solutions with $E<0$. Therefore we assume attractive interaction between two electrons with wavevectors $\vec{k}$, $-\vec{k}$, which only exists in a small sphere of width $\hbar\omega_D$ around E_F and has a constant value $V_{k,-k}=-\frac{V}{L^3}$. The parameter ω_D is named the Debye frequency and has to do with the nature of the assumed attractive potential. The physical idea of the attraction is that the electron going in direction $\vec{k}$ attracts positive ions of the solid. This creates an excess positive charge coming from the induced ions which attracts the electron with wave-vector $-\vec{k}$. Thus this effect results in a net attractive potential between the two electrons, given that the attractive interaction exceeds Coulomb repulsion. This is the case as long as the energy is smaller than the Debye energy $\hbar\omega_D$, which is the cutoff of the phonon spectrum.
Using this positive interactions, one can indeed find negative eigenvalues, where N(0) is the density of states at E_F.

$$E=-2\hbar\omega_De^{-2/N(0)V} \tag{2.27}$$

Thus we can conclude that the Fermi sea is not stable if we turn on a positive interaction at $T\mapsto 0$. That means that in superconductivity we obtain a new ground state, which is called the BCS-ground state. We are looking for a wave function of N electrons which are organized in pairs of two. Hence we are looking for a function of the form:

$$\Phi_N(\vec{r_1},\vec{r_2},...,\vec{r_N})=\Phi(\vec{r_1}-\vec{r_2})\Phi(\vec{r_1}-\vec{r_2})...\Phi(\vec{r_{N-1}}-\vec{r_N}) \tag{2.28}$$

We have to minimize the energy to find the BCS-ground state, look out that the wave function is antisymmetrized and introduce the spin part of the wave-function. Thereby electrons of the same pair have opposite spin. If we use a second quantization technique we can find the BCS-ground state in this way:

$$\tilde{\Phi}=\Pi_k(u_k+v_ka_{k\uparrow}^\dagger a_{-k\downarrow}^\dagger)\Phi_0 \tag{2.29}$$

with $\frac{v_k}{u_k}=g_k$ and $u_k^2+v_k^2=1$.
Note that g_k is the probability of finding a pair of electrons in state $k\uparrow$, $-k\downarrow$. Such a pair is called a Cooper pair. The two operators $a_{k\uparrow}^\dagger a_{-k\downarrow}^\dagger$ signify the creation of a Cooper pair.
Two electron spins forming Cooper pairs in an s-wave superconductor are entangled.

This can be shown from the two-electron space-spin density matrix which can be obtained from the BCS ground state using a two-particle Green's function [91]. In a simplified picture, Cooper pairs can be thought of spin singlet states (see equation (1.1)). Furthermore, in reference [92], the authors show that the entanglement of the spin-singlet state is conserved when the entangled state is injected into two adjacent quantum dots within a beamsplitter geometry.

2.4.2 Quasiparticles and the density of states

Excitations in a superconductor are mediated by fermion quasiparticles. It turns out, however, that excitations need to have a minimal energy above E_F in order to arise. This minimal energy defines the superconducting gap Δ_S. The gap is strongly temperature-dependent. As the derivation of the BCS ground state relies on the premise that $T \mapsto 0$, it is not astonishing that the superconducting gap vanishes at a critical temperature T_C. Superconducting gap and critical temperature are related by $\frac{\Delta_S(0)}{k_B T_C} = 1,764$, where k_B is Boltzmann's constant and $\Delta_S(0)$ is the superconducting gap at zero temperature. Furthermore the superconducting gap is a function of temperature. This function follows from BCS theory and can be computed numerically. The result is visible in figure (2.12(a)).
An arbitrary excitation in the superconductor has energy $E_k^2 = \Delta_S^2 + \zeta^2$, where ζ is the single particle energy relative to the Fermi-level. Equating

$$N_S(E)dE = N_n(\zeta)d\zeta \tag{2.30}$$

and assuming $N_n(\zeta)$ as constant, we obtain:

$$\frac{N_S(E)}{N(0)} = \begin{cases} \dfrac{E}{(E^2 - \Delta_S^2)^{1/2}} & (E > \Delta) \\ 0 & (E < \Delta) \end{cases} \tag{2.31}$$

We can thus plot the superconducting density of states (see figure 2.12(b)) as a function of energy. Clearly we observe the superconducting gap Δ_S.

2.4.3 Tunneling processes involving superconductors

An important issue in our beamsplitter experiment is the tunneling from the superconducting electrode into the normal lead. The situation can be understood visualizing sketch (2.12(c)) which shows the so-called Semiconductor model of N-S junctions. The normal metal is represented by a continuous distribution of independent-particle energy states. The superconductor is represented by an ordinary semiconductor with an independent-particle density of states given by equation 2.31. If no external

potential is applied, the Fermi-level of the normal metal lies in-between the superconducting gap. Only if an external potential is applied, electrons in the normal state can populate levels which are sufficiently high to overcome the gap and then tunnel into the superconductor.

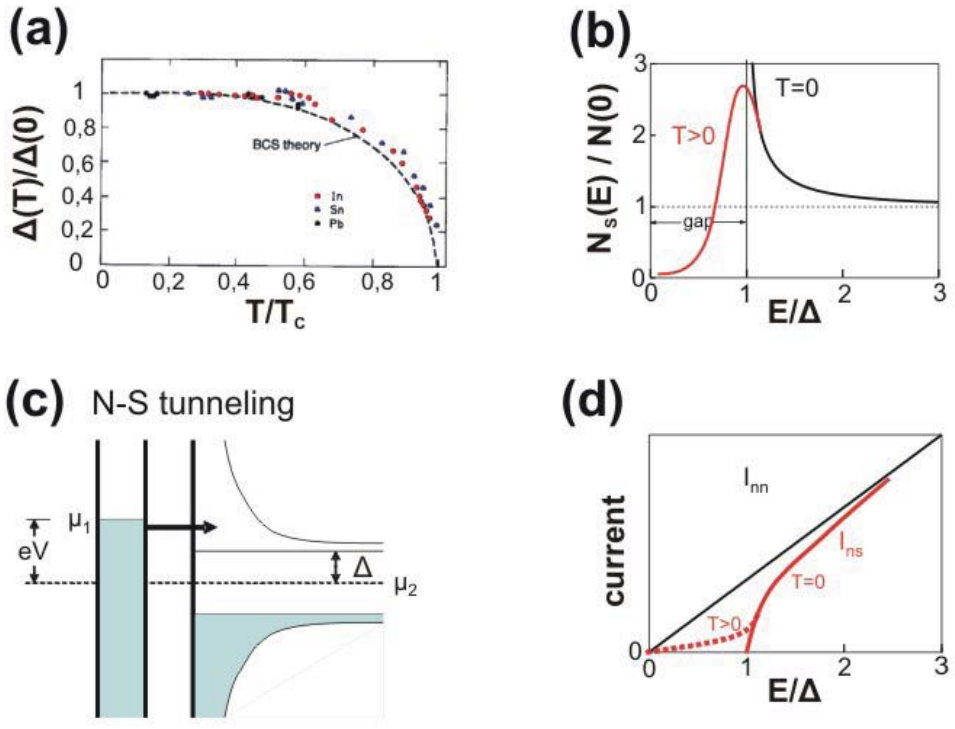

Figure 2.12: (a) Behavior of the superconducting gap if $T \mapsto T_C$ (taken from [93]). (b) The BCS density of states. The sharp peak at the gap edge is washed out for finite temperature. (c) Schematical illustration of tunneling processes at N-S junctions: The potential difference applied at the leads has to exceed the superconducting gap Δ_S. (d) I-V characteristic for a NS tunnel junction.

The expression for the tunnel current in a single particle picture thus reads:

$$I_{ns} = A \mid T \mid^2 N_n(0) \int_{-\infty}^{\infty} N_s(E)\Big[f(E) - f(E+eV)\Big]dE \tag{2.32}$$

where A is constant, $\mid T \mid^2$ is the tunnel probability, N_n and N_s are the densities of states in normal and superconducting region and f(E) is the Fermi-Dirac distribu-

tion. The result is plotted in figure (2.12(d)). The subgap current becomes finite as soon as we leave the zero temperature limit.

2.5 Injecting superconducting correlations in a normal conductor: Andreev Reflection

The picture of an NS junction given in the last section is simplified. The model used in figure (2.12(c)) to explain tunneling through an NS junction is called the semiconductor model. The model only treats quasiparticle excitations. If, however, the potential barrier between normal metal and superconductor is not too high, electrons coming from the normal metal can indeed enter the condensate of the superconductor. This process is known as Andreev Reflection [94] and is the only subgap transport that can occur at NS-junctions.

2.5.1 Andreev Reflection at an NS interface

The microscopic process which occurs at an NS boundary is sketched in figure (2.13(a)). An incoming electron with spin up and an energy $E_i < \Delta_S$ approaches the interface in the normal metal. In order to enter the Cooper pair condensate, it needs a second electron of opposite spin. This process is maintained by the reflection of a hole into the normal metal. Note that spin, momentum, energy and charge are conserved. Therefore a hole with spin down traces back the time-reversed path of the incoming electron.

As depicted in figure (2.13(b)), Andreev Reflection at the NS-interface can be described by a scattering matrix approach [95]. At the interface, normal scattering as well as Andreev Reflection occurs. Owing to an idea of Beenakker [80], the problem can be separated into two parts: the normal scattering is thought of as slightly displaced from the junction into the normal metal. The Andreev Reflection is assumed to take place at the interface. Therefore one can write two scattering matrices. The first matrix $\hat{S}_N$ connects the ingoing $(I_1^e, I_1^h, I_2^e, I_2^h)$ and outgoing $(O_1^e, O_1^h, O_2^e, O_2^h)$ states from the "normal" scattering, for both electrons and holes:

$$\begin{pmatrix} O_1^e \\ O_1^h \\ O_2^e \\ O_2^h \end{pmatrix} = \begin{pmatrix} r_{11}(E) & 0 & t_{12}(E) & 0 \\ 0 & r_{11}^*(-E) & 0 & t_{12}^*(-E) \\ t_{21}(E) & 0 & r_{22}(E) & 0 \\ 0 & t_{21}^*(-E) & 0 & r_{22}^*(-E) \end{pmatrix} \begin{pmatrix} I_1^e \\ I_1^h \\ I_2^e \\ I_2^h \end{pmatrix} \tag{2.33}$$

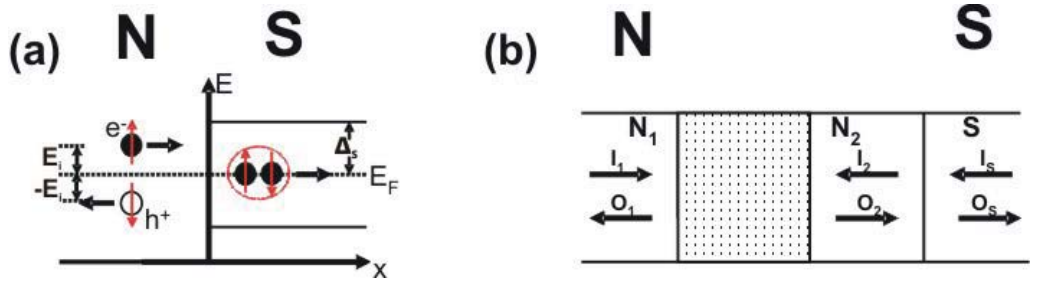

Figure 2.13: In figure (a) an incoming electron from the normal metal side at energy ϵ is converted into a Cooper pair in the superconductor. The missing electron of opposite spin is symbolized by a retroreflected hole at energy $-\epsilon$. Thus charge, momentum, energy and total spin are conserved. In figure (b) the same situation is shown within a scattering matrix approach. Owing to the idea in reference [80] the normal region is divided into three regions: Normal scattering takes place in the shaded region which is slightly removed from the NS-interface. Thus, at the NS-interface, Andreev-reflection is the only scattering mechanism. In this way the scattering matrix can be divided into two separate parts.

The parameters $r_{11}(E), t_{12}(E), r^*_{11}(-E), t^*_{12}(-E), t_{21}(E), r_{22}(E), t^*_{21}(-E), r^*_{22}(-E)$ are transmission and reflection amplitudes of incoming and outgoing particles. (For simplicity, we assume to have only one conduction channel: $N = 1$).
In a similar way we can construct a matrix $\hat{S}_I$ for the Andreev Reflection at the NS-Interface:

$$\begin{pmatrix} I_2^e \\ I_2^h \\ O_S^e \\ O_S^h \end{pmatrix} = \begin{pmatrix} \hat{r}_I(E) & \hat{t}'_I(E) \\ \hat{t}_I(E) & \hat{r}'_I(E) \end{pmatrix} \begin{pmatrix} O_2^e \\ O_2^h \\ I_S^e \\ I_S^h \end{pmatrix} \tag{2.34}$$

The matrices $\hat{r}_I(E), \hat{t}'_I(E), \hat{t}_I(E), \hat{r}'_I(E)$ are 2×2 scattering matrices which connect ingoing and outgoing states from the Andreev Reflection process.
In order to calculate the full current-voltage characteristic of the junction, the matrices $\hat{S}_N$ and $\hat{S}_I$ have to be combined. From this we obtain the total conductance G_S across the junction which can then be inserted into the relation for the current:

$$I = \int dE \frac{1}{e}[f(E) - f(E + eV)]G_S(E, V) \tag{2.35}$$

where $f(E)$ is the Fermi-Dirac distribution.
In the linear response limit ($E \to 0$) of the Andreev Approximation [95], the total

conductance G_S for a single channel simplifies to:

$$G_S = \frac{4e^2}{h} \frac{T(0)^2}{[2 - T(0)]^2} \tag{2.36}$$

Here, $T(0)$ is the transmission probability through the whole system at $E = 0$.
The full derivation to obtain this result would exceed the scope of this thesis. The interested reader is referred to reference [80].

2.5.2 Crossed Andreev Reflection

In the last subsection the Andreev Reflection process was introduced. Next we consider a special type of Andreev Reflection which is called Crossed Andreev Reflection (CAR). In this process an incoming electron in normal lead 1 groups together with a second electron from normal lead 2 to travel as a Cooper pair in the superconductor. Thus a hole is reflected in normal lead 2. The incoming electron and the reflected hole are spatially separated and hence the phenomenon is often called non local Andreev Reflection [96], [97]. The process is illustrated e.g. in figure (2.14(a)).
In order to make Crossed Andreev Reflection possible, different sample designs have been implemented (see figures 2.14(a)-(c)). In figure (2.14(a)) and figure (2.14(c)) the three terminal structure connecting two normal conductors to a superconductor is defined by a lithographical process. The CAR process happens in the surface plane of the device. In figure (2.14(b)) the situation is different: The superconductor is sandwiched in z-direction between two normal metal layers. The latter process requires only optical lithography. An important choice is the material which is used as superconductor. Straight forward candidates are Aluminum and Niobium. Niobium has a critical temperature of 9,2K and a critical field of 195mT. Aluminium has a critical field of 10mT and a critical temperature of 1,2K. The given values apply to bulk materials and can vary drastically if thin films are considered [98]. The values are taken from reference [99].
The idea of measuring non local Andreev Reflection works as follows (see for instance figure 2.14(b)): A bias current is maintained between normal lead N_1 and the superconductor. As can be seen in figure (2.15 (up right)) the hole which is reflected into normal lead N_2 has exactly the same energy as the incoming electron, however with opposite sign. Thus a negative non local voltage is detected if non local Andreev Reflection takes place.
The problem is that CAR is not the only process that is possible. A second process called Elastic Cotunneling is illustrated in figure (2.15(up left)). In this process the incoming electron from normal lead N_1 crosses the superconductor via a virtual state and impinges into the second normal metal N_2, creating thus a positive non

local voltage.
When injecting electrons in the normal lead and measuring the non local voltage between the second normal lead and the superconductor (as is illustrated in figures 2.14(a)-(c)), CAR and Elastic Cotunneling are always in competition. Only if one obtains a negative signal, one can be sure that CAR exceed Elastic Cotunneling. The ratio between the two, however, can hardly be determined. In order to find a configuration in which CAR dominate, different approaches have been made: In reference [100] the authors make the superconducting sandwich layer between the two normal metals as small as possible. Kleine et al. [101] study the strength of the tunnel barriers between normal leads and the superconductor and finally find a regime where negative non local voltage is observed. In references [102], [103], [104] the authors use ferromagnetic normal leads to favor CAR. Using one of these methods, one can find results as illustrated in figure (2.15(down)) which corresponds once again to sample design (2.14(b)). Whereas Elastic Cotunneling dominates at zero bias, the authors find a bias window around $0.4mV$, in which CAR clearly dominate Elastic Cotunneling.
In the final analysis it can be concluded that within the experiments presented in this subsection, the equilibration of CAR and Elastic Cotunneling is not yet understood. The influence of electron-electron interaction [105], for example, is not explained to a great extent.

2.6 Putting the puzzle together: Theoretical description of the beamsplitter

The last sections gave an overview over the theoretical concepts necessary to understand the Carbon Nanotube beamsplitter as presented in this work. Now we apply the concept of CAR to our sample. As explained above, CAR consist of an incoming electron in one normal lead, a reflected hole in the second normal lead and a Cooper pair traveling out of the structure via a superconducting electrode (see for instance 2.14(a)). The outgoing hole in the right arm of figure (2.14(a)) can also be represented by an incoming electron, as done in figure (2.16(a)). Hence two incoming electrons from different leads unite to form a Cooper pair in the superconductor. If the situation is time-inversed, i.e. a Cooper pair is injected in the superconducting electrode, the beamsplitter idea becomes visible (see figure 2.16 (b)). An incoming Cooper pair from a superconducting electrode is split in two different normal leads. Thus the CAR process is equivalent to our beamsplitter.
However, when injecting a Cooper pair, electrons do not split automatically in two different leads. As can be seen in figure (2.17), the two electrons either split into

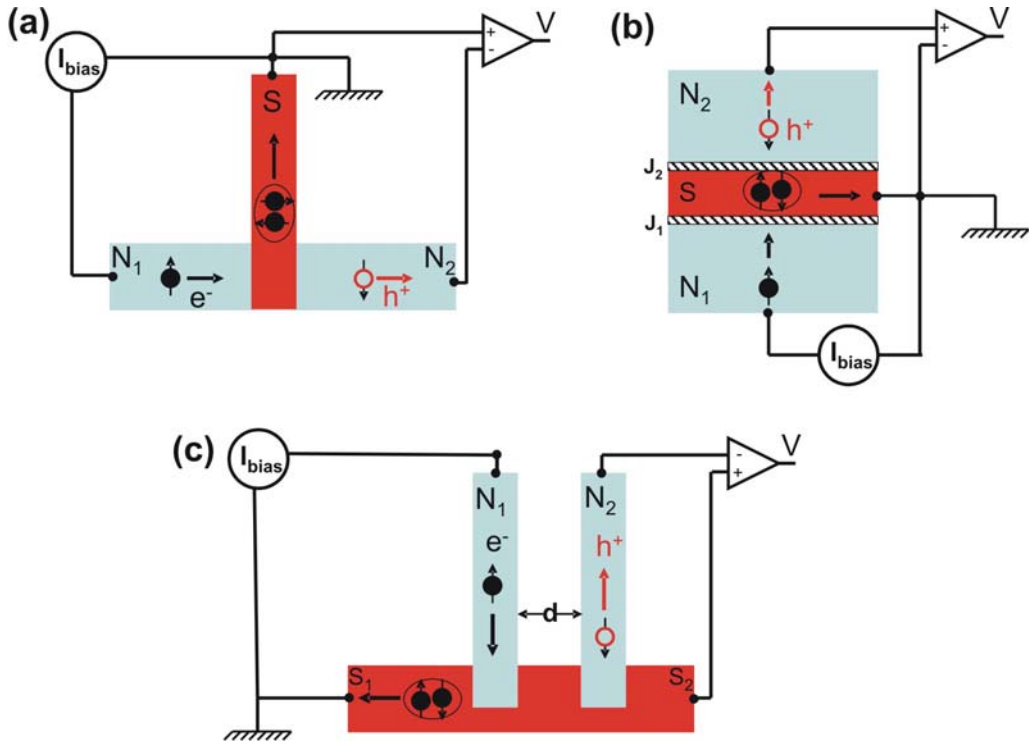

Figure 2.14: Crossed Andreev Reflection illustrated in three different sample geometries. Sample (a) describes the beamsplitter setup (topview), sample (b) describes the sample used by Russo et al. [100](crosssection) and sample (c) describes the sample of Eichler et al. [101] (topview).

two different leads (Process 2) or they tunnel to the same lead (Process 1). This fact defines two major tasks of our experiment: First we have to find a method how to favor Processes 2 and suppress Process 1. Furthermore we have to find a method to show that CAR do indeed contribute to transport in our device. Second, Local and Crossed Andreev Reflection will always superimpose. Thus we have to look for a way to extract and evaluate the contribution of CAR to the total transport.

Concerning the first task, i.e. the effective splitting of the pair, different suggestions have been made. The use of ferromagnetic normal leads [102], energy filtering with a single quantum dot [106], and the coupling of the superconductor to two Luttinger liquid leads [62], [107] are pointed out promising candidates. We follow a proposal by Recher et al. [108] and Bouchiat et al. [70], where a double quantum dot is used to effectively split the pair. That means that the normal metal within the proposal given in figure (2.14(a)) is disrupted by a quantum dot on each side.

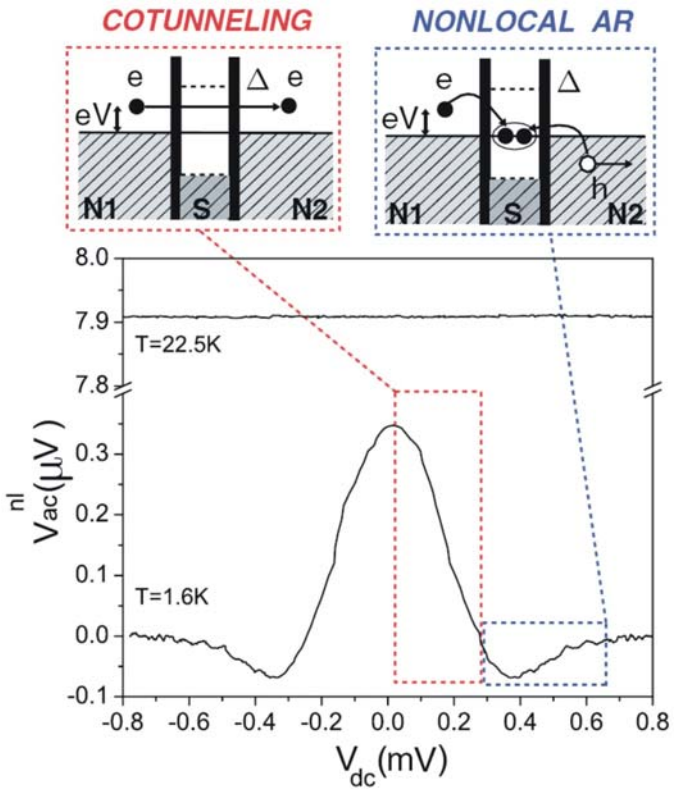

Figure 2.15: The figure is taken from reference [100]. The two energy diagrams on top illustrate the two competing processes found in Crossed Andreev samples as illustrated in figure (2.14). Cotunneling leads to a positive non local voltage whereas Crossed Andreev Reflection produces a negative non local voltage. The experimental task is to find a configuration in which CAR exceeds Cotunneling. In the measurement by Russo et al. [100], Cotunneling dominates at zero bias. Increasing the source-drain voltage, one can find symmetric dips of negative non local voltage signifying Crossed Andreev Reflections.

The corresponding sketch is depicted for instance in figure (2.17). We expect that the contribution from Elastic Cotunneling, (i.e. the tunneling from left to right normal lead via a virtual state) is less important here, as we apply positive bias to the superconducting contact whereas both normal leads are grounded. Electrons traveling between normal leads would henceforth have to overcome the potential difference between normal reservoir and superconductor which makes this process less probable. In order to give evidence for split Cooper pairs, we introduce an analysis tool in subsection 2.6.1. In a second step we will deal with the second task, i.e the quantitative evaluation of CAR contribution to the total conductance. We will

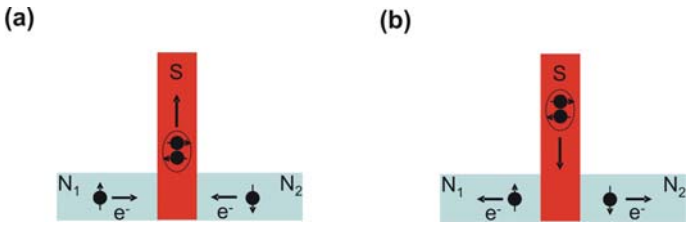

Figure 2.16: (a) An outgoing Cooper pair is created by two incoming electrons from different normal leads. (b) By time-inversion the outgoing Cooper pair becomes an incoming Cooper pair: The Crossed Andreev Reflection can thus be interpreted as the splitting of the electrons of the Cooper pair in two different normal leads.

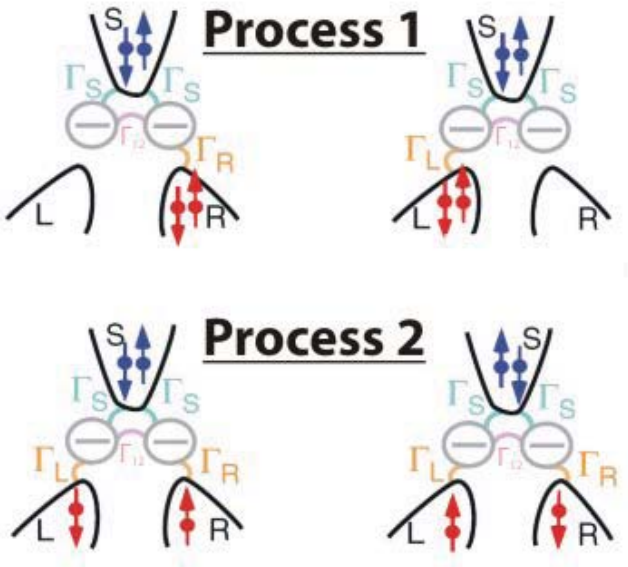

Figure 2.17: The figure illustrates the competing processes in our double dot beam-splitter. Process 1 shows how both electrons of an incoming Cooper pair tunnel to the same normal contact. Process 2, on the contrary, illustrates Crossed-Andreev Reflection.

present the basic results of the corresponding theory in subsection 2.6.2.

2.6.1 Qualitative Theory and Splitting argument

The basic ingredient for the argument is the conductance ratio between left and right normal lead while injecting in the middle contact of our beamsplitter device. It turns out that this ratio is highly sensitive with respect to magnetic field and gate voltages:
The magnetic field is used to switch the superconducting middle contact into the normal state. Hence charge transport is changed from Andreev Reflection to regular transmission. This has an important effect on the conductance ratio between left and right lead as will be explained below.
Furthermore we can tune the two sidegates attached to the double dot such that either no, one or two quantum dots are at resonance. In the superconducting case, this makes a decisive difference for the conductance ratio between left and right dot. Below, we explain the reason for this behavior.
In figure (2.18) we show the transport mechanisms in our CNT-beamsplitter device at finite magnetic field ($B = 89mT$).
This magnetic field is higher than the critical field of aluminum and thus the aluminum contact is in the normal state. Transport is mediated by single particle tunneling. In figure (2.18(left)), the side gate voltages are such that the beamsplitter is on a single resonance (see figure (2.18top)). In the illustrated case, the left quantum dot is at resonance whereas the right dot is off resonance. Injecting electrons in the middle contact, the particles can only tunnel to the left lead. The coupling energy between left quantum dot and left lead is defined as Γ_L. Hence the conductance G_L measured at the left lead can be written as: $G_L \sim \Gamma_L$. If the right dot is at resonance and the left dot off resonance (not shown in the figure), we can write analogously: $G_R \sim \Gamma_R$.
If both dots are at resonance (see figure 2.18(right)), i.e. we measure on a triple point within the stability diagram (see figure (2.18top)), we obtain the same expressions for the conductance at left and right lead: $G_{L,R} \sim \Gamma_{L,R}$. The reason is that tunneling to the left lead is independent from tunneling to the right lead. Both processes are single particle processes.
If we define the conductance ratio in the normal state between left and right lead as α_N, we obtain for both single resonances and triple points:

$$\alpha_N = \frac{G_R}{G_L} = \frac{\Gamma_R}{\Gamma_L} \tag{2.37}$$

In the superconducting state at zero magnetic field, the situation changes as depicted in figure (2.19). In this case, a fundamental difference between single resonances and triple points can be predicted:
At the NS-interface, transport is possible via Andreev Reflection which is essentially

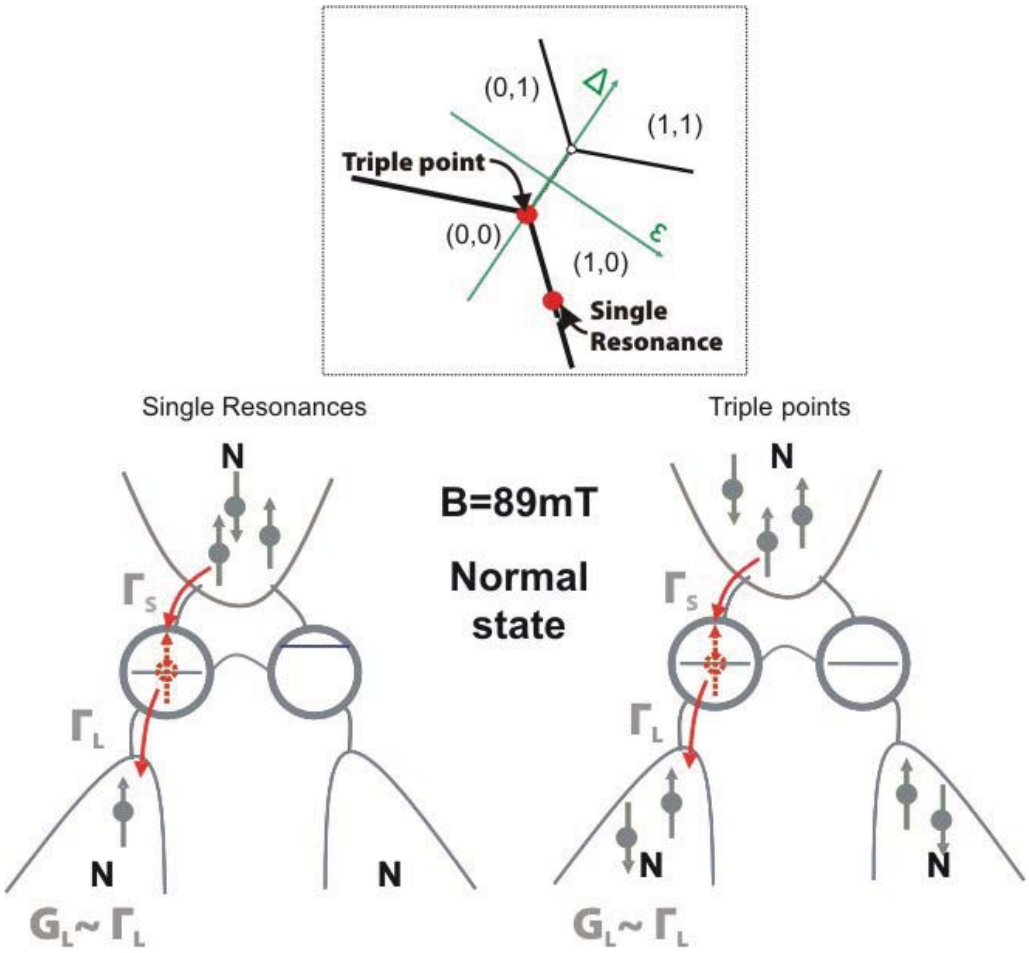

Figure 2.18: At $B = 89mT$, the Aluminum contact is in the normal state. Hence only single particle tunneling contributes to transport and the conductance measured at the left lead is proportional to the coupling energy of the left lead. Therefore it makes no difference if we measure the conductance at a single resonance or at a triple point.

a two-particle process. At a single resonance (2.19(left)), only local Andreev Reflection is possible. Hence the conductance at left lead and right lead (not shown) are

$$G_L \sim \Gamma_L^2 \tag{2.38}$$

$$G_R \sim \Gamma_R^2 \tag{2.39}$$

If we define the conductance ratio α_S in the superconducting case between left and

right lead, we obtain:

$$\alpha_S = \frac{G_R}{G_L} = \frac{\Gamma_R^2}{\Gamma_L^2} = \alpha_N^2 \tag{2.40}$$

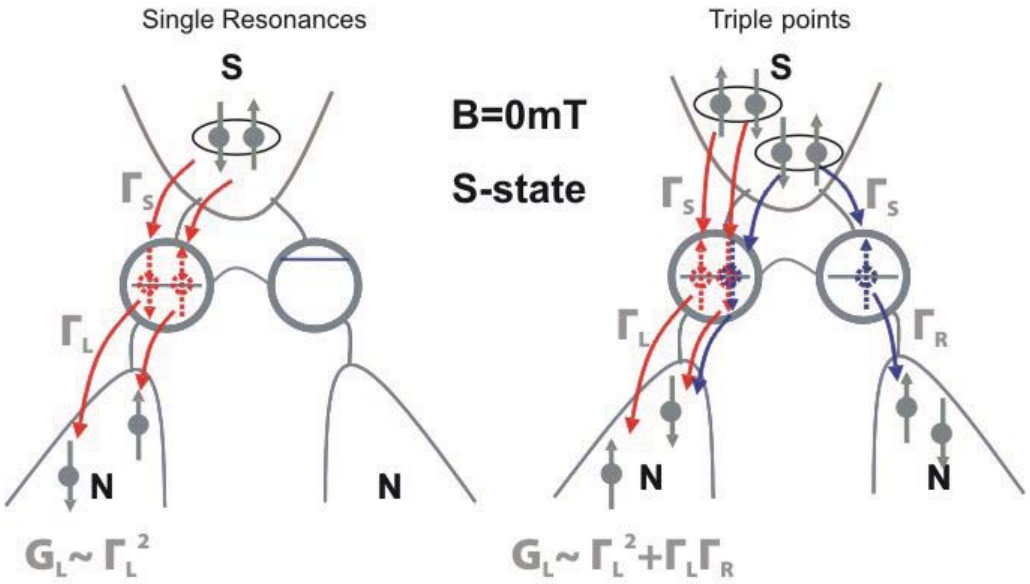

Figure 2.19: At zero magnetic field, the aluminum contact is superconducting. Hence we can only inject Cooper pairs which can tunnel to the normal leads via the Andreev Reflection process. In contrast to the normal case, charge transport is mediated by a two-particle tunneling process. That means that the conductance measured at the left lead is proportional to the square of the involved tunnel rates. In this case we observe a fundamental difference between the single resonances and the triple points. At the triple points we expect an additional term in the conductance which comes from CAR processes.

At the triple points (see figure 2.19(right)), local Andreev Reflection (red arrows) is not the only possible charge transport. Here, Crossed Andreev Reflection is possible, too (blue arrows). To simplify the argument, we assume that the two normal leads have the same coupling Γ_S to the superconducting electrode. The CAR process is responsible for an additional term in the conductance expression for the conductance at left and right lead, respectively. As CAR can be interpreted as the tunneling of the two electrons of the same Cooper pair to two different leads, this adds a crossed term $\sim \Gamma_R\Gamma_L$ to the conductance. Thus we obtain for the conductance at left and

right lead, respectively:

$$G_{L,R} \sim \Gamma_L \Gamma_R + \Gamma_{L,R}^2 \tag{2.41}$$

If we compute the conductance ratio α_S between left and right lead in the superconducting case at the triple points, we obtain:

$$\alpha_S = \frac{\Gamma_R^2 + \Gamma_L \Gamma_R}{\Gamma_L^2 + \Gamma_L \Gamma_R} = \alpha_N \tag{2.42}$$

That means that α_S as a function of α_N is sensitive to the fact whether CAR contribute to the total transport or not. If CAR do contribute, α_S as a function of α_N defines a linear function. If CAR do not contribute and only local Andreev Reflection is present, α_S as a function of α_N is a parabola.
That means that the basic analysis tool introduced in this subsection works as follows: We have to determine the ratios α_S and α_N for a large number of triple points. If CAR contribute to the charge transport, α_S as a function of α_N for all these points will describe a linear function.
In a second step we carry out the same analysis for several single resonances: Here, as only local Andreev Reflection is possible, α_S as a function of α_N must define a parabola.

2.6.2 Methods to obtain the Γ's

In the paper resulting from this thesis [109], our measurement data is not only analyzed qualitatively as described in the last subsection, but also fitted quantitatively by a model developed by our co-worker Alfredo Levy-Yeyati (see reference [110] and Supplementary Information of reference [109]). In this subsection we give an overview over the underlying physical concept and comment on the procedure which extends the concept to model the differential conductance in our beamsplitter in the middle-injection setup.
As was pointed out in subsection 2.1.2, the differential conductance across a quantum conductor is proportional to the transmission probability T. Hence we have to look at the transmission probability in some more detail. The transmission probability depends on the potential landscape which an incident particle faces while passing through the conductor. Starting from textbook knowledge [111], a noninteracting quantum dot can be seen as a potential well as illustrated in figure (2.20(b)).
We are interested in the transmission probability T(E) for a particle incident from region I. The transmission probability defines the probability with which the incident particle tunnels through the potential and arrives at region III.

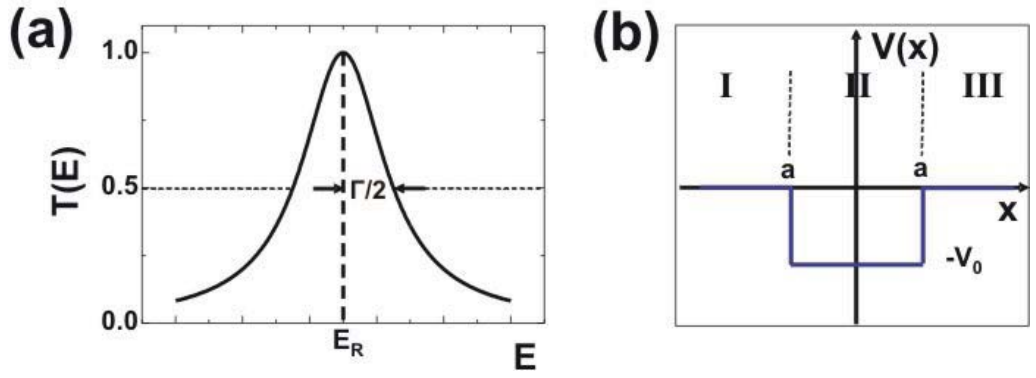

Figure 2.20: (a) The line shape of the transmission probability around a resonance E_R is given by the so-called Lorentzian or Breit-Wigner function. (b) In a very basic approach, a quantum dot can be modeled as a potential well.

In textbooks [111] one obtains the so-called Lorentzian or Breit-Wigner function as an approximation in the vicinity of a transmission resonance:

$$T(E) = \frac{(\Gamma/2)^2}{(E - E_R)^2 + (\Gamma/2)^2} \tag{2.43}$$

As can be seen in figure (2.20(a)), the parameter $\Gamma/2$ describes half of the width of the resonance at $T(E) = 1/2$. For $V_0 \gg E_R$ the parameter Γ is given by :

$$\frac{2}{\Gamma} \simeq \frac{\sqrt{2mV_0}a}{2\hbar}\frac{1}{\sqrt{V_0 E_R}}. \tag{2.44}$$

Hence $\Gamma = \Gamma(E_R, V_0, a)$ is a function depending on the resonant energies and on the width and height of the potential well. As Γ is the decisive parameter of the transmission probability, it can be understood as the coupling energy of regions I and III.
In figure (2.21), the carbon nanotube quantum dot is modeled by a more realistic potential which takes into account that the nanotube is coupled to the leads via two different tunnel barriers. To simplify the calculation, the two tunnel barriers are approximated by two Dirac δ-functions. The left tunnel barrier is situated at $x = 0$ and the right barrier at $x = L$. Schrödinger's equation for the problem thus reads:

$$-\frac{\hbar^2}{2m}\nabla^2\Psi(x) + V_L\delta(x)\Psi(x) + V_R\delta(x - L)\Psi(x) = E\Psi(x) \tag{2.45}$$

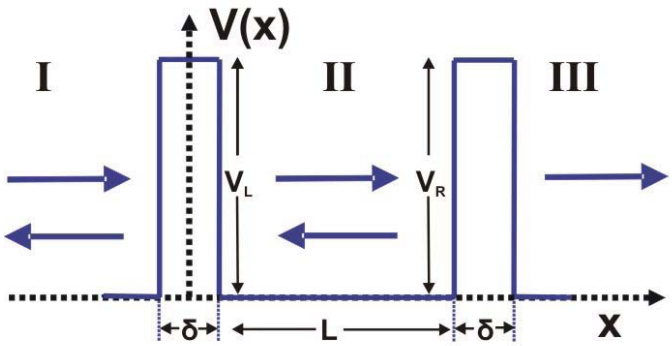

Figure 2.21: Our Carbon nanotube quantum dot is modeled by two potential barriers which can be approximated as Dirac δ-functions. We calculate the transmission probability for incoming particles with an energy $E > 0$.

We make a similar Ansatz as before for the wavefunction $\Psi(x)$ in the three regions defined in figure (2.21). The boundary conditions deliver 4 equations which allow to determine the transmission probability $T(E)$. The result has a Breit-Wigner like shape:

$$T(E) = \frac{\Gamma_L \Gamma_R}{(E - E_R)^2 + (\frac{\Gamma_L + \Gamma_R}{2})^2} \tag{2.46}$$

The only difference to equation 2.43 is that two coupling energies Γ_L, Γ_R are involved which describe the coupling to left and right lead, respectively.
Next these basic considerations have to be extended to a three terminal situation. Furthermore scattering at normal-superconductor junctions, as introduced in subsection 2.5.1, has to be taken into account. Finally, Coulomb interaction has to be considered. This last ingredient allows only numerical solutions for the full problem. However, as described in the qualitative argument given in the last subsection, our main argument is based on the peak values of the zero bias conductance resonances. Our co-worker Alfredo Levy-Yeyati could extract the expressions for the peak values of the zero bias differential conductance in both normal and superconducting state. The relevant parameters are the coupling energies of left and right dot to left and right lead (Γ_L, Γ_R), the coupling energies of left and right dot to the superconducing lead $(\Gamma_{SL}, \Gamma_{SR})$ and the intermediate coupling of the two dots Γ_{12}. The results are summarized below.

In the superconducting state, the peak values for the zero bias differential conductance at left and right lead (G_L, G_R) can be evaluated in the middle-injection setup.

To obtain this result, it is assumed that $\Gamma_{SL} = \Gamma_{SR} = \Gamma_S$. Furthermore the coupling to the superconductor is renormalized with respect to the induced gap in the dots by $\tilde{\Gamma}_S = \Gamma_S - \Delta_{induced}$. The result is valid for $\Gamma_{12} \gg \Gamma_{L,R} \gg \Gamma_S$. In this case the peak values of $G_{L(R)}$ read:

$$G_{L(R)} = \frac{4e^2}{h} \frac{16\tilde{\Gamma}_S^2}{(\Gamma_L + \Gamma_R)^4} (\Gamma_{L(R)}^2 + \Gamma_L \Gamma_R) \tag{2.47}$$

Furthermore the peak values of the transmission coefficients to left and right lead can be dissociated into the contribution of local Andreev Reflection ($AR_{L,R}$) and Crossed Andreev Reflection (T_{CAR}):

$$AR_{L,R} = \frac{4\tilde{\Gamma}_S^2 \Gamma_{L,R}^2}{[\Gamma_L + \Gamma_R]^4} \frac{[\Gamma_{L,R}^2 + \Gamma_L \Gamma_R + 2\Gamma_{12}^2]^2}{[\Gamma_{12}^2 + \Gamma_L \Gamma_R]^2} \tag{2.48}$$

$$T_{CAR} = \frac{4\Gamma_{12}^2 \tilde{\Gamma}_S^2 \Gamma_L \Gamma_R}{[\Gamma_L + \Gamma_R]^4} \frac{[(\Gamma_L + \Gamma_R)^2 + 4\Gamma_{12}^2]}{[\Gamma_{12}^2 + \Gamma_L \Gamma_R]^2} \tag{2.49}$$

Within these expressions, we can identify terms $\sim \frac{\Gamma_L \Gamma_R}{(\Gamma_L + \Gamma_R)^2}$ which, according to equation 2.46, are typcial for Breit-Wigner behavior.

In the normal state, in the limit $\Gamma_{12} \gg \Gamma_{L,R} \gg \Gamma_S$, Alfredo Levy-Yeyati obtains for the peak values of the zero bias differential conductance at left and right lead:

$$G_{L(R)} = \frac{2e^2}{h} \frac{4\Gamma_{L(R)} \Gamma_S}{(\Gamma_L + \Gamma_R + 2\Gamma_S)^2} \tag{2.50}$$

The peak values of $G_{L(R)}$ in normal and superconducting state as well as the peak values for T_{CAR} and $AR_{L,R}$ are of high importance.
From the expressions for the differential conductance, it can be confirmed for $\Gamma_{12}^2 \gg \Gamma_L \Gamma_R$ that α_S as a function of α_N is a linear function at the triple points and a parabola at single resonances.
The expressions which quantify the contribution of Local and Crossed Andreev Reflection allow to define an efficiency of the beamsplitter in the superconducting state at the resonances: The contribution of CAR to the total transmission is divided by the total transmission. Due to the expressions 2.48 and 2.49, the efficiency of the beamsplitter at the zero bias resonances of the differential conductance is:

$$Efficiency \equiv 2T_{CAR}/(AR_L + AR_R + 2T_{CAR}) \simeq 2/(2 + 1/\alpha_S + \alpha_S) \tag{2.51}$$

In this way we can define a splitting efficiency at each triple point. This is an important tool because high splitting efficiencies are highly desirable. The reason is

that in future experiments only split pairs are of interest. If we assume that we find a way to separate the split pairs from the rest of the current, we still face the following problem: As the total current through the Carbon nanotube beamsplitter is expected to be very low, i.e. on the order of $0,5nA$ for an excitation of $V_{ac} = 10\mu eV$, a low splitting efficiency would leave a very small signal with a very bad signal to noise ratio. Hence further analysis of the split pairs would be very difficult.

Chapter 3

Sample preparation and Measurement environment

We use Carbon nanotubes synthesized on a SiO_2 wafer by Chemical Vapor Deposition (CVD) [112] . Next we pattern alignment marks and detect the Single-Walled Carbon nanotubes with respect to the marks with a Scanning Electron microscope. In a further step we use electron beam lithography and evaporation techniques to contact our three terminal Single-Walled Carbon nanotube devices. A picture in false colours is shown in figure (3.1). The following sections give some more detailed insight in the different steps of the fabrication process.

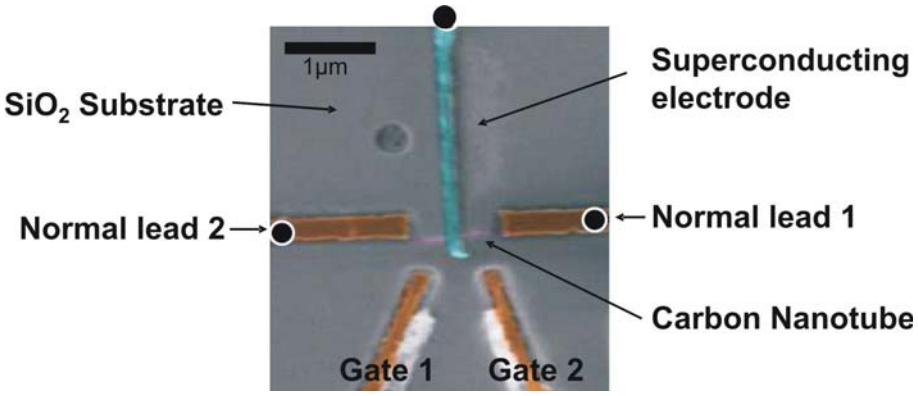

Figure 3.1: A typical Single-Walled Carbon nanotube beamsplitter sample. The different parts of the sample are illustrated by false colours. The picture was taken with a standard Scanning Electron Microscope.

3.1 CVD growth

We use doped Si wafers with a $300 - 500nm$ oxide layer on top. The oxide layer is a gate dielectric which isolates the contacts from the silicon bulk. Hence the doped silicon can be used as a backgate.
As a first step we cut the wafer into small pieces which fit into our chip-carrier. Next we exhaustively clean the surface by using oxygen plasma (5 minutes) as well as sonication in both acetone and propanol (10 minutes each). Once the surface is clean we deposit catalyst particles which stimulate the growth of our tubes. The recipe of the catalyst is given in appendix A. Before depositing the catalyst on the lithographically designed pattern (see next section), the catalyst is put in ultrasonics for at least 30 minutes. Moreover the catalyst should be either changed regularly (every two months) or kept on a permanent stirring machine.
After the catalyst deposition the sample is baked 5 minutes at 150 degrees Celsius. Then we carry out the lift-off (see next section). Only at the predefined spots, where there is no PMMA, the catalyst sticks to the surface. Everywhere else the catalyst is washed away again. We use an acetone-spray-bottle in the beginning and then toss the sample in hot acetone for 3 minutes. It turned out that the lift-off works better if the used PMMA-layer (see next section) is very thick. The use of a double PMMA layer is thus recommended.
Prepared in this way, the sample is put in the CVD-furnace. The cylindrical oven heats up the sample to 900 degrees Celsius. Thereby it is important that the sample is inside a quartz tube under a closed atmosphere of flowing gas. To heat up the sample, argon is used to ensure an inert atmosphere. Then methane is used as a carbon feedstock for the nanotubes during the growth process. Additionally, a slow flow rate of hydrogen is added which is supposed to favor growth conditions. Its role, however, is not entirely clear. After the growth process the sample is cooled down in argon atmosphere. The detailed growth recipe is given in the appendix. Note that parameters in the Paris lab differed from the parameters in Regensburg. Therefore two recipes are given in appendix A. Typical results are shown in figure (3.2).

3.2 Lithographical patterning

Electron beam lithography is a basic tool in state-of-the art nanofabrication. The principle is to locally expose a layer of resist with an electron beam. The standard resist is PMMA which consists of long, chain-like hydrocarbon molecules. The incident electron beam cuts the molecule chains in small pieces and hence the resist looses its stability in the exposed regions. The exposed regions can be washed out by

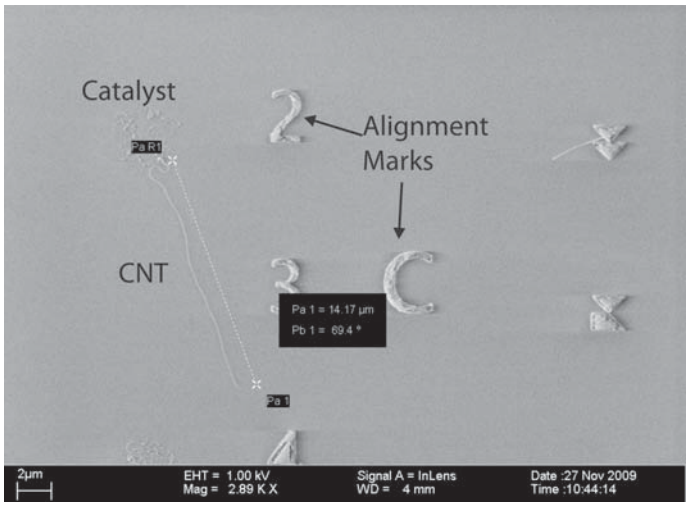

Figure 3.2: A typical Single-Walled Carbon nanotube as grown in our systems. It has a length of roughly $14\mu m$ *and grows from a catalyst spot. Catalyst spots are typically around* $1 - 2\mu m$ *in size.*

a developer (often MIBK). In this way microscopic structures down to about 20nm can be defined. The developed structures are then put into an evaporator (see next section). The whole surface is covered with a metal, for instance gold. Afterwards, in a process called lift-off, the resist is dissolved and the metal is washed away. Only at the exposed regions, where there is no PMMA in-between the metal and the wafer surface, the metal sticks to the wafer. In our sample fabrication process we carry out several electron beam lithography steps. We use it to deposit the catalyst before CVD growth and then to deposit alignment marks after CVD growth. In the last step of the fabrication process we use lithography again to put the contacts on the nanotube. In figure (3.3), a typical lithography is illustrated.

3.3 Evaporation

The evaporation of alignment marks is straight forward. We use a Ti/Au bilayer (5nm/50nm). The titanium is used as undercoating to increase the adhesive forces to the substrate. The more important and also more difficult part is the evaporation of the contacts. Here, two different methods have been tried out: The first method is a shadow-evaporation technique in which superconducting and normal leads are evaporated in the same evaporation step. The second technique is a two-step process, in which the normal leads are nanostructured in a first step and the aluminium

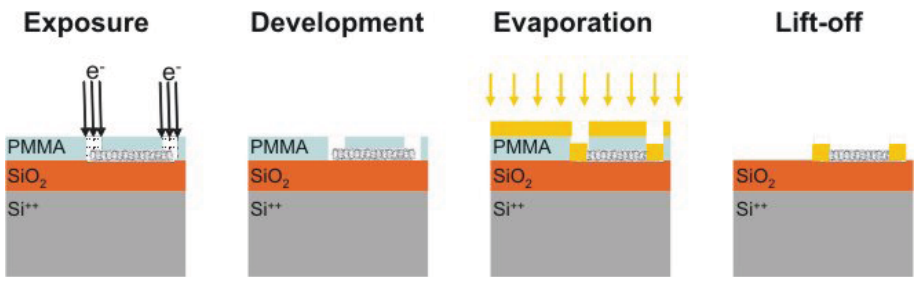

Figure 3.3: The four-step lithographical process which we use for nanofabricating our devices. As an example, the last lithography step is illustrated. In this step the Single-Walled Carbon Nanotube is contacted and connected to metallic leads.

contact in a second step. In both techniques, the aluminium contact is undercoated with 2,5 nm of palladium to increase the coupling between the nanotube and the metallic leads. When the Pd buffer layer was omitted, the tunnel barriers were too resistive. The width of the aluminum contact was around $80nm$ in order to be smaller than the superconducting coherence length ξ_S.

3.3.1 Shadow Evaporation

Shadow evaporation is a technique in which different materials can be deposited at different positions on a sample within the same pump-down. In our case the middle contact of our device has to be aluminium (with 2,5 nm Pd undercoating) whereas the normal leads are made out of palladium because of its excellent contact properties. Figure (3.4) illustrates how this process works. In figure (3.4(a)) our beamsplitter structure is shown. The sample is supposed to be lithographically structured and is sketched from plain view. In figure (b) the sample is put on a sample holder within a coating system. (Note that the 2,5 nm undercoating is not illustrated here. However it works similar as the aluminium coating.) In figure (b) we look at the sample from side view. In this cross section we cannot see the vertical lithography result as the borders are completely covered by PMMA. To see where this region is, it is highlighted by transparent colour. The sample is mounted such, that the 35° tilt of the sample is carried out in the direction of the superconducting finger. If one starts evaporating in this configuration, the material is deposited along the axis of the superconducting finger. Concerning the normal leads, however, their vertical orientation with respect to the evaporated material ensures that no material is deposited there. Therefore the tilt has to be big enough that the deposited material does not reach the base area of the normal leads but is blocked by the PMMA edges.

Therefore the technique is called shadow evaporation. For shadow evaporation it is important that the evaporated material beam has a specified direction. Electron-beam and thermal evaporation are techniques which meet this constraint.
In figure (3.4(c)) the sample is tilted back to zero angle. In this configuration we deposit Pd and thus create the normal leads. If we now perform the lift-off (3.4(d)), we obtain normal leads out of palladium and a superconducting aluminum lead in perpendicular direction.
The big advantage of shadow evaporation is that the superconducting contact is always perfectly aligned with respect to the normal leads. Also, a one step-process is in principle faster than carrying out two lithographical steps. Most measurements which we present in this work are carried out with a sample fabricated in this way. However the technique has also disadvantages. As material is deposited on the PMMA edges, lift-off is quite critical and the yield of working samples is low.
We used different evaporators at different sites. Surprisingly, the technique does not work, if UHV-evaporators are used. The reason is that the palladium is not only deposited at the normal leads but also on top of the aluminium. Although we already use 100nm of aluminium and 40nm of palladium, the superconducting gap of the aluminium can vanish entirely if the palladium contains a small amount of magnetic impurities. At higher evaporation pressures, enough oxygen is in the chamber to build up a small Al_2O_3 layer which shields the palladium. In this case the aluminium contact remains superconducting but shows a reduced gap [113].

3.3.2 Two-step Process

If either the lift off does not work properly or the gap is not visible any more in the transport spectroscopy, a two-step lithography and evaporation process is the method of choice. In a first lithography step, the normal contacts and leads are structured and evaporated. In a second step the aluminium contact connecting the nanotube with the respective lead is lithographically defined and evaporated with the Pd-undercoated aluminium. The problem of this process is to realign the second lithography in-between the normal leads with an error less than 100nm. This is very demanding and often fails.

3.4 Measurement setup

We need two ingredients to carry out our measurements. The first is an electronic measurement environment, which is sensitive enough to detect several pA. The second is a dilution cryostat which cools the sample to 80mK. The low temperatures are necessary for several reasons: The sample has to be cooled below T_C of aluminium

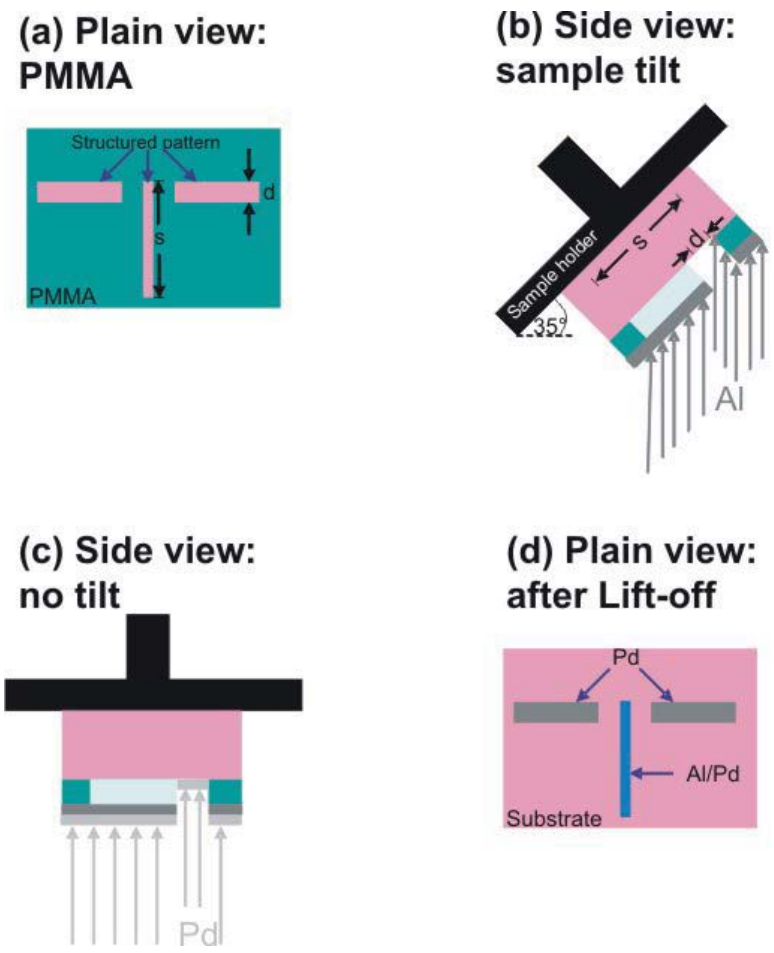

Figure 3.4: Simplified figure to illustrate our shadow evaporation technique: (a) Both normal and superconducting leads are patterned in the same lithography step.(b) Then the sample is put in the evaporator. First, aluminium (with a small Pd undercoating, as described in the text) is deposited at an angle of 35-40 degrees . The material is evaporated along the superconducting finger. Because of the tilting, no material is deposited at the normal leads. (c) In the second evaporation step , Pd is evaporated at zero angle. (d) After the lift off, the superconducting contact is made out of aluminium (with Pd on top) and the normal leads consist of pure palladium.

which is around 1,2K. Furthermore the low temperatures are necessary to observe Coulomb blockade, as explained in section 2.2. Last but not least thermal noise has to be excluded to perform sensitive measurements.

3.4.1 Electronics

The electronic setup is depicted in figure (3.5). Two biasing schemes are used. In the so-called middle-injection, denoted by V_M and red coloured lines, a bias voltage is applied at the superconducting contact. Current is sent into the nanotube and splits into a left (I_L) and a right (I_R) component. Both branches are grounded by $2k\Omega$ resistors. I_L and I_R are converted to voltages, amplified by low-noise amplifiers of type SA-220F5 and detected with standard Lock-In technique. The second injection possibility is called side-injection (V_S) and is highlighted by green lines in the circuit diagram. Here, we inject at one of the normal leads and measure the transmission at the other normal lead, in the same way as described above. The measurement of the current going to the superconducting lead is not possible within our circuit. The reason is that the superconducting lead is designed as injection line with a $200k\Omega$ resistor mounted in series. This resistance together with a grounded $2k\Omega$ resistor is used to divide the injected voltage on chip at base temperature. Hence thermal noise injected into the system is low. Additionally we use standard RC-filters for the gates and special microcoax cables for the measurement lines in order filter out parasite signals coming from the outside world.
The side-injection setup gives us the possibility to operate our device as a standard double quantum dot. It is used to find a regular honeycomb stability diagram. Here, the small current going to the superconductor, mediated by Andreev Reflection, is neglected.
We use voltage amplifiers instead of I-V converters because our electronic environment is designed for future noise measurements. Therefore the sample is not mounted on a standard chip carrier but on a PCB. Furthermore we minimize capacitances to ground and install high-frequency suitable measurement lines at the normal contacts. The goal is to carry out shot noise cross-correlation measurements in the MHz-regime between the two normal leads in a future experiment. The measurements are supposed to be taken at frequencies between $100kHz$ and $5MHz$ in order to avoid $1/f$-noise. A picture of the PCB is available in appendix B.

3.4.2 Cryogenics

We use a home made dilution-fridge from Patrick Pari at CEA Saclay, with a base temperature of 30mK. Due to unknown reasons (probably a slightly detuned mixture) we reach a base temperature of 80mK. For our purpose, however, this is low enough. The cooling process is mediated by a phase transition between He3 and He4 in the mixing chamber of the device which is thermally coupled to our sample. Measurements show that we reach an electronic temperature of about 100 mK in

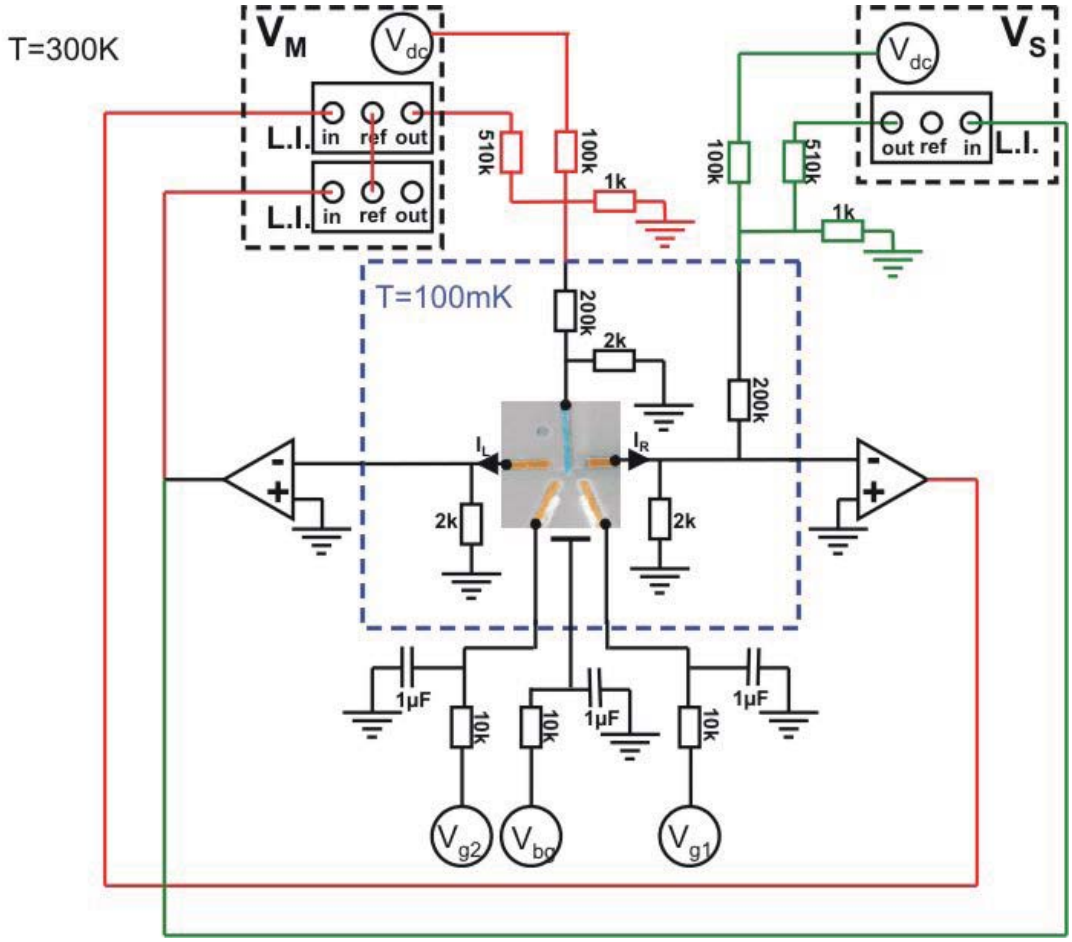

Figure 3.5: Our two different injection schemes are illustrated in this figure. We either inject at one of the side normal contacts (V_S) or at the superconducting contact in the middle (V_M). In both cases we apply a voltage which induces a current through the nanotube. The current is changed into voltage by the two grounded resistors mounted adjacent to the normal leads. We then amplify the voltage and measure it with standard Lock-In technique.

this way. In the context of this work, the operating principle of a dilution-fridge will not be discussed in detail. The reader is referred to the corresponding literature [114], [115].

Chapter 4

Transport in a double quantum dot connected to a superconducting lead

The data presented in this chapter was obtained almost entirely from one particularly successful sample named S3LC4. The sample was cooled down three times. When data from other samples is presented, this is indicated in the text.
In this chapter we present the results of our experiment. We quickly summarize the point of departure which was explained in previous chapters. Our goal is to split a Cooper pair injected by a superconducting electrode into a normal metal fork. In order to favor the splitting process we design the normal metal fork such that it acts as a double quantum dot. Furthermore the normal metal fork must be combinable with superconductors. All the requirements are met by Single-Walled Carbon Nanotubes. Hence we design the carbon nanotube beamsplitter, as depicted in figure (4.1).
Within this chapter, we will answer three questions. The last and most important one is if we can split a Cooper pair with the suggested setup. In order to get to this final point we have to do two preliminary checks in the next section: First we have to show that our sample acts as a double quantum dot and second we must ensure that we inject Cooper pairs into our system.

4.1 Spectroscopy of the double dot

We measure the differential conductance in two measurement setups labeled side-injection and middle-injection, respectively (see figures (3.5) and (4.2)). The measurements are carried out at $T = 80mK$ and an ac-excitation voltage of $V_{ac} = 1.8\mu V$.

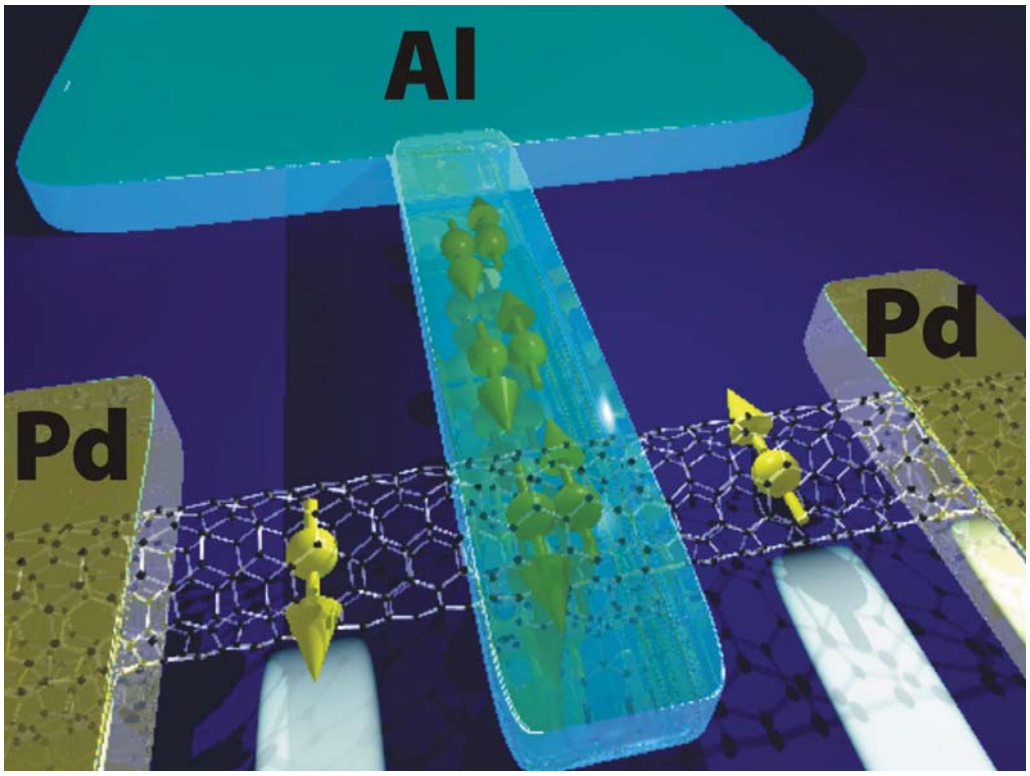

Figure 4.1: The Carbon Nanotube beamsplitter: A Single-Walled Carbon Nanotube is connected to two normal metal leads (Pd or Ti/Au) and a third, superconducting electrode in the middle (Al). The nanotube parts in-between two contacts act as a quantum dot. Hence the whole system is a double quantum dot attached to a superconducting reservoir.

In order to characterize our sample as a double dot we use the side-injection setup. Later on we switch to middle-injection to show the injection of Cooper pairs.

4.1.1 Stability diagram of the sample

We use the side-injection setup to measure the stability diagram because in this way, we can find the points where both dots are at resonance within one measurement. In the middle-injection setup we would have to carry out two measurements simultaneously to get the same information. Further technical details are given in appendix (C). The result is depicted in figure (4.3) at a constant backgate voltage of $V_{bg} = -2,543V$.
The honeycombs are regularly spaced. Moreover the sample is in the tunnel cou-

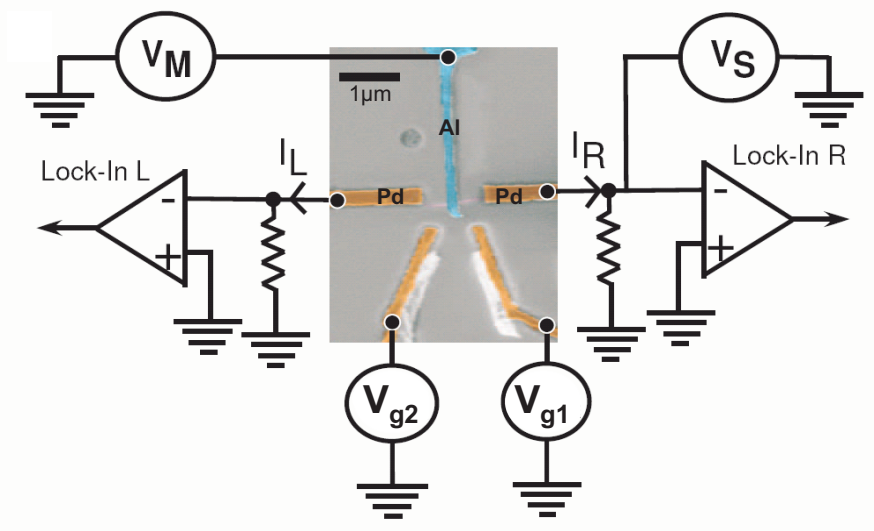

Figure 4.2: In this figure, our two different injection schemes are illustrated. We either inject at one of the side normal contacts (V_S) or at the superconducting contact in the middle (V_M). We use side-injection to characterize our sample as a double quantum dot. In the middle-injection setup we show the injection and splitting of Cooper pairs.

pling regime, where the excess electrons delocalize over the double dot and form a molecular state (see subsection 2.3.2). The yellow number insets in figure (4.3) define the fixed number of electrons on left and right dot, respectively.
In this context we assume that the superconducting contact which is in the middle of our nanotube creates a potential barrier between the two dots by mechanical deformation. The difference in comparison with previous devices (see figure (2.14)) is that the contact splitting the nanotube into two dots has always been an electrostatically coupled gate [22], and not a tunnel coupled contact. For further details see subsection 3.4.1. Despite the fact that we inject within the superconducting gap, we have a small leakage current mediated by Andreev Reflection going to the superconductor. We assume that Andreev Reflection makes a smaller contribution to the current than highly transmissive tunnel barriers at the normal contacts. Hence this leakage current is assumed to be unimportant for the electrostatic coupling pa-

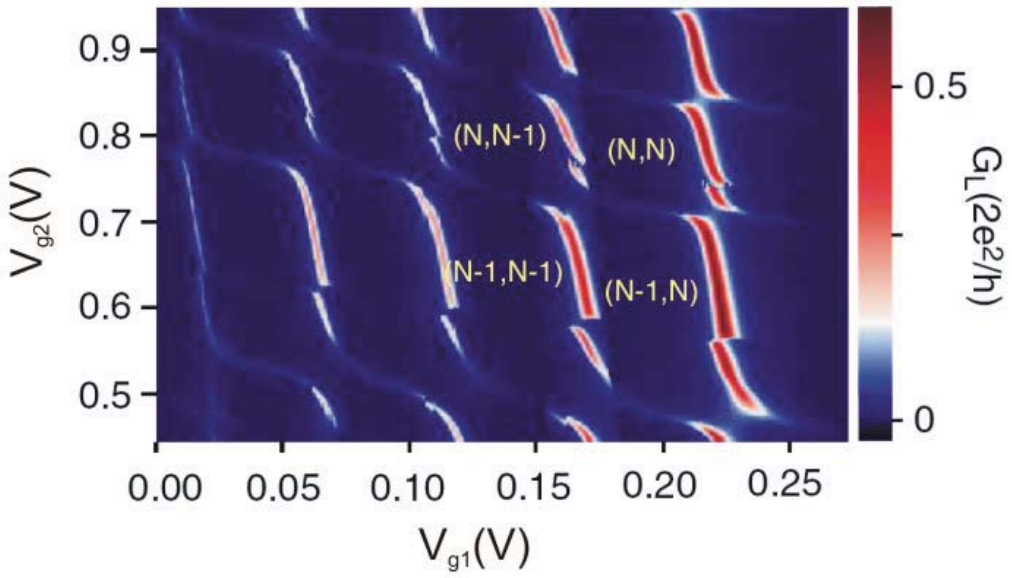

Figure 4.3: Typical stability diagram of our samples. The yellow number insets define the number of electrons on 1st and 2nd dot, respectively.

rameters of the whole system.
Next we give experimental evidence that the current to the superconducting lead is low:
First, we use an argument based on current conservation. The situation is explained in figure (4.4(a)).
The total injected current I_{tot} splits into three different current branches:

$$I_{tot} = I_1 + I_2 + I_3 \tag{4.1}$$

The current flowing to the superconductor is hence

$$I_2 = I_{tot} - I_1 - I_3 = \frac{U_{ac}}{R_{tot}} - I_1 - I_3 \tag{4.2}$$

and can be compared to the current I_3 going to the second normal contact. Our point is that $I_2 < I_3$ and can be neglected. From figure (4.4(b)), we can calculate R_{tot}:

$$R_{tot} = \frac{1}{\frac{1}{2k\Omega} + \frac{1}{R_{RS}+2k\Omega} + \frac{1}{R_{LS}+2k\Omega}} \tag{4.3}$$

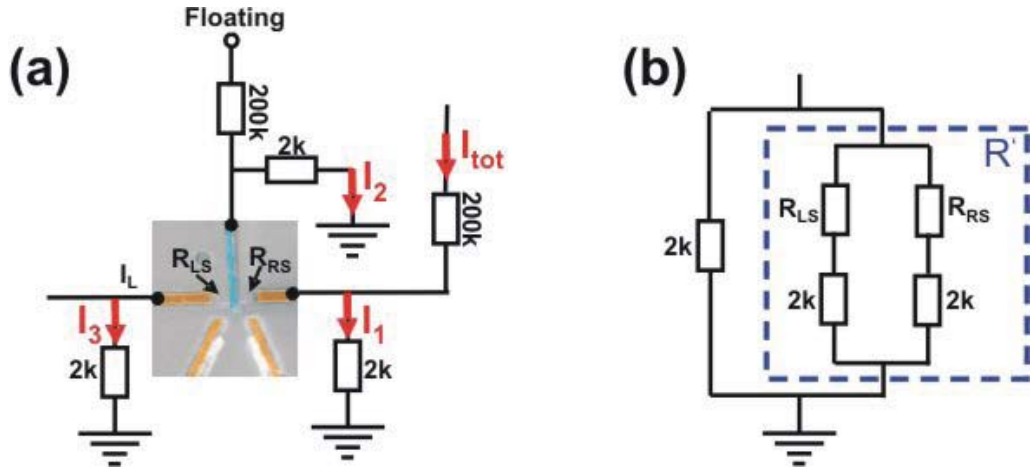

Figure 4.4: (a) In the side-injection setup, the total injected current splits into three branches. (b) Equivalent circuit scheme of the side-injection setup.

The values for the resistances R_{LS} and R_{RS} which connect left and right normal contact to the superconducting contact can be measured within the middle-injection setup. We simply measure the conductances $G_{L,R}$ to left and right normal lead. Hence the current going to the superconductor is given by:

$$I_2 = U_{ac}[\frac{1}{2k\Omega} + \frac{1}{1/G_R + 2k\Omega} + \frac{1}{1/G_L + 2k\Omega}] - I_1 - I_3 \tag{4.4}$$

If we carry out the above analysis at the triple points, we find that the current going to the second normal lead is indeed higher than the current going to the superconductor. In appendix D we illustrate an example where we obtain a factor 2,4 between the two current branches. The analysis is not very precise, however, as the error made to determine the total current is big.
Second, the behavior $I_2 < I_3$ can also be seen directly in figure (4.5). In the middle-injection setup (4.5(a)) we use $V_M = 50\mu V$ well within the gap. Clearly, the conductance between superconducting lead and the left normal lead (the right normal contact which is not shown is even less transmissive) is a factor 10 smaller than the conductance measured across the whole dot in the side-injection setup (4.5(b)). This result is not consistent with the factor 2,4 obtained before. The reason for this is the big error which we have to consider when calculating I_2 in equation 4.4. In our example, the current going to left and right lead in the middle-injection setup is around $1pA$. The current I_1 measured in the side-injection setup is $(830 \pm 0,7)pA$. That means that the currents referring to $G_{L,R}$ are on the same order of magnitude

as the error bar of I_1. Nevertheless we use $G_{L,R}$ to calculate the total current from which we subtract I_1 and I_3. Hence the determination of the total current is not exact and the factor 2,4 obtained in this way as a ratio between I_2 and I_3 is less reliable than the factor 10 which we obtain from the direct comparison of the stability diagrams of middle-injection and side-injection. That means that we henceforth rely on the second observation to claim that in the side-injection setup, the current going to the superconducting terminal is smaller than the current going to the the second normal terminal.
This observation gives evidence for the assumption that the superconducting terminal connected to ground does not change the coupling parameters in comparison with double dots which are split by a central gate electrode.
Further support for this claim is given by the observation of the line shapes of the stability diagrams of middle- and side-injection. The shapes of the honeycombs compared within figure (4.5) are equivalent. In the middle-injection case, the pattern is slightly shifted down and left with respect to the side gate voltages. This happens regularly from one measurement to the next but has no importance as long as the dimensions of the honeycombs do not change. It thus turns out that the location of electron injection is not relevant for our determination of electrostatic and tunnel coupling of the two dots.

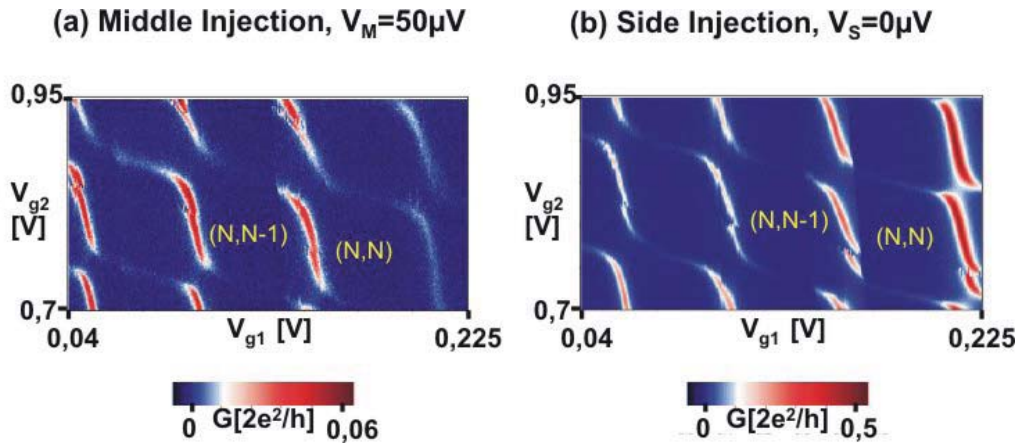

Figure 4.5: This figure shows the equivalence of the line shapes within the stability diagram in middle- and in side-injection. In (a), the middle-injection pattern is depicted. In comparison to the side-injection pattern (b), it is shifted a little bit down and to the left. Otherwise it is completely equivalent.

4.1.2 Extraction of electrostatic parameters

From the stability diagram, we can extract the coupling parameters of the double quantum dot. For this purpose one typical honeycomb cell of the stability diagram is considered (see figure 4.6(a)).

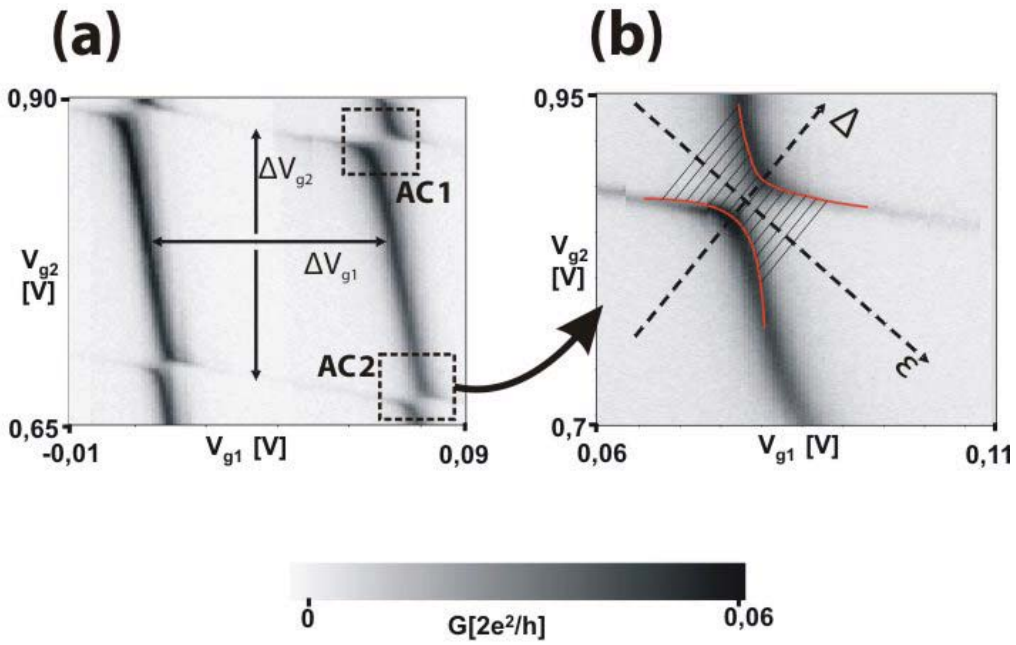

Figure 4.6: (a) The dimensions of the honeycomb cells define the gate capacitances. Furthermore the charging energy can be extracted. (b) The separation of the two anticrossing lines along the axis of detuning ϵ gives insight in both electrostatic and tunnel coupling.

The following analysis is based on references [22] and [86]. First, the coupling capacitances of the two sidegates to left and right dot are derived from the dimensions $(\Delta V_{g1}, \Delta V_{g2})$ of the (regular spaced) honeycomb cells:

$$C_{g1} = \frac{\mid e \mid}{\Delta V_{g1}} = \frac{\mid e \mid}{0,068V} = 2,35aF \tag{4.5}$$

$$C_{g2} = \frac{\mid e \mid}{\Delta V_{g2}} = \frac{\mid e \mid}{0,2V} = 0,8aF \tag{4.6}$$

Second, the charging energies E_{C1}, E_{C2} of left and right dot are calculated. To do so, the total capacitances of left and right dot $C_{\Sigma 2}, C_{\Sigma 1}$ are extracted from the finite

bias stability diagram presented in figure (4.7). The finite bias dependence of the stability diagram is explained in figure (2.8). The analysis follows reference [22].

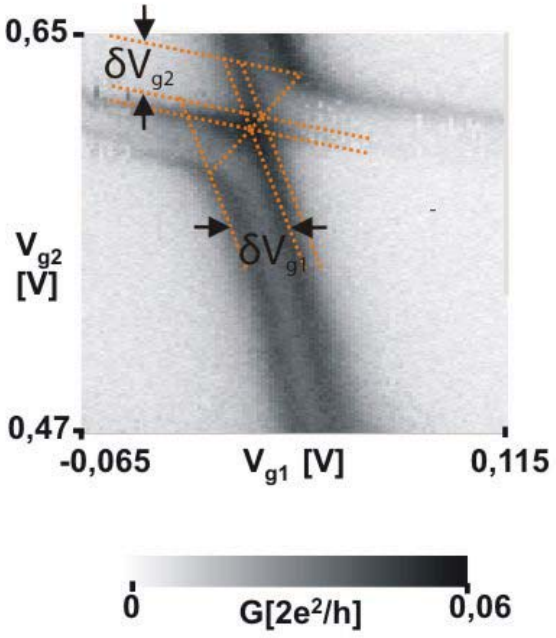

Figure 4.7: The anticrossing presented in figure 4.6(b) at $V_{bias} = 200\mu V$. The parameters δV_{g1} and δV_{g2} allow to calculate the charging energy of 1st and 2nd dot.

To calculate $C_{\Sigma 2}, C_{\Sigma 1}$, the equations 2.17 and 2.18 are used:

$$\frac{C_{g1,2}}{C_{\Sigma 1,\Sigma 2}} = \frac{\mid V_{sd} \mid}{\delta V_{g1,2}}$$

With $\delta V_{g1} = 0,012V$ and $\delta V_{g2} = 0,085V$ extracted from figure (4.7), $V_{sd} = 200\mu V$, $C_{g1} = 2,35aF$ and $C_{g2} = 0,8aF$, we obtain the following total capacitances for the two dots:

$$C_{\Sigma 1} = 141aF \tag{4.7}$$

$$C_{\Sigma 2} = 340aF \tag{4.8}$$

Using equation 2.10, we obtain for the charging energy for the two dots:

$$E_{C1} = \frac{e^2}{C_{\Sigma 1}} = 1,1meV \tag{4.9}$$

$$E_{C2} = \frac{e^2}{C_{\Sigma 2}} = 0,5meV \tag{4.10}$$

The stability diagram (4.6(a)) is presented in the voltage scale. In order to transfer the data from the gate voltage to the energy scale we need the conversion factors α_{g1} and α_{g2} as given in equations 2.15 and 2.16. However, we do not use the capacitance ratios as given by the two equations but use a further method to extract the conversion factors directly. For this method, it is necessary to measure the stability diagram at several finite bias values and compare the observed line splittings δ_1, δ_2 far away from the triple points with the corresponding gate voltage differences. Additionally to the measurement at zero bias, we measure the stability diagram at a bias voltage $V_{sd} = 200\mu V$ and at $V_{sd} = 400\mu V$. The three measurements are illustrated in figure (4.8).

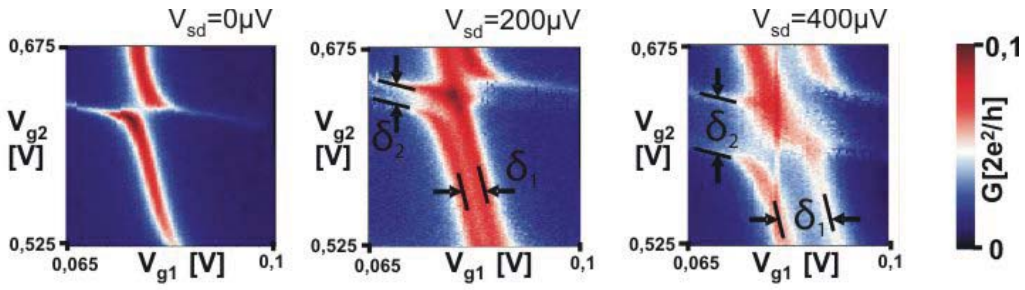

Figure 4.8: Stability diagram of the same anticrossing at B=90mT at three different bias voltages. The line splitting increases as a function of the bias voltage.

To understand the splitting, we have to consider figure (4.9). We are interested in the splitting far away from the triple points. In figure (4.9(a)) we illustrate an energy diagram in this situation. As the detuning ϵ is large, the individual dot energy levels $E_{1,2}$ do not form a molecular state any more. If we fix the sidegate voltage V_{g2} of the second quantum dot and sweep only V_{g1}, we can switch to a single quantum dot picture. The second quantum dot is traversed by means of cotunneling. In a more simplified picture it can even be thought of being part of the drain reservoir. In figure (4.9(b)) we plot the corresponding differential conductance as a function of source-drain bias V_{sd} and V_{g1}. We obtain Coulomb-diamonds of zero conductance (black regions) and regions of finite conductance (white regions). This plot is typical for a single quantum dot and illustrated in figure (2.5). If we go to a fixed and finite bias voltage in figure (4.9(b)) and sweep along the orange arrow, we obtain a finite conductance region of width δ_1, depending on the bias voltage. Thereby it

is possible, that the transitions from Coulomb diamonds to the conductive region are very pronounced. If this is the case the conductance along the orange arrow is a double peak structure. In figure (4.8) the line cuts along constant V_{sg2} which determine δ_1 correspond to the orange arrow in figure (4.9(b)). For fixed V_{sd} and V_{g2} we sweep V_{g1} and henceforth obtain a region of finite conductance of width δ_1. This width increases with increasing bias voltage. Referring back to figure (4.9(a)) we find that conductance is possible as long as E_1 is in-between the chemical potentials $\mu_{L(R)}$ of left and right lead. This interval is given exactly by eV_{sd}. From the plots given in figure (4.8) we can extract the gate voltage interval δ_1 which is necessary to overcome the energy difference given by eV_{sd}. Hence we can calculate the conversion factor α_{g1} which converts gate voltage in absolute energy. In the same way we can find α_{g2}.

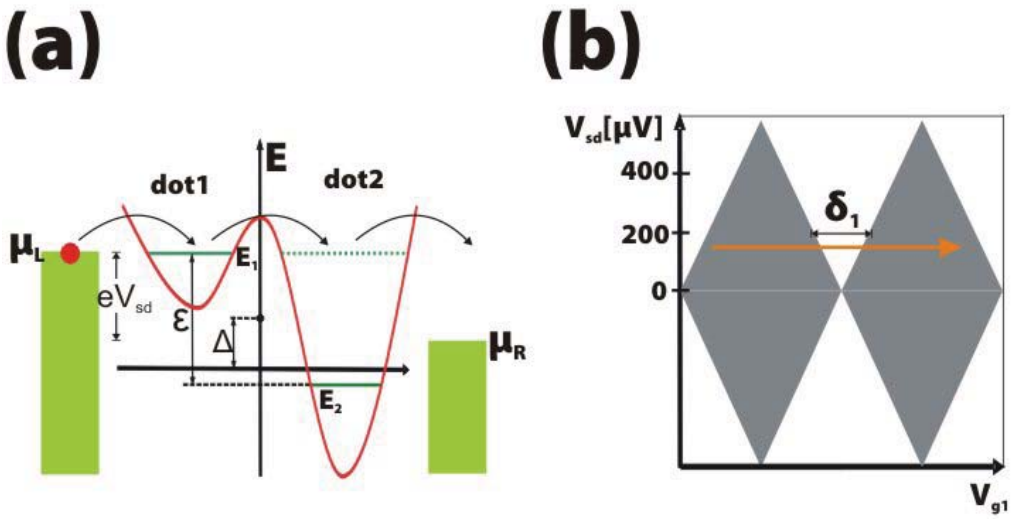

Figure 4.9: (a) If the detuning of E_1 and E_2 becomes big, no molecular state develops. That means that the double quantum dot behaves like a single quantum dot far away from the triple points. The second dot is traversed by co-tunneling. (b)We obtain Coulomb-diamonds as a function of applied V_{sd} and V_{g1}. The second quantum dot can be interpreted as part of the right contact.

Due to this method the two conversion factors are given by

$$\alpha_{g1} = \frac{V_{sd}}{\delta_1} \tag{4.11}$$

and

$$\alpha_{g2} = \frac{V_{sd}}{\delta_2} \tag{4.12}$$

Note that the measurements are carried out at $B = 90mT$. The sample is thus in the normal state and the measurement signal is much higher. This is possible as tunnel coupling and electrostatic coupling between the normal leads are supposed to be equal in superconducting and normal state. The stability diagrams in figure (4.8) are measured in the middle injection configuration at three different bias voltages. We measure at $V_{sd} = 0\mu V$, $V_{sd} = 200\mu V$, $V_{sd} = 400\mu V$. We carry out two finite bias measurements to have two independent measurements of the conversion factors α_{g1} and α_{g2}. The results are illustrated in figure (4.10(a)) and (4.10(b)). There, we plot the line splitting $\delta_{1,2}$ as a function of the applied bias voltage V_{sd}. The splitting of the lines is a linear function of the bias voltage. To minimize the error, we carry out a linear fit of our three data points and obtain the conversion factors α_{g1} and α_{g2}.

$$\alpha_{g1} = 0,03987 \tag{4.13}$$

$$\alpha_{g2} = 0,00973 \tag{4.14}$$

These conversion factors can be used to convert the gate voltage axes (V_{g1}, V_{g2}) of the stability diagrams to the absolute energy axes eV_1 and eV_2.

$$eV_1 = e\alpha_{g1}V_{sg1} = 0,03987eV_{sg1} \tag{4.15}$$

$$eV_2 = e\alpha_{g2}V_{sg2} = 0,00973eV_{sg2} \tag{4.16}$$

Next we focus on one particular anticrossing within figure (4.6(a)) which is highlighted by the small dashed box in the down right corner. A zoom on this region is available in figure (4.6(b)). The coordinate system (V_{sg1}, V_{sg2}) is converted to absolute energy (eV_1, eV_2) using the conversion factors α_{g1} and α_{g2}. Furthermore we change variables in the following way:

$$\Delta = eV_1 + eV_2 \tag{4.17}$$

$$\epsilon = eV_1 - eV_2 \tag{4.18}$$

The new coordinate system Δ, ϵ is defined exactly as in the explanation given in figure (2.11). In this way we can understand that ϵ is the axis of detuning and Δ is the axis which shifts the whole double-dot potential with respect to the chemical potential of the leads.

If one plots the energy difference E_Δ along the Δ-axis between the anticrossing lines as a function of the detuning ϵ, one obtains the plot illustrated in figure (4.10(c)). As pointed out in equation 2.24, the separation of the wings, (again neglecting the grounded superconducting reservoir), is given by:

$$E_\Delta = \sqrt{2}U' + \sqrt{4\epsilon^2 + 8t^2}$$

When we extract the separation of the anticrossing lines in figure (4.6(b)), we face the problem that the lines have finite width. In order to account for the error which we make by extracting the separation of the two anticrossing lines, we carry out the analysis for an upper boundary of maximal line separation (indicated by the upper dots in figure (4.10c)) and a lower boundary of minimal line separation (indicated by the lower dots in figure (4.10c)). Next we fit each dataset with equation 2.24. As a result we take the mean value of the two fits. The result for the electrostatic coupling is $U' = (4 \pm 2)\mu eV$ and for the tunnel coupling we obtain $t = (126 \pm 9)\mu eV$. Thus the tunnel coupling dominates over the electrostatic coupling in our device.

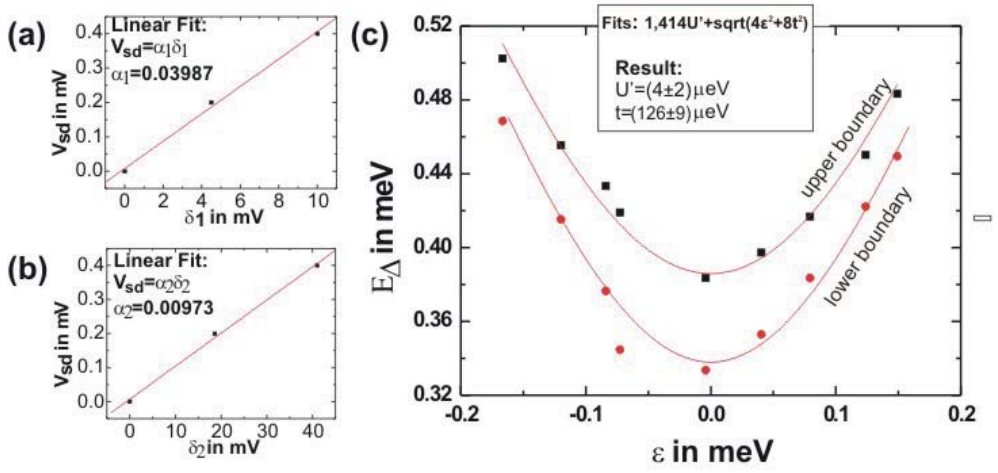

Figure 4.10: (a),(b) The line splitting as a function of bias voltage defines the conversion factors of the two gate voltages to the absolute energy scale. (c) The separation of the two anticrossing lines allows the determination of both tunnel and electrostatic coupling between the two dots of the double dot device.

At this point we consider the first question, namely the question whether our device acts as a double dot, as answered. We clearly observe double dot behavior

and furthermore are able to extract all relevant coupling parameters which will be important for modeling our system theoretically.

4.1.3 Testing the NS-junction

Now we consider the second check mentioned in the beginning of this chapter: We have to show that we inject Cooper pairs into our double dot. At base temperature, we test whether the aluminum contact is superconducting. To do so we adjust the two sidegate voltages such that (V_{g1}, V_{g2}) are located within a honeycomb, away from the resonances. In the middle injection setup, we henceforth probe the BCS-density of states (equation 2.32) as a function of the applied source-drain voltage. The equation is used to fit the obtained data at zero magnetic field (marked as black dots in figure 4.11(left)). From the fit, an electron temperature of $T = 100mK$ and a superconducting gap of $\Delta_S = 85\mu eV$ can be extracted. If a magnetic field (B=44,5mT) is applied, the gap vanishes and the sample switches to its normal state. The corresponding data is denoted by green dots within figure (4.11(left)).

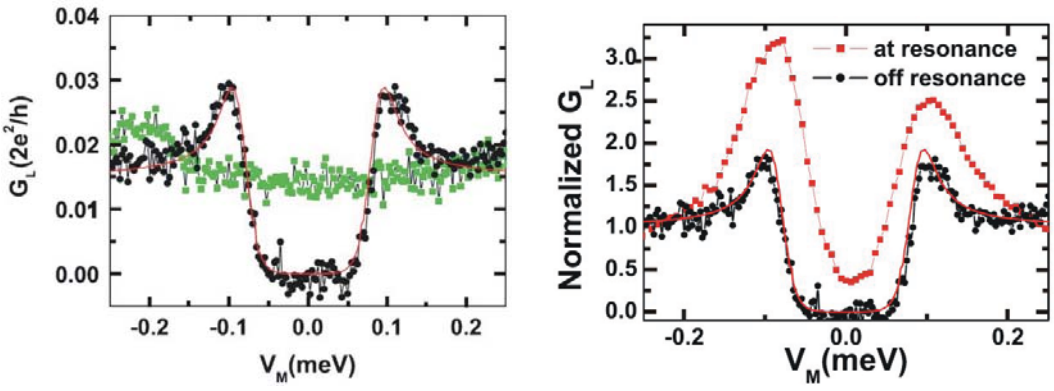

Figure 4.11: (Left) In the middle-injection scheme we measure the differential conductance at T=80mK between the superconducting contact and one of the normal leads. Away from resonance, in the Coulomb blockade regime, we observe the superconducting gap (black dots) at zero magnetic field. Fitting the data with the BCS-density of states, an electron temperature of T=100mK and a gap of $\Delta_S = 85\mu eV$ is extracted. If a magnetic field is applied (44,5mT), the sample switches to the normal state and the gap vanishes.(Right) The measured conductance between middle and left electrode at one of the triple points. Finite subgap current, which can be attributed to Andreev Reflection, is observed.

In figure (4.11 (right)), the bias dependence of the NS junction is shown at one of the triple points. To compare the measurement to the off-resonance case, the data

is normalized to the off-resonance data. Clearly we observe finite subgap current which can be attributed to Andreev Reflection.

4.2 Evidence for splitting Cooper pairs

In section (2.6) we introduced the conductance asymmetries α_S, α_N as a diagnostic tool to detect the existence of CAR in our beamsplitter sample. In the following section, this tool is applied to our measurement results.

4.2.1 Measurements along the axis of detuning at zero and finite magnetic field

According to the strategy explained in section 2.6, we carry out conductance measurements in the middle-injection setup. We measure the differential conductance at left and right lead at zero and finite magnetic field. The measurements are carried out at triple points and single resonances.
We zoom into the honeycomb stability diagram shown in figure (4.3) and focus on individual honeycombs as shown in figure (4.12). If we measure along the yellow arrow we obtain the differential conductance at two adjacent triple points which are labeled T_1 and T_2. The same measurement is carried out along the green arrow to obtain the differential conductance at the single resonances. The single resonance in figure (4.12) is labeled S_1. In total, 36 triple points and 11 single resonances were studied.
First we discuss the measurements at the triple points. The sweep-direction as well as starting and end-point of the sweep are indicated by the yellow arrow in figure (4.12). The sweep direction is a superposition of gate voltages V_{g1} and V_{g2}. Using equations 2.15, 2.16 and 4.9, 4.10, we can define the sweep direction as the energy axis $\delta\epsilon$

$$\delta\epsilon \approx (C_{g2}E_{C2}\delta' V_{g2} + C_{g1}E_{C1}\delta' V_{g1})/e \tag{4.19}$$

where C_{g2}, C_{g1} are the gate capacitances of the sidegates, E_{C2}, E_{C1} are the charging energies of the dots and $\delta' V_{g1}, \delta' V_{g2}$ are the voltage differences at the sidgates which are the parameters to drive the measurement along the yellow arrow in figure (4.12). In figure (4.13) the obtained results for two anticrossings labeled $AC1$ and $AC2$, i.e. 4 triple points, are presented. The two anticrossings are marked within the stability diagram presented in figure (4.6). The two triple points within each anticrossing correspond to the two visible peaks. As described above, the measurement is taken at both left and right lead, therefore each diagram is two-fold. G_L signifies the

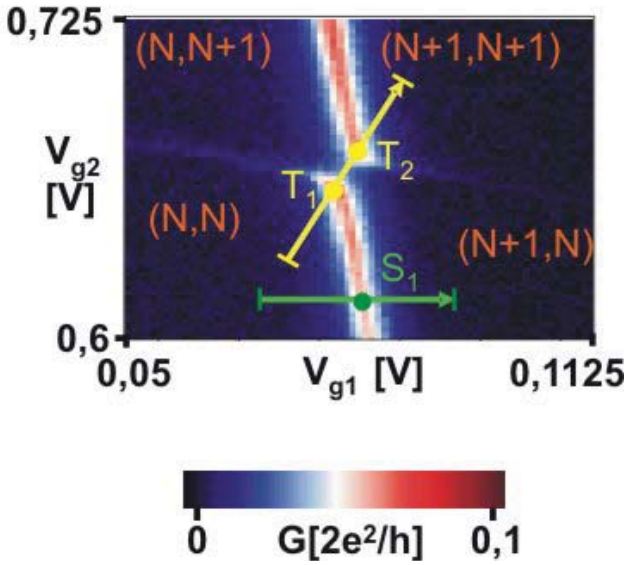

Figure 4.12: Stability diagram of a typical anticrossing in the middle-injection setup. The yellow arrow defines the scanning direction across two adjacent triple points T_1 and T_2. We measure the zero bias conductance at left and right lead simultaneously, following the indicated direction. The same is carried out for the single resonance S_1.

conductance at the left normal lead whereas G_R is standing for the conductance at the right normal lead. The red curves are the measurements in the superconducting state whereas the black curves are the corresponding measurements in the normal state. Note that the black curves are scaled down to allow better comparison with the subgap current. From the plots it is also evident, that the coupling to the left reservoir is better than the coupling to the right reservoir. Therefore G_L is higher than G_R. The most important feature of figure (4.13) is the conductance ratio between the peak values of left and right lead in the superconducting case (α_S) and in the normal case (α_N). From figure (4.13), the extracted conductance ratios are equal in normal and superconducting state. We analyze this feature in more detail by determining α_S and α_N for 36 triple points.

Second we repeat the analysis for single resonances. As opposed to equation 4.19, we choose horizontal scanning directions in the middle of the honeycomb cells. The energy interval $\delta\epsilon$ along the sweep direction is sketched in figure (4.12) and is defined

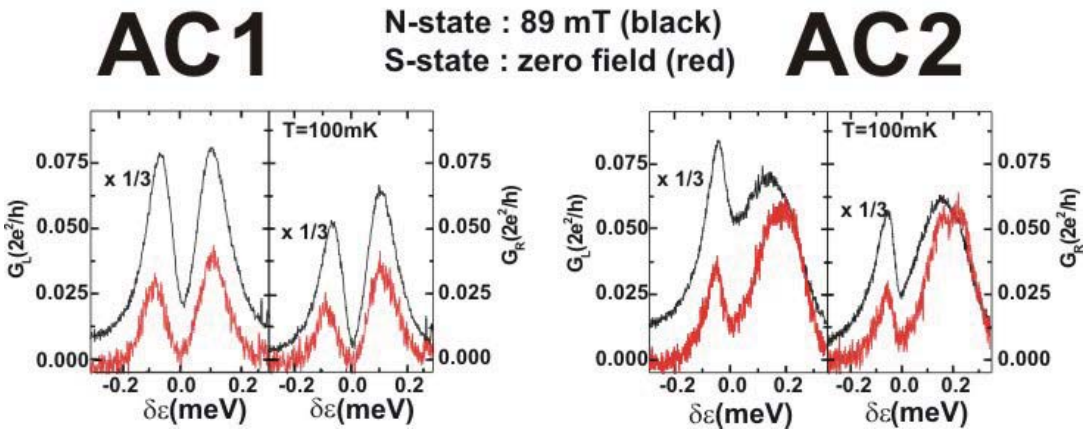

Figure 4.13: We measure the zero bias conductance across the anticrossings, as shown in figure (4.12) in the middle-injection setup. Data for two different anticrossings is shown. Each anticrossing shows a double peak corresponding to two adjacent triple points. The measurement is carried out in the superconducting state (red line) and the normal state (black line). Note that the black lines represent the data multiplied by a factor 1/3. Most importantly, the conductance ratio between left and right lead seems to be equivalent in normal and superconducting state.

as

$$\delta\epsilon \approx (C_{g1} E_{C1} \delta' V_{g1})/e \tag{4.20}$$

where C_{g1} is the gate capacitance of the first sidegate, E_{C1} is the charging energy of the first dot and $\delta' V_{g1}$ is the voltage difference at the first sidgate which drives the measurement along the orange arrow in figure (4.12). The equivalent plot to figure (4.13) is given in figure (4.14). Along the defined sweep direction only one dot, namely quantum dot 2 attached to G_L, is at resonance. The second dot which is attached to G_R is in Coulomb blockade. Therefore we obtain hardly any signal there. In the normal state, however, G_R is not zero though. The reason is that cotunneling makes a small contribution to transport and results in a finite conductance. In the superconducting state, this contribution is suppressed. In figure (4.14) we analyze again the conductance ratio between left and right lead in the superconducting case (α_S) and in the normal case (α_N). From the figure it is visible that the conductance ratios depend on the fact whether the sample is in normal or superconducting state. The ratios are different in the two cases. In the superconducting state the current at the right lead gets so low, that it falls into the noise of our measurement. In this situation we simply take the value to be zero and add an error bar corresponding to

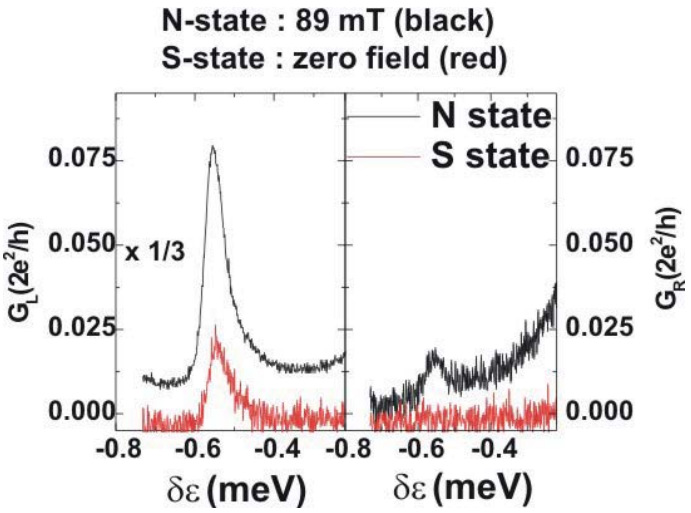

Figure 4.14: We measure the zero bias conductance across the single resonances, as shown in figure 4.12. Data for one typical single resonance is shown. The normal state is represented by the black line (scaled down in the figure) whereas the data in the superconduting state is given by the red line. Most importantly, the conductance ratio between left and right lead changes if we switch from the normal to the superconducting state.

the noise level of our measurement.
All in all, we determine α_S and α_N for 11 single resonances.

As a final step we draw all points α_S as a function of α_N into a common diagram (see figure (4.15)).
Consistent with equations 2.42 and 2.40, $\alpha_S[\alpha_N]$ for single resonances fall onto a parabolic function whereas $\alpha_S[\alpha_N]$ for triple points fall on a linear function. This agrees with our qualitative reasoning in subsection (2.6.1) based on the presence and absence of CAR. The data corresponding to the triple points falls on $\alpha_S = \alpha_N$ and thus demonstrates that CAR is present in our device.
This result means that we can indeed split Cooper pairs incident from a central superconducting finger into two normal metal leads. To do so, we sweep V_{g1} and V_{g2} such that we inject Cooper pairs at the triple points of the stability diagram. We can furthermore switch CAR off if we move the gates away from the triple points and readjust them to measure in the middle of the vertical conductance lines, in-between the triple points. We call these points single resonances. At these points, only local Andreev Reflection contributes to the total transport.

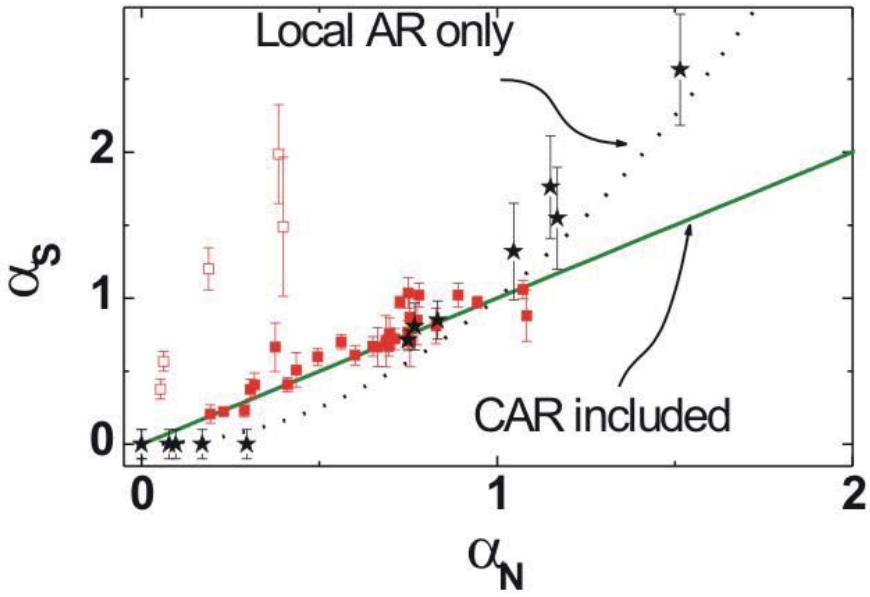

Figure 4.15: We plot α_S as a function of α_N for both triple points and single resonances. As expected, single resonances fall on a parabola whereas triple points fall on a linear function. This proves the existence of CAR in our beamsplitter device.

4.2.2 Unbalanced Anticrossings

For 5 out of 36 anticrossings, a special situation arises. As can be seen in figure (4.15), the red open squares do not fall on the universal linear function $\alpha_S[\alpha_N]$.
A typical measurement across an anticrossing of this kind is presented in figure (4.16(a)). We call this anticrossing unbalanced because the doublets both at right and left side differ substantially in their height. Furthermore the peaks are narrower than usually. These effects can be attributed to shifting gate potentials at the triple points in question. Rather than sweeping across the triple points, we accidently sweep on a shifted axis which is shown by the yellow arrow within figure (4.16(c)). In comparison with the original sweep direction (indicated by the dashed arrow) the sweep is shifted on the axis of detuning. By comparing the data to the stability diagrams of the anticrossings in question, Alfredo Levy-Yeyati can quantify this shift and take it into account within his full theory. In this way he can theoretically reproduce our data (compare figure 4.16(b)). This reasoning justifies that we treat

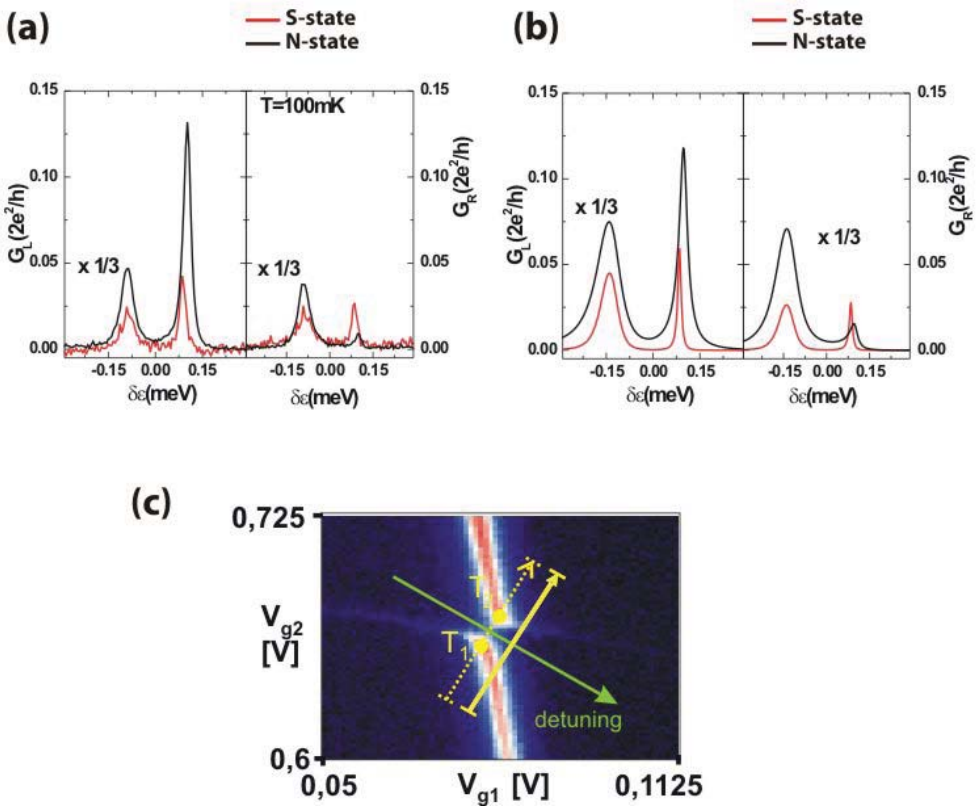

Figure 4.16: (a) We observe 5 triple points which do not fall on the universal linear function $\alpha_S[\alpha_N]$. It turns out that the scanning direction $\delta\epsilon$ of the triple points in question is shifted on the axis of detuning. This shift is suggested by the asymmetry between the peaks in each doublet and the small width of the resonances. (b) If we take a small shift along the axis of detuning into account, we can reproduce our measurement results theoretically. (c) The yellow arrow corresponds to the shifted scanning direction. The original scanning position is illustrated by the dashed arrow.

the five triple points in question separately.

4.2.3 Quantitative comparison of theory and experiment

As explained in subsection (2.6.2), the corresponding theory can be used to model our measurements, extract the contribution of CAR to the total conductance and allows to define a splitting efficiency.
We apply the theory to the two anticrossings AC1 and AC2 presented in figure (4.13). The corresponding stability diagram is depicted in figure (4.6(a)).
By using the corresponding theory (see figure 4.17), Alfredo Levy-Yeyati can nu-

merically fit our measurement data in the normal state (black data curves) and in the superconducting state (red data curves) along the axis $\delta\epsilon$ perpendicular to the anticrossings. As a result he obtains the orange (normal state) and green (superconducting state) curves in figure (4.17). As is visible in the plot, theory and experiment fit together. Additionally, the contribution of CAR is denoted by the black dashed line. Again, this is a numerical result.

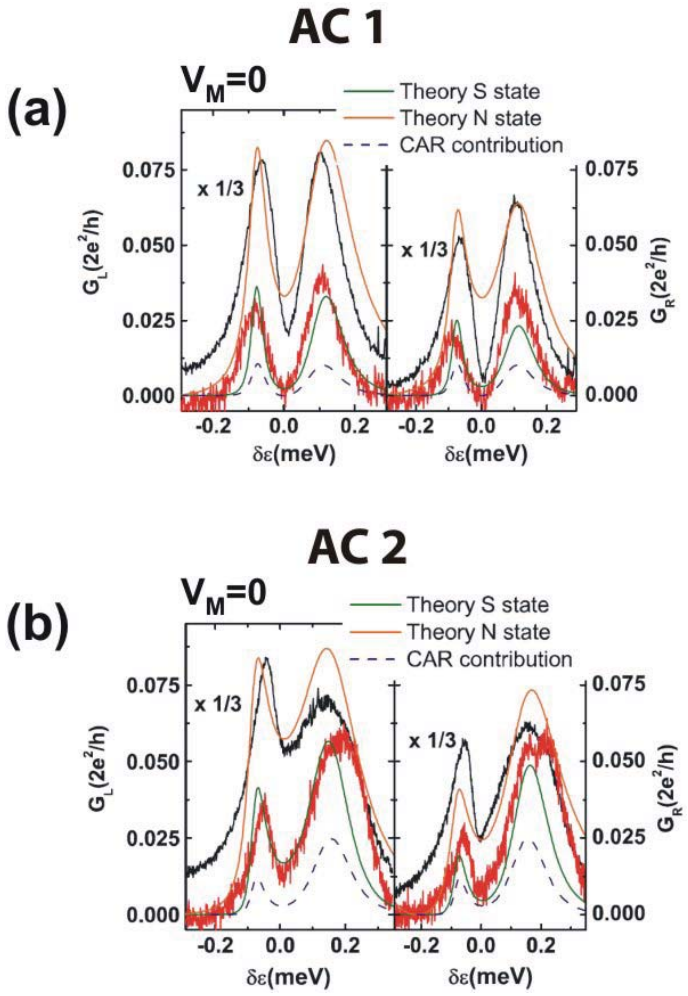

Figure 4.17: We calculate the zero bias conductance at the triple points at middle-injection in the superconducting (green curve) and normal (orange curve) state. We compare the results to our measurements presented in figure (4.13). The dashed black line quantifies the contribution from CAR to the total transport as extracted by Alfredo Levy-Yeyati's theory.

The numerical reproduction of our data is based on the coupling parameters E_{C1},

E_{C2} and Γ_{12} of the double dot beamsplitter. These parameters can be extracted from the stability diagram as illustrated in subsection 4.1.2. Another possibility is to measure the finite bias Coulombdiamonds as illustrated in figure (2.5) for both 1st and 2nd quantum dot. The maximal extension of the diamonds on the V_{sd} scale are exactly equal to E_C, as illustrated in figure (4.18). Concerning the interdot coupling energy of our double quantum dot device, it turned out in subsection 4.1.2 that the coupling energy is nearly entirely composed of the tunnel coupling t. The electrostatic coupling energy U' can therefore be neglected and we assume for the total coupling energy Γ_{12}:

$$\Gamma_{12} = t$$

Due to this fact, we have another possibility to extract the tunnel coupling directly from the plots given in figure (4.13). Consistently with figure (2.11(a)), we simply take half of the separation of the two peaks. This corresponds to the total coupling energy of the two dots.
We discuss in detail the set of parameters of the second anticrossing (AC2), shown in figure (4.17). This anticrossing corresponds to the one which was analyzed in subsection 4.1.2. The set of fitting parameters for AC2 is given by:

$$\begin{aligned} E_{C2} &= 0.595meV \\ E_{C1} &= 0.85meV \\ \Gamma_{12} = t &= 170\mu eV \\ \Gamma_L &= 77\mu eV \\ \Gamma_R &= 110\mu eV \\ \Gamma_{SL} &= 21\mu eV \\ \Gamma_{SR} &= 4\mu eV \end{aligned}$$

Although the values for E_{C1}, E_{C2} slightly differ (around 20%) from the values extracted in subsection 4.1.2, they are on the same order of magnitude. In subsection 4.1.2 we found $E_{C1} = 1,1meV$ and $E_{C2} = 0.5meV$. Here, we extract the data from the finite bias Coulomb diamonds which were measured during the same cool-down as the stability diagram shown in figure (4.6(a)). We measure the finite bias Coulomb diamonds at $B = 63mT$ in the middle-injection setup at left and right normal lead along the gate trajectory of AC2. The result is shown in figure (4.18(a)). As the Coulombdiamonds are not entirely visible in the plots, we interpolate the boundaries of the diamonds to obtain $E_{C1} = 0.85meV$ and $E_{C2} = 0.595meV$. As the Coulomb diamonds are a direct method to determine E_{C1}, E_{C2}, the values $E_{C1} = 0.85meV$

and $E_{C2} = 0.595meV$ are considered more reliable as the values obtained in subsection 4.1.2. Hence it is justified to claim that the parameters used for the numerical fit are consistent with our measurements.

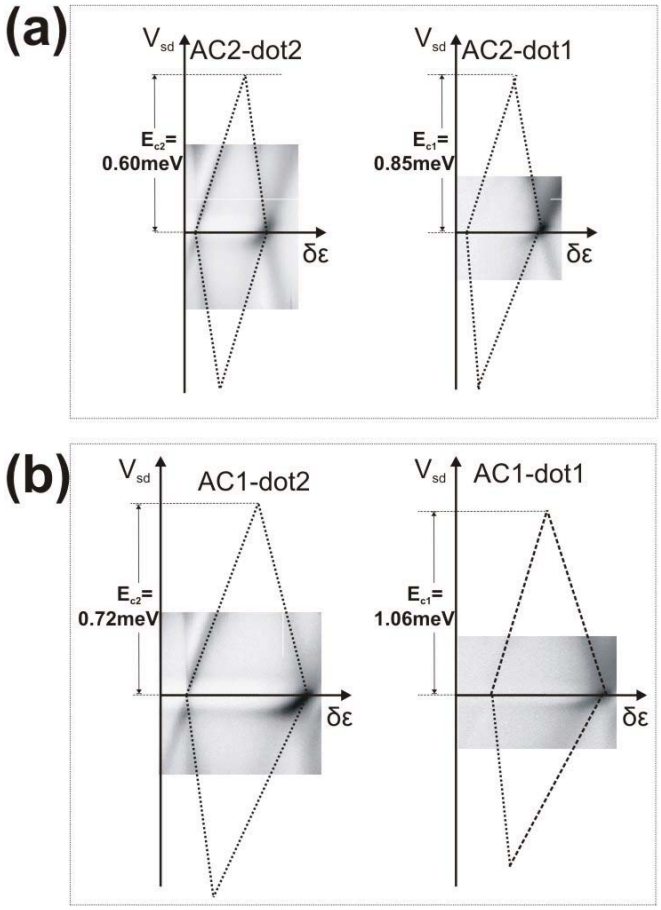

Figure 4.18: (a) The finite bias Coulomb diamonds in the middle-injection setup along AC2 for both dots of the double quantum dot are depicted here. (b) Similar measurement as above along AC1.

Concerning the interdot tunnel coupling, we extract half of the separation of the two peaks of AC2 in figure (4.17(b)). The coupling energy, which is only due to tunnel coupling, is $\Gamma_{12} = t = 170\mu eV$. This result differs from the value for AC2 which was derived in subsection 4.1.2. There we found $\Gamma_{12} = t = (126 \pm 9)\mu eV$. Nevertheless the two values are consistent. This can be explained as follows:
The right peak of AC2 in figure (4.17(b)) has a larger width than the left peak.

We attribute this behavior to a slight tilting of the gate voltage trajectory as illustrated in figure (4.19). The trajectory with the slight mismatch (solid line) is longer than the direct trajectory (dashed line). Hence the energy difference between the peaks of AC2 in figure (4.17(b)) is stretched from $\Gamma_{12} = t = (126 \pm 9)\mu eV$ to $\Gamma_{12} = t = 170\mu eV$.

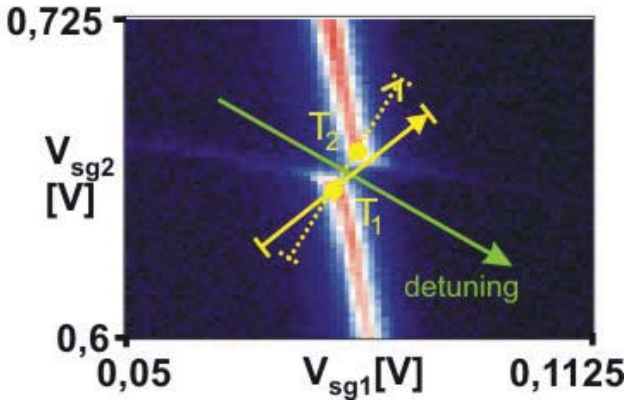

Figure 4.19: In case of the measurement of AC2 presented in figure (4.13), the gate trajectory illustrated by the yellow solid line is slightly tilted. The direct trajectory would correspond to the dashed line.

The parameters used to model the anticrossing AC1 are given by:

$$\begin{aligned} U_L &= 0.72meV \\ U_R &= 1.06meV \\ \Gamma_{12} &= 140\mu eV \\ \Gamma_L &= 68\mu eV \\ \Gamma_R &= 93\mu eV \\ \Gamma_{SL} &= 9\mu eV \\ \Gamma_{SR} &= 13\mu eV \end{aligned}$$

The charging energies are consistent with the values extracted from the Coulomb diamonds measured at middle-injection along the gate trajectory of AC1. The result is illustrated in figure (4.18(b)). Again the data is limited in range and the size of the Coulomb diamonds has to be interpolated. We obtain $E_{C1} = 1,06meV$

and $E_{C2} = 0.72meV$. These values are also consistent with the values extracted in subsection 4.1.2. The same refers to the tunnel coupling. From figure (4.17(a)) we obtain $\Gamma_{12} = 140\mu eV$. As the anticrossings AC1 and AC2 in figure (4.6) look similar, we assume that the coupling energy is the same in the two cases. We can thus compare the value $\Gamma_{12} = 140\mu eV$ obtained for AC1 to the tunnel coupling of AC2 as extracted in subsection 4.1.2 ($\Gamma_{12} = t = (126 \pm 9)\mu eV$). We find that the two values are consistent.

In the superconducting state, we can define a splitting efficiency of our beamsplitter. At the triple points, Cooper pairs either split in a CAR process or tunnel to right or left lead by means of local Andreev Reflection. In subsection (2.6.2), the efficiency is thus defined as the ratio between the CAR contribution to the conductance and the total conductance. As only peak values are considered, we obtain an analytic expression for the splitting efficiency as given by equation 2.51. For each datapoint in figure (4.15) we calculate the splitting efficiency and plot the efficiency as a function of α_N in figure (4.20).

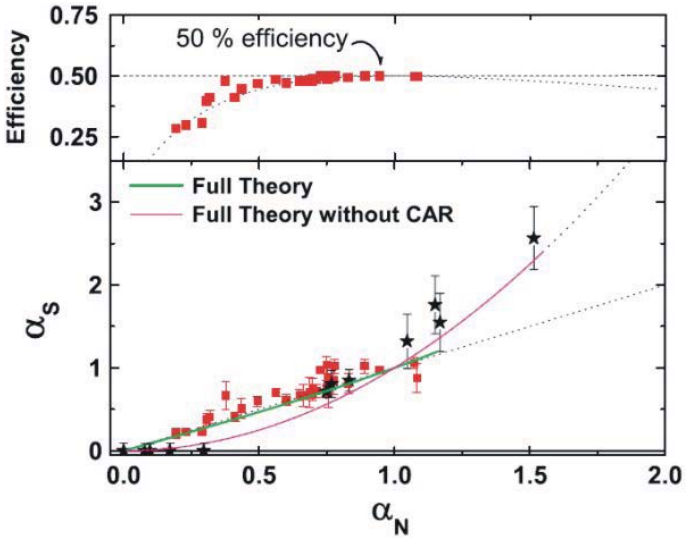

Figure 4.20: We show the splitting efficiency of our Carbon Nanotube beamsplitter for every triple point presented in figure (4.15). Splitting efficiencies up to 50 per cent are reached.

We obtain splitting efficiencies up to 50 per cent. This is the central result of this thesis which shows that we do split Cooper pairs in our Carbon Nanotube beamsplitters.

4.3 Nonlinear transport at triple points

In this section we report on preliminary results on the differential conductance which we obtained at finite bias in the middle-injection setup. At the moment, however, a quantitative theory to gain insight in the charge transport processes is not yet available.

Again we focus on anticrossing AC2 as illustrated in figure (4.6(a)). We choose a gate trajectory $\delta\epsilon$ across the triple points as illustrated in figure (4.21(a)). For each point on the trajectory, we sweep the source-drain voltage V_{sd}. We measure the differential conductance G_L at the left normal lead. The differential conductance at the right normal lead is measured simultaneously but not shown in this figure. It looks very similar to the result for the left lead, only the signal is smaller.
We obtain two-dimensional plots as illustrated in figures (4.21(b)) and (4.21(c)). In figure (4.21(b)) we show the result for zero magnetic field whereas figure (4.21(c)) shows the result for $B = 63mT$.
When we sweep the gates such that we move along the axis $\delta\epsilon$, we intersect the triple points. In figures (4.21(b)) and (4.21(c)) the triple points are labeled by T_1, T_2. In the superconducting case (figure 4.21(b)), the effect of the gap Δ_S is very pronounced at the triple points. We observe a gap of $\Delta_S \sim 85\mu eV$ (see figure 4.21(b)), which corresponds to the minigap of the Pd/Al-bilayer [113]. At the triple points, the conductance resonances penetrate into the gap. The current is due to local and Crossed Andreev Reflection. By applying a magnetic field of $B = 63mT$ (compare figure 4.21(c)), the superconducting gap vanishes. This effect is very pronounced at the triple points.
We make a further observation concerning the interdot tunnel coupling Γ_{12}. The tunnel coupling is given by the distance of the resonance lines as illustrated in figure (4.21(b)). For zero bias this distance corresponds exactly to $\Gamma_{12} \sim 170\mu eV$ as derived in the last section from figure (4.17) for anticrossing AC2. When we go to finite bias, however, we can see in figures (4.21(b)) and (4.21(c)) that the distance of the resonance lines varies as a function of bias. As the interdot coupling energy is a very important parameter for quantitative fits in the finite bias regime, the dependence of Γ_{12} as a function of the applied bias voltage V_{sd} has to be investigated in more detail in future experiments.

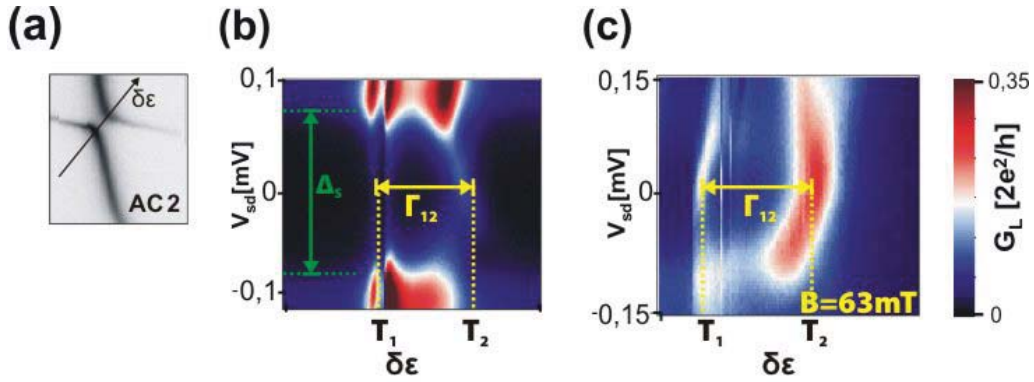

Figure 4.21: (a) The scanning direction is defined as the trajectory across the anticrossing AC2. (b) Finite bias dependence of the differential conductance measured at the left normal lead in the middle injection setup in the superconducting state. (c) The measurement is repeated in the normal state, at $B = 63mT$.

Chapter 5

Discussion and Outlook

In subsection 4.2.1, we show experimentally that CAR are present in our Carbon Nanotube Beamsplitter. We proceed in subsection 4.2.3 with the quantitative evaluation of the contribution of CAR to the total current.
Although we could show the existence of CAR, our method to do so is indirect and based on the qualitative reasoning given in subsection 2.6.1. The indirectness is even more pronounced when we fit our data numerically. Although several input parameters in subsection 4.2.3 are extracted from our measurements, we still have free fitting parameters and small inconsistencies concerning the determination of the input parameters E_{C1}, E_{C2} and Γ_{12} within different methods. This makes us infer that the splitting efficiency which we obtain in subsection 2.6.1 has considerable error bars which are difficult to evaluate.
Concerning the directness to show the inset of CAR at the triple points, the competing experiment by Hofstetter et al. [116] has an advantage compared to our experiment. The authors use the middle-injection setup and measure the differential conductance at first and second lead, simultaneously. As depicted in figure (5.1(a)), they adjust the first quantum dot on a resonant level and only sweep the gate voltage attached to the second dot. They sweep the second quantum dot through a conductance resonance and perform this measurement in the normal as well as in the superconducting state. Special attention is paid to the conductance G_1 measured at the first quantum dot. In the normal state, the sweep of the second dot through a conductance resonance has no effect on the conductance G_1 of the first dot. In the superconducting case, however, the conductance G_1 at the first dot increases once the second dot is swept in a conductance resonance. This additional contribution to the current is attributed to CAR, as no other transport mechanism can account for this correlated particle effect.
Concerning the splitting efficiency, however, Hofstetter et al. attain lower values than we do. From figure (5.1(b)) we can extract a splitting efficiency around 1%.

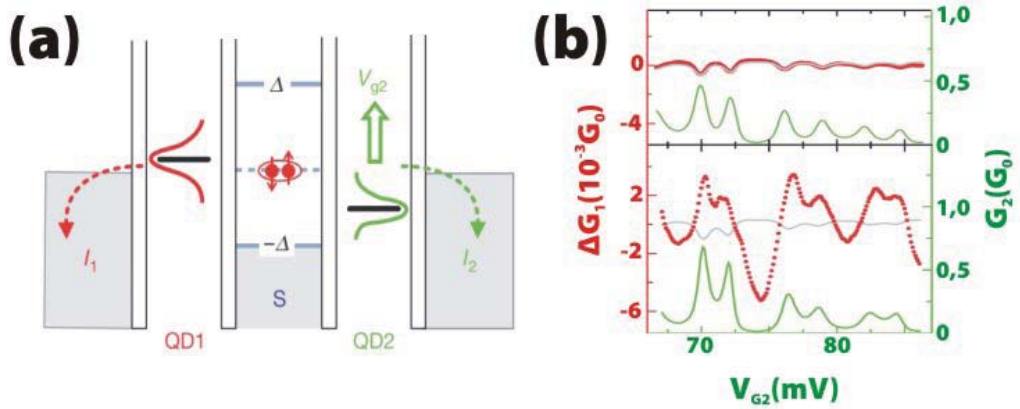

Figure 5.1: (a) The measurement method of the Basel group: In the middle-injection setup, the differential conductance is measured at 1st and 2nd lead. The 1st quantum dot is held at resonance while the 2nd dot is swept through a conductance resonance. (b) The additional conductance measured at the 1st lead is attributed to CAR. (Figures taken from reference [116])

We wonder why the two experiments lead to such a big difference concerning the splitting efficiency. We assume that the sample used by Hofstetter et al. possesses low interdot coupling Γ_{12}. Hence we also suppose that tunnel coupling is low in their sample, which could be responsible for the low splitting efficiency. In their publication, the interdot coupling regime is not entirely investigated, as the authors do not show a stability diagram of their sample. In contrast to Hofstetter et al., our device is measured in the regime of strong interdot coupling. Furthermore tunnel coupling outweighs electrostatic coupling which allows the two electrons of an incoming Cooper pair to form a molecular state on the double dot. As we obtain much higher splitting efficiencies than Hofstetter et al., high tunnel coupling seems to be more favorable for the splitting process than low tunnel coupling.
In a recent article [66], it is pointed out that the experiment presented in this thesis may help to pave the way to further explore nonlocal effects in solid state systems. The author also speaks about possible applications such as teleportation or ultrasecure communication (see section 1.2). We think that applications are not close at hand at the moment, but a greater understanding of the possibility to create entangled states in solid state devices is very important from a merely scientific point of view. This absolutely justifies further investigations: Tests of nonlocality in a solid state system would be a scientific breakthrough. Together with the work by Hofstetter et al. [116], our work opens a new research field in this context.

This brings us to the question how the research field will develop and what experiments are next at hand. To give a judgement it is necessary to define the ultimate goal and identify a series of intermediate steps.
The ultimate goal is to test Bell's inequalities and thus prove that the split Cooper pairs are still entangled. In order to come to this point, one has to achieve three intermediate goals: The first thing is to find a tool to detect the entangled state. In solid state physics an appropriate method to do so is to measure shot noise cross correlations. Hence one milestone is to design a sensitive noise measurement setup. Electrical current is the consequence of a potential difference applied across a resistor. As a function of time, current is not constant but rather shows tiny stochastic oscillations (see figure 5.2(a)). What is typically measured in a standard resistance measurement is the average value of the current, named I_0. The statistical oscillations, however, are very sensitive to electronic interactions within a conductor.
This can be used to probe the simultaneous arrival of charge carriers at left and right contact of our beamsplitter device. The point of departure are spectra as illustrated in figure (5.2(a)), for both left and right lead. If we calculate the correlation function of the two spectra, the so-called cross-correlations, we have a tool to make a statement concerning the simultaneous arrival of particles.
The experiment to measure shot noise cross correlations between the normal contacts of a beamsplitter geometry involving a superconducting source contact is suggested in several publications [70], [69], [71], [117], [62]. Furthermore it is pointed out, that entangled electrons would lead to positive cross correlations (see figure 5.2(b)), given that the superconductor-nanotube junction is in an intermediate transparency regime. The cross-correlation noise spectral density is given by:

$$S_{12}(f) = 2\int_{-\infty}^{\infty} d\tau \langle \delta I_1(t)\delta I_2(t+\tau)\rangle e^{2i\pi f\tau} \tag{5.1}$$

However, positive cross-correlations alone do not prove entanglement yet. Strictly speaking positive correlations are only a proof of charge correlation, not of spin.
That means that the second milestone is to realize a sample with ferromagnetic contacts to allow spin-filtering. In order to prove the entanglement of the particles, one has to be sure that only particles of a predefined spin orientation enter left and right lead, respectively. This is very important and is the analogon to the polarizers in the optical experiment (see figure 1.2). Finally, one has to investigate the finite bias conductance regime of the structure. Shot noise always is a function of the current passing through the conductor and hence a finite bias effect. Therefore it is inevitable to study the finite bias conductance of our double quantum dot beamsplitter device in the middle-injection setup.

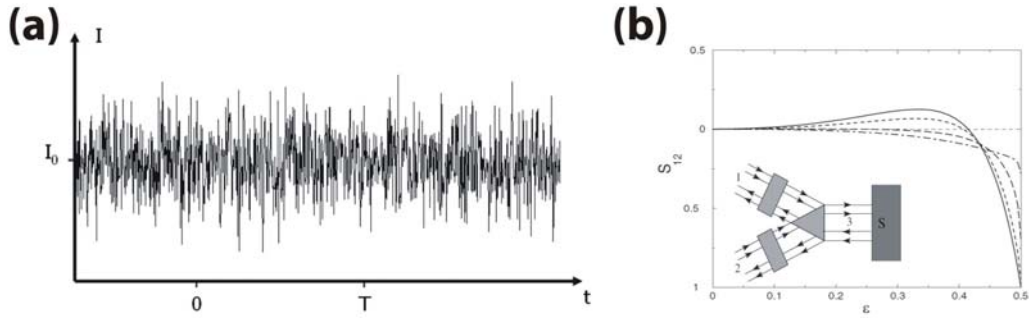

Figure 5.2: (a) Typical current noise spectrum as a function of time (taken from [118]). (b) Current-current noise correlations at both ends of the nanotube as a function of the transparency ϵ between superconductor and nanotube (taken from [70]).

Chapter 6

Conclusion

In this work, we have made a first step towards a solid-state entangler which could be used as a basic building block in quantum-computation like devices. We showed that Cooper pairs coming from the central electrode of a Y-structured beamsplitter geometry can be split into two normal leads. In some more detail our results can be described as follows:

First, we showed by means of transport measurements that our carbon nanotubes are of sufficiently high quality to deliver regular spaced Coulomb diamonds. Another achievement is the control of contact resistances: We reliably fabricated contact resistances leading to Coulomb-blockade behavior. The control of the contact resistance of the superconducting contact was the most difficult part in this context: The contact between the nanotube and pure aluminum turned out to be too resistive. To solve this problem we replaced the pure aluminum by an aluminium/Pd bilayer which was adjusted such that our device had a room temperature contact resistance around $30k\Omega$ and a superconducting gap around $100\mu eV$ at low temperature.

Second, the experimentally observed stability diagram confirmed the non trivial fact that our samples act as double dots. This is non-trivial because we do not have a topgate in the middle of our nanotube which defines two separate dots, as was done in previous devices. Instead, we deposit our superconducting electrode in the middle of the tube which fulfils a double function: It serves as a Cooper pair injector and at the same time it creates a potential barrier which separates the Single-Walled nanotube in two quantum dots. Another very important observation is that the stability diagram does not depend on the fact whether we inject at one of the normal contacts and measure at the other normal contact or if we inject at the superconducting contact and measure at one or both normal contacts. It looks the same in all cases.

Third, we developed a method how to show, by means of simultaneous conductance measurements at left and right lead, that we split the Cooper pairs. We present a slightly simplified but very intuitive argument how the ratio G_R/G_L at triple points and single resonances gives insight into the microscopic nature of transport: Taking resonances within the stability diagram, G_R/G_L in the superconducting state plotted against G_R/G_L in the normal state depend drastically on the fact whether the resonances are triple points or single resonances. For the triple points, $\alpha_S[\alpha_N]$ shows a linear behavior, whereas the ensemble of analysed single resonances describes a parabola. Furthermore we present a fully interacting theory implemented by Alfredo Levy Yeyati, whose results only show small deviations from the qualitative argument. Theory and experiment are consistent. Finally, we can use the full theory to extract the contribution of CAR to the total transport. In this way we can state that a CAR contribution up to 50% can be expected in the strong coupling regime.

Appendix A

CVD growth of Single-Walled Carbon Nanotubes

A.1 Catalyst recipe for Single-Walled Carbon Nanotubes

- $Fe(NO_3)_3 9H_2O$: 80,4mg
- $MoO_2(acac)_2$: 4,1mg
- $Al(nanoparticles)$: 60,8mg
- $Methanol$: 60ml

A.2 Growth process - Paris

- growth temperature: 900°C
- start: flush the tube with all used gases at the used flow rates for 2min
- heating: Argon, 1500 ml/min
- growth preparation: Hydrogen, 240ml/min, 10min
- growth: Hydrogen, 240ml/min and Methane, 1000ml/min, 10min
- cool down to 500°C: Hydrogen, 240ml/min and Argon, 1500ml/min
- cool down to room temperature: Argon, 1500ml/min

A.3 Growth process - Regensburg

- growth temperature: 900°C
- start: flush the tube with all used gases at the used flow rates for 2min
- heating: Argon, 1500 ml/min
- growth: Hydrogen, 700ml/min and Methane, 800ml/min, 15min
- cool down: open the furnace directly after growth
- cool down to 500°C: Hydrogen, 700ml/min and Argon, 1500ml/min, furnace closed
- cool down to room temperature: Argon, 1500ml/min, furnace closed

Appendix B

Printed-Circuit-Bord

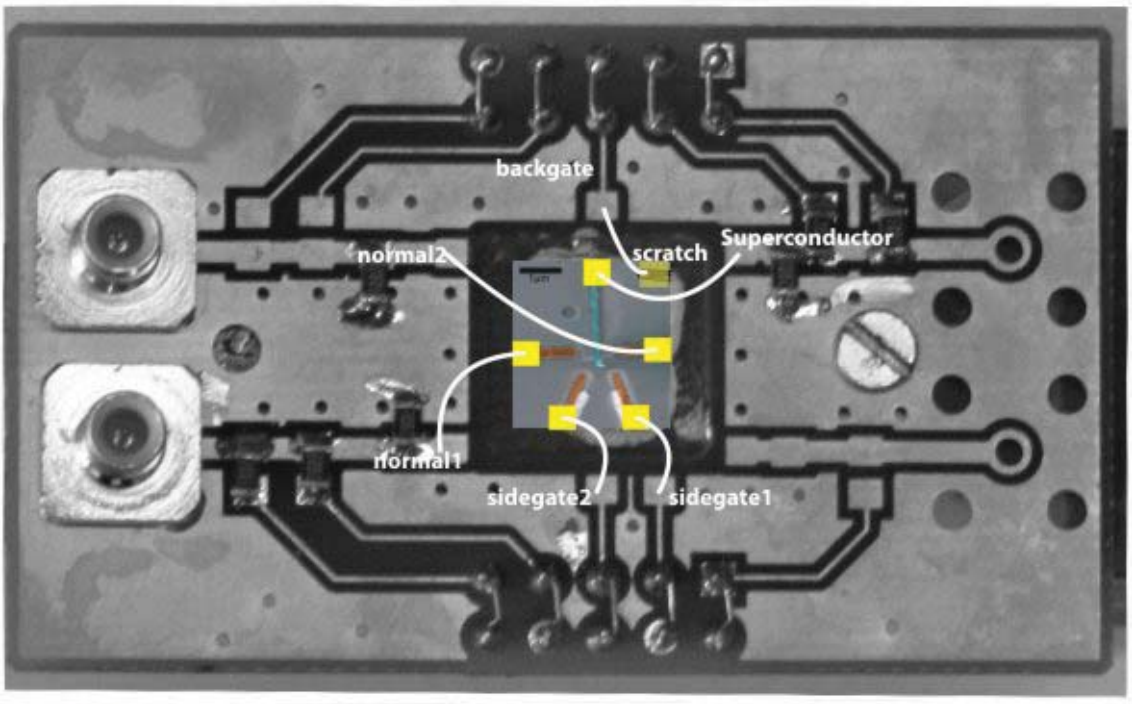

Figure B.1: The Printed-Circuit-Bord used for our measurements. To illustrate how the sample was mounted on chip, a sketch of the sample is put in the middle of our sample holder. The contact pads of the sample contacts are bonded to the respective pads of the PCB. Note that at the corner of the sample we scratch the wafer and thus destroy the oxide layer between surface and bulk. We can thus connect the backgate of the chip with a contact pad on our sample holder.

Appendix C

Finding the working point of the beamsplitter

In figure C.1, we illustrate how to find suitable gate voltage ranges for our experiment. This preliminary work is done in the side-injection scheme as defined in figure (4.2). In principle, we have to adjust three parameters: V_{bg}, V_{g1} and V_{g2}.
We leave the two sidegates at zero voltage and start with the adjustment of the backgate voltage. In our experiment, the backgate voltage together with the potential barrier created by depositing the middle contact on our tube can be thought of as an analog of the central gate in previous devices (see e.g. reference [22]). Hence the backgate voltage is crucial because it defines the coupling of the two quantum dots.
At 4K we measure Coulomb oscillations at zero bias between the normal contacts as a function of the backgate. Clearly we can see that our nanotube is semiconducting and has a pinch off around +2V (see figure C.1(a)). Next we cool our sample to base temperature, which is 80mK in our case. As thermal smearing is reduced at low temperatures, Coulomb peaks become sharper. As indicated in figure (C.1(b)) we set the backgate voltage in a region of low conductance, preferably not too far away from the pinch off. This increases the chance to observe a double dot behavior rather than a single dot behavior of our sample. Having adjusted the backgate to a constant voltage we start sweeping sidegate 1. We investigate a large gate voltage range $-10V...10V$ and look for a regular spaced pattern as shown in figure (C.1(c)). Last but not least we set sidegate voltage 1 to a constant value, too, and sweep the second sidegate. If we obtain again a regular spaced pattern as the one in figure (C.1(d)), the chance is high to find a promising double dot gate voltage configuration. The next step is to start a detailed measurement of the stability diagram: The conductance is measured as a function of the two sidegates and the honeycomb stability diagram is supposed to occur.

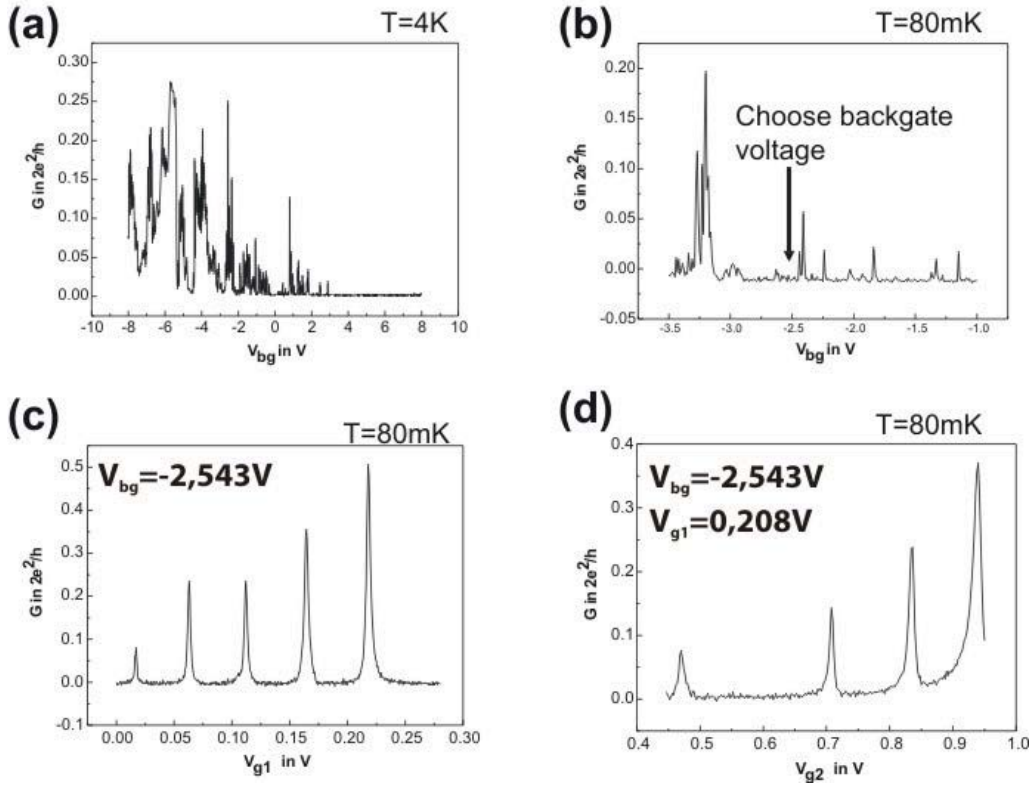

Figure C.1: In (a) Coulomb oscillations between the two normal contacts at T=4K are depicted. Clearly, the nanotube is semiconducting with a pinch-off voltage around 2V. (b) We choose a smooth gate region to fix the backgate voltage. In (c) we sweep sidegate 1. Once we find nice oscillations we fix sidegate 1. (d) Next we sweep sidegate 2. If we find nice oscillattions also as a function of sidegate 2, we start the measurement of the stability diagram.

Appendix D

Determination of the current going to the superconductor in the side-injection setup

We determine the current I_2 going to the superconductor in the side-injection setup. The setup is illustrated in figure (4.4). In the side-injection setup we measure the parameters I_1, I_3. We switch to the middle-injection setup and measure G_{RS}, G_{LS}. We apply a bias voltage $U_{ac} = 1,8\mu V$. By using equation 4.4 we can henceforth determine the current I_2.
We study the left triple point illustrated in figure (D.1). We obtain the following results:

$$G_{LS} = 0,069\frac{e^2}{h} \tag{D.1}$$

$$G_{RS} = 0,028\frac{e^2}{h} \tag{D.2}$$

$$I_1 = 0,83nA \tag{D.3}$$

$$I_3 = 0,0537nA \tag{D.4}$$

$$I_2 = 0,023nA \tag{D.5}$$

$$\tag{D.6}$$

Hence the current going to the second normal reservoir is a factor $2,4$ times bigger than the current going to the superconductor.

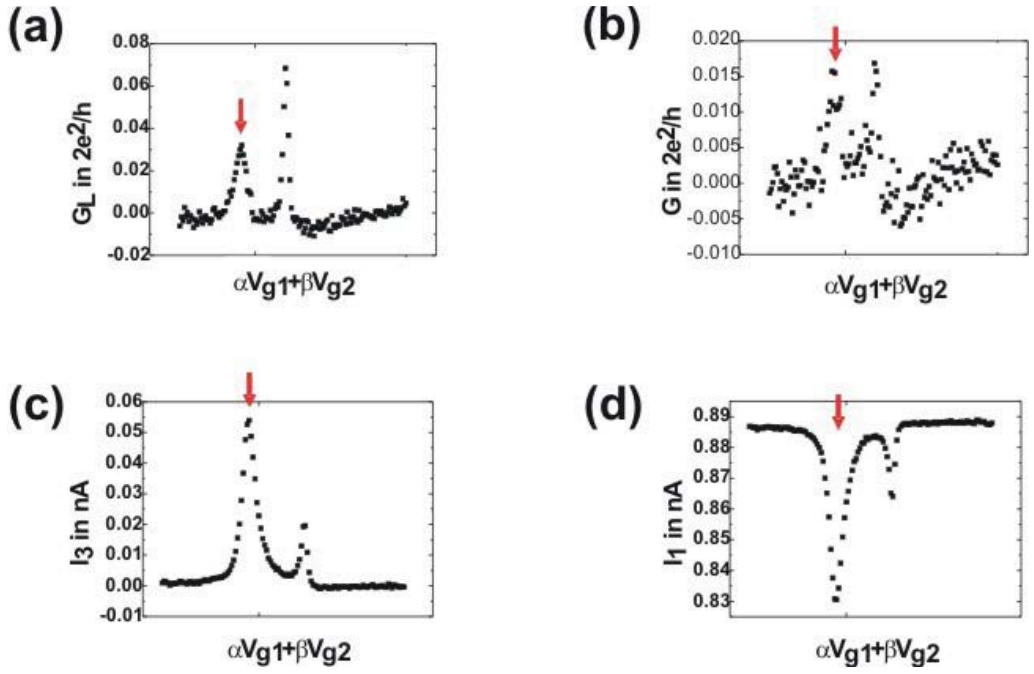

Figure D.1: We measure the differential conductance in the middle-injection setup at left (a) and right (b) lead. Afterwards we switch to the side-injection setup and measure the same region again. We measure I_1 and I_3 as defined in figure (4.4).

Bibliography

[1] M. Kastner. 'Artificial atoms.' Physics Today, 46 (1):24 (1993).

[2] M. T. Björk, C. Thelander, A. E. Hansen, L. Jensen, M. W. Larsson, L. Reine-Wallenberg and L. Samuelson. 'Few-electron quantum dots in nanowires.' Nano Letters, 4 (9):1621 (2004).

[3] M. T. Björk, A. Fuhrer, A. E. Hansen, M. W. Larsson, L. E. Fröberg and L. Samuelson. 'Tunable effective g factor in inas nanowire quantum dots.' Phys. Rev. B, 72 (20):201307 (2005).

[4] C. Fasth, A. Fuhrer, L. Samuelson, V. N. Golovach and D. Loss. 'Direct measurement of the spin-orbit interaction in a two-electron inas nanowire quantum dot.' Phys. Rev. Lett., 98 (26):266801 (2007).

[5] H. Postma, T. Teepen, Z. Yao, M. Grifoni and C. Dekker. 'Carbon nanotube single-electron transistors at room temperature.' Science, 293:76 (2001).

[6] W. Liang, M. Shores, M. Bockrath, J. Long and H. Park. 'Kondo resonance in a single-molecule transistor.' Nature, 417:725 (2002).

[7] O. Millo, D. Katz, Y. Cao and U. Banin. 'Imaging and spectroscopy of artificial-atom states in core/shell nanocrystal quantum dots.' Phys. Rev. Lett., 86 (25):5751 (2001).

[8] U. Banin, Y. Cao and O. Millo. 'Identification of atomic-like electronic states in indium arsenide nanocrystal quantum dots.' Nature, 400:542 (1999).

[9] P. Hawrylak. 'Single-electron capacitance spectroscopy of few-electron artificial atoms in a magnetic field: Theory and experiment.' Phys. Rev. Lett., 71 (20):3347 (1993).

[10] M. Kastner. 'The single electron transistor and artificial atoms.' Ann. Phys. (Leipzig), 9 (11-12):885 (2000).

[11] J. Kondo. 'Resistance minimum in dilute magnetic alloys.' Prog. Theor. Phys., 32:37 (1964).

[12] T. Delattre, C. Feuillet-Palma, L. Herrmann, P. Morfin, J.-M. Berroir, G. Féve, B. Placais, D. Glattli, M.-S. Choi, C. Mora and T. Kontos. 'Noisy kondo impurities.' Nature Physics, 5:208 (2009).

[13] J. Nygard, D. Cobden and P. Lindelof. 'Kondo physics in carbon nanotubes.' Nature, 408:342 (2000).

[14] D. Goldhaber-Gordon, S. H., D. Mahalu, A.-M. D., U. Meirav and K. M.A. 'Kondo effect in a single-electron transistor.' Nature, 391:156 (1998).

[15] P. Michler, A. Imamoğlu, M. Mason, P. Carson, G. Strouse and S. Buratto. 'Quantum correlation among photons from a single quantum dot at room temperature.' Nature, 406:968 (2000).

[16] R. Warburton, C. Schäflein, D. Haft, F. Bickel, A. Lorke, K. Karrai, J. Garcia, W. Schoenfeld and P. Petroff. 'Optical emission from a charge-tunable quantum ring.' Nature, 405:926 (2000).

[17] A. Wallraff, D. Schuster, A. Blais, L. Frunzio, R.-S. Huang, J. Majer, S. Kumar, S. Girvin and R. Schoelkopf. 'Stong coupling of a single photon to a superconducting qubit using circuit quantum electrodynamics.' Nature, 431:162 (2004).

[18] S. Bednarek, T. Chwiej, J. Adamowski and B. Szafran. 'Artificial molecules in coupled and single quantum dots.' Phys. Rev. B, 67 (20):205316 (2003).

[19] J. Gorman, D. G. Hasko and D. A. Williams. 'Charge-qubit operation of an isolated double quantum dot.' Phys. Rev. Lett., 95 (9):090502 (2005).

[20] M. Rontani, F. Rossi, F. Manghi and E. Molinari. 'Multiple quantum phases in artificial double-dot molecules.' Solid State Comm., 112:151 (1999).

[21] N. Mason, M. Biercuk and C. Marcus. 'Local gate control of a carbon nanotube double quantum dot.' Science, 303:655 (2004).

[22] M. R. Gräber, W. A. Coish, C. Hoffmann, M. Weiss, J. Furer, S. Oberholzer, D. Loss and C. Schönenberger. 'Molecular states in carbon nanotube double quantum dots.' Phys. Rev. B, 74 (7):075427 (2006).

[23] H. Pothier, P. Lafarge, C. Urbina, D. Esteve and M. Devoret. 'Single-electron pump based on chargin effects.' Europhys. Lett., 17 (3):249 (1992).

[24] A. Holleitner, R. Blick, A. Hüttel, K. Eberl and J. Kotthaus. 'Probing and controlling the bonds of an artificial molecule.' Science, 297:70 (2002).

[25] A. Furher, C. Fasth and L. Samuelson. 'Single electron pumping in inas nanowire double quantum dots.' Appl. Phys. Lett., 91 (052109) (2007).

[26] A. Pfund, I. Shorubalko, K. Ensslin and R. Leturcq. 'Suppression of spin relaxation in an inas nanowire double quantum dot.' Phys. Rev. Lett., 99 (3):036801 (2007).

[27] A. Einstein, B. Podolsky and N. Rosen. 'Can quantum-mechanical description of physical reality be considered complete?' Phys. Rev., 47 (10):777 (1935).

[28] D. Bohm. 'Quantum theory.' Englewood Cliffs, NJ: Prentice Hall, 614–622 (1951).

[29] C. Cohen-Tannoudji, B. Diu and F. Laloe. *Quantenmechanik, Tl.2* (de Gruyter, 1999), 2nd edn.

[30] J. Bell. 'On the einstein-podolsky-rosen paradox.' Physics, 1:195 (1965).

[31] J. F. Clauser and M. A. Horne. 'Experimental consequences of objective local theories.' Phys. Rev. D, 10 (2):526 (1974).

[32] P. Hemmer and W. J. 'Where is my quantum computer?' Science, 324:473 (2009).

[33] D. Deutsch. 'Quantum theory, the church-turing principle and the universal quantum computer.' Proc. R. Soc. Lond. A, 400:97 (1985).

[34] D. Deutsch. 'Quantum computational networks.' Proc. R. Soc. Lond. A, 425:73 (1989).

[35] S. Lloyd. 'A potentially realizable quantum computer.' Science, 261:1569 (1993).

[36] P. Shor. 'Algorithms for quantum computation: discrete logarithms and factoring.' Proceedings, 35th Annual Symposium on Foundations of Computer Science (1994).

[37] B. Schumacher. 'Quantum coding.' Phys. Rev. A, 51 (4):2738 (1995).

[38] B. Schumacher. 'Sending entanglement through noisy quantum channels.' Phys. Rev. A, 54 (4):2614 (1996).

[39] C. H. Bennett and S. J. Wiesner. 'Communication via one- and two-particle operators on einstein-podolsky-rosen states.' Phys. Rev. Lett., 69 (20):2881 (1992).

[40] M. Nielsen and I. Chuang. *Quantum Computation and Quantum Information* (Cambridge University Press, 2000), 1st edn.

[41] I. Chuang, L. Vandersypen, X. Zhou, D. Leung and S. Lloyd. 'Experimental realization of a quantum algorithm.' Nature, 393:143 (1998).

[42] I. L. Chuang, N. Gershenfeld and M. Kubinec. 'Experimental implementation of fast quantum searching.' Phys. Rev. Lett., 80 (15):3408 (1998).

[43] J. Jones, M. Mosca and R. Hansen. 'Implementation of a quantum search algorithm on a quantum computer.' Nature, 393:344 (1998).

[44] S. Gulde, M. Riebe, G. Lancaster, C. Becher, J. Eschner, H. Häffner, F. Schmidt-Kaler, I. Chuang and R. Blatt. 'Implementation of the deutsch-josza algorithm on an ion-trap quantum computer.' Nature, 421:48 (2003).

[45] K.-A. Brickman, P. C. Haljan, P. J. Lee, M. Acton, L. Deslauriers and C. Monroe. 'Implementation of grover's quantum search algorithm in a scalable system.' Phys. Rev. A, 72 (5):050306 (2005).

[46] P. Kwiat, J. Mitchell, P. Schwindt and A. White. 'Grover's search algorithm: an optical approach.' J. Mod. Opt., 47:257 (2000).

[47] M. Gurudev Dutt, L. Childress, L. Jiang, E. Togan, J. Maze, F. Jelezko, A. A. S. Zibrov, R. Hemmer and M. Lukin. 'Quantum register based on individual electronic and nuclear spin qubits in diamond.' Science, 316:1312 (2007).

[48] D. Loss and D. P. DiVincenzo. 'Quantum computation with quantum dots.' Phys. Rev. A, 57 (1):120 (1998).

[49] G. Burkard, D. Loss and D. P. DiVincenzo. 'Coupled quantum dots as quantum gates.' Phys. Rev. B, 59 (3):2070 (1999).

[50] J. Clarke and F. Wilhelm. 'Superconducting quantum bits.' Nature, 453:1031 (2008).

[51] E. Knill. 'Quantum computing.' Nature, 463:441 (2010).

[52] M. Hofheinz, H. Wang, M. Ansmann, R. Bialczak, E. Lucero, M. Neeley, A. O'Connell, D. Sank, J. Wenner, J. Martinis and A. Cleland. 'Synthesizing arbitrary quantum states in a superconducting resonator.' Nature, 459:546 (2009).

[53] M. Hofheinz, E. Weig, M. Ansmann, R. Bialczak, E. Lucero, M. Neeley, A. O'Connell, H. Wang, J. Martinis and A. Cleland. 'Generation of fock states in a superconducting quantum circuit.' Nature, 454:310 (2008).

[54] A. O'Connell, M. Hofheinz, M. Ansmann, R. Bialczak, M. Lenander, E. Lucero, M. Neeley, D. Sank, H. Wang, M. Weides, J. Wenner, J. Martinis and A. Cleland. 'Quantum ground state and single-phonon control of a mechanical resonator.' Nature, 464:697 (2010).

[55] L. Frunzio, A. Wallraff, D. Schuster, J. Majer and R. Schoelkopf. 'Fabrication and characterization of superconductingcircuit qed devices for quantum computation.' IEEE TRANSACTIONS ON APPLIED SUPERCONDUCTIVITY, 15 (2):860 (2005).

[56] M. Steffen, M. Ansmann, R. Bialczak, N. Katz, E. Lucero, R. McDermott, M. Neeley, E. Weig, A. Cleland and J. Martinis. 'Measurement of the entanglement of two superconducting qubits via state tomography.' Science, 313:1423 (2006).

[57] M. Ansmann, H. Wang, R. Bialczak, M. Hofheinz, E. Lucero, M. Neeley, A. O'Connell, D. Sank, M. Weides, J. WEnner, A. Cleland and J. Martinis. 'Violation of bell's inequality in josephson phase qubits.' Nature, 461:504 (2009).

[58] J. Friedman, V. Patel, W. Chen, S. Tolpygo and J. Lukens. 'Quantum superpositions of distinct macroscopic states.' Nature, 406:43 (2000).

[59] C. van der Wal, A. ter Haar, F. Wilhelm, R. Schouten, C. Harmans, T. Orlando, S. Lloyd and J. Mooij. 'Quantum superposition of macroscopic persistent-current states.' Science, 290:773 (2000).

[60] D. Vion, A. Aassime, A. Cottet, P. Joyez, H. Pothier, C. Urbina, D. Esteve and M. Devoret. 'Manipulating the quantum state of an electrical circuit.' Science, 296:886 (2002).

[61] J. M. Martinis, S. Nam, J. Aumentado and C. Urbina. 'Rabi oscillations in a large josephson-junction qubit.' Phys. Rev. Lett., 89 (11):117901 (2002).

[62] P. Recher and D. Loss. 'Superconductor coupled to two luttinger liquids as an entangler for electron spins.' Phys. Rev. B, 65 (16):165327 (2002).

[63] J. M. Kikkawa, I. P. Smorchkova, N. Samarth and D. D. Awschalom. 'Room-temperature spin memory in two-dimensional electron gases.' Science, 277:1284 (1997).

[64] J. M. Kikkawa and D. D. Awschalom. 'Resonant spin amplification in n-type gaas.' Phys. Rev. Lett., 80 (19):4313 (1998).

[65] D. Awschalom and J. Kikkawa. 'Electron spin and optical coherence in semiconductors.' Physics Today, 52 (6):33 (1999).

[66] N. Mason. 'Carbon nanotubes help pairs survive a breakup.' Physics, 3 (3) (2010).

[67] A. Blais, J. Gambetta, A. Wallraff, D. I. Schuster, S. M. Girvin, M. H. Devoret and R. J. Schoelkopf. 'Quantum-information processing with circuit quantum electrodynamics.' Phys. Rev. A, 75 (3):032329 (2007).

[68] L. DiCarlo, J. Chow, G. J.M., L. Bishop, B. Johnson, D. Schuster, J. Majer, A. Blais, L. Frunzio, S. Grivin and R. Schoelkopf. 'Demonstration of two-qubit algorithms with a superconducting quantum processor.' Nature, 460:240 (2009).

[69] A. Crépieux, R. Guyon, P. Devillard and T. Martin. 'Electron injection in a nanotube: Noise correlations and entanglement.' Phys. Rev. B, 67 (20):205408 (2003).

[70] V. Bouchiat, N. Chtchelkatchev, D. Feinberg, G. Lesovik, T. Martin and J. Torres. 'Single-walled carbon nanotube-superconductor entangler: noise correlations and einstein-podolsky-rosen states.' Nanotechnology, 14:77 (2003).

[71] N. M. Chtchelkatchev, G. Blatter, G. B. Lesovik and T. Martin. 'Bell inequalities and entanglement in solid-state devices.' Phys. Rev. B, 66 (16):161320 (2002).

[72] I. Sumio. 'Helical microtubules of graphitic carbon.' Nature, 354:56 (1991).

[73] S. Saito, G. Dresselhaus and M. Dressehlaus. *Physical Propberties of Carbon Nanotubes* (Imperial College Press, 2003), 1st edn.

[74] Y. M. Blanter and M. Büttiker. 'Shot noise in mesoscopic conductors.' Phys. Rep., 336:1 (2000).

[75] S. Datta. *Electronic Transport in Mesoscopic Systems* (Cambridge University Press, 1997), 1st edn.

[76] C. Glattli. *Mesoscopic physics, DEA lectures* (ENS Paris, 2006).

[77] W. Liang, M. Bockrath, D. Bozovic, J. H. Hafner, M. Tinkham and H. Park. 'Fabry-perot interference in a nanotube electron waveguide.' Nature, 411:665 (2001).

[78] C. W. J. Beenakker. 'Theory of coulomb-blockade oscillations in the conductance of a quantum dot.' Phys. Rev. B, 44 (4):1646 (1991).

[79] D. Averin and K. Likharev. 'Coulomb blockade of single-electron tunnelling, and coherent oscillations in small tunnel junctions.' Journal of Low Temperature Physics, 62 (3):345 (1986).

[80] C. W. J. Beenakker. 'Random-matrix theory of quantum transport.' Rev. Mod. Phys., 69 (3):731 (1997).

[81] R. Hanson, L. P. Kouwenhoven, J. R. Petta, S. Tarucha and L. M. K. Vandersypen. 'Spins in few-electron quantum dots.' Rev. Mod. Phys., 79 (4):1217 (2007).

[82] S. De Franceschi, S. Sasaki, J. M. Elzerman, W. G. van der Wiel, S. Tarucha and L. P. Kouwenhoven. 'Electron cotunneling in a semiconductor quantum dot.' Phys. Rev. Lett., 86 (5):878 (2001).

[83] L. J. Geerligs, D. V. Averin and J. E. Mooij. 'Observation of macroscopic quantum tunneling through the coulomb energy barrier.' Phys. Rev. Lett., 65 (24):3037 (1990).

[84] C. Kane, L. Balents and M. P. A. Fisher. 'Coulomb interactions and mesoscopic effects in carbon nanotubes.' Phys. Rev. Lett., 79 (25):5086 (1997).

[85] D. H. Cobden, M. Bockrath, P. L. McEuen, A. G. Rinzler and R. E. Smalley. 'Spin splitting and even-odd effects in carbon nanotubes.' Phys. Rev. Lett., 81 (3):681 (1998).

[86] W. G. van der Wiel, S. De Franceschi, J. M. Elzerman, T. Fujisawa, S. Tarucha and L. P. Kouwenhoven. 'Electron transport through double quantum dots.' Rev. Mod. Phys., 75 (1):1 (2002).

[87] R. H. Blick, R. J. Haug, J. Weis, D. Pfannkuche, K. v. Klitzing and K. Eberl. 'Single-electron tunneling through a double quantum dot: The artificial molecule.' Phys. Rev. B, 53 (12):7899 (1996).

[88] C. Cohen-Tannoudji, B. Diu and F. Laloe. *Quantenmechanik, Tl.1* (de Gruyter, 1999), 2nd edn.

[89] J. Bardeen, L. N. Cooper and J. R. Schrieffer. 'Theory of superconductivity.' Phys. Rev., 108 (5):1175 (1957).

[90] P. De Gennes. *Superconductivity of Metals and Alloys* (Westview Press, 1999), 3rd edn.

[91] S. Oh and J. Kim. 'Entanglement of electron spins in superconductors.' Phys. Rev. B, 71 (14):144523 (2005).

[92] E. Dupont and K. Le Hur. 'Decoherence of einstein-podolsky-rosen pairs in a noisy andreev entangler.' Phys. Rev. B, 73 (4):045325 (2006).

[93] D. Weiss. *Festkörperphysik* (lecture, University of Regensburg, 2006).

[94] A. Andreev. Sov.Phys.-JETP, 51 (11) (1964).

[95] A. Fauchere. 'Transport and magnetism in mesoscopic superconductors.' Diss. Naturwiss. ETH Zürich, Nr. 13068 (1999).

[96] D. S. Golubev and A. D. Zaikin. 'Non-local andreev reflection in superconducting quantum dots.' Phys. Rev. B, 76 (18):184510 (2007).

[97] J. P. Morten, A. Brataas and W. Belzig. 'Circuit theory of crossed andreev reflection.' Phys. Rev. B, 74 (21):214510 (2006).

[98] A. Anthore, H. Pothier and D. Esteve. 'Density of states in a superconductor carrying a supercurrent.' Phys. Rev. Lett., 90 (12):127001 (2003).

[99] W. Buckel. *Supraleitung* (Wiley-VCH, 1995), 5th edn.

[100] S. Russo, M. Kroug, T. M. Klapwijk and A. F. Morpurgo. 'Experimental observation of bias-dependent nonlocal andreev reflection.' Phys. Rev. Lett., 95 (2):027002 (2005).

[101] A. Kleine, A. Baumgartner, J. Trbovic and C. Schönenberger. 'Contact resistance dependence of crossed andreev reflection.' Europhys. Lett., 87:27011 (2009).

[102] G. Deutscher and D. Feinberg. 'Coupling superconducting-ferromagnetic point contacts by andreev reflections.' Appl. Phys. Lett., 487 (2000).

[103] M. S. Kalenkov and A. D. Zaikin. 'Crossed andreev reflection at spin-active interfaces.' Phys. Rev. B, 76 (22):224506 (2007).

[104] D. Beckmann, H. B. Weber and H. v. Löhneysen. 'Evidence for crossed andreev reflection in superconductor-ferromagnet hybrid structures.' Phys. Rev. Lett., 93 (19):197003 (2004).

[105] A. Levy Yeyati, F. Bergeret, A. Martin-Rodero and T. Klapwijk. 'Entangled andreev pairs and collective excitations in nanoscale superconductors.' Nature Physics, 3:455 (2007).

[106] W. D. Oliver, F. Yamaguchi and Y. Yamamoto. 'Electron entanglement via a quantum dot.' Phys. Rev. Lett., 88 (3):037901 (2002).

[107] C. Bena, S. Vishveshwara, L. Balents and M. P. A. Fisher. 'Quantum entanglement in carbon nanotubes.' Phys. Rev. Lett., 89 (3):037901 (2002).

[108] P. Recher, E. V. Sukhorukov and D. Loss. 'Andreev tunneling, coulomb blockade, and resonant transport of nonlocal spin-entangled electrons.' Phys. Rev. B, 63 (16):165314 (2001).

[109] L. G. Herrmann, F. Portier, P. Roche, A. L. Yeyati, T. Kontos and C. Strunk. 'Carbon nanotubes as cooper-pair beam splitters.' Phys. Rev. Lett., 104 (2):026801 (2010).

[110] J. C. Cuevas, A. Levy Yeyati and A. Martín-Rodero. 'Kondo effect in normal-superconductor quantum dots.' Phys. Rev. B, 63 (9):094515 (2001).

[111] F. Schwabl. *Quantenmechanik* (Springer, 2007), 7th edn.

[112] J. Kong, H. Soh, A. Cassell, C. Quate and H. Dai. 'Synthesis of individual singlewalled carbon nanotubes on patterned siliconwafers.' Nature, 878–881 (1998).

[113] T. Kontos, M. Aprili, J. Lesueur, X. Grison and L. Dumoulin. 'Superconducting proximity effect at the paramagnetic-ferromagnetic transition.' Phys. Rev. Lett., 93 (13):137001 (2004).

[114] R. Richardson and E. Smith. *Experimental Techniques in Condensed Matter Physics at low Temperatures* (Westview Press, 1998), 2nd edn.

[115] C. Enns and S. Hunklinger. *Tieftemperaturphysik* (Springer, 2000), 1st edn.

[116] L. Hofstetter, S. Csonka, J. Nygard and C. Schönenberger. 'Cooper pair splitter realized in a two-quantum-dot y-junction.' Nature, 461:960 (2009).

[117] G. Burkard, D. Loss and E. V. Sukhorukov. 'Noise of entangled electrons: Bunching and antibunching.' Phys. Rev. B, 61 (24):R16303 (2000).

[118] T. Delattre. *Fluctuations quantiques de courant dans les nanotubes de carbone* (unpublished, 2009), ph.d. thesis, ens paris edn.

Acknowledgements

All of this would never have been accomplished without the help of many people. In particular, I would like to thank

- My advisors, Takis Kontos and Christoph Strunk
- Milena Grifoni, Elke Scheer, Bernard Plaçais, Vincent Bouchiat and Jascha Repp, who agreed to act as referees for my thesis
- Fabien Portier and Patrice Roche, who helped me with the measurements at CEA Saclay
- Alfredo Levy-Yeyati, who developed the theory corresponding to our experiments
- The engineers and technicians Thomas Haller, Martin Furthmeier, Klaus Lachner, Cornelia Deinhardt, Uli Gürster, Patrice Jacques, Michael Rosticher and Pascal Morfin
- The workshops at ENS Paris, CEA Saclay and the University of Regensburg
- The chair directors at Regensburg and Paris, Dieter Weiss and Christian Glattli
- The permanent staff members at Laboratoire Pierre Aigrain Gwendal Fève, Audrey Cottet, Claude Delalande and Jean-Marc Berroir
- Our secretaries Claudia Rahm, Elke Haushalter and Anne Matignon
- Dr. Andreas Hüttel for various explanations
- All of the Ph.d. colleagues and post-doctoral researchers at our groups at ENS Paris, CEA Saclay and the University of Regensburg